Georg Arnold, BSc

Quasi-1D Nano-Resonators for Ultra-Sensitive Gas Sensing Applications

MASTER THESIS

For obtaining the academic degree
Diplom-Ingenieur

Master Program of
Technical Physics

Graz University of Technology

Supervisor:

Ao. Univ.-Prof. Dipl.-Ing. Dr.techn. Werner Grogger

Institute for Electron Microscopy and Nanoanalysis

Co-Supervisor:

Dipl.-Ing. Dr.techn. Harald Plank

Graz, May 2015

Abstract

During the last decades cantilever based sensing systems have become the focus of innovative studies and approaches and has attracted enormous attention due to their high sensitivities on selective analyses in gaseous and liquid environments. A key element for fast and sensitive detection is the application of high aspect ratio geometries. However, the fabrication of such architectures is often complicated and mostly restricted to surfaces where classical resist-based lithography can be employed. Focused electron beam deposition (FEBID) is a perfectly eligible approach to meet this barrier. This fabrication technique is a powerful additive, mask-less, direct-write method and allows an incredible variety of 3-dimensional geometries. Furthermore, the fabrication can be finished within a second-to-minute time scale even on non-flat surfaces of practically each material suitable for scanning electron microscopy (SEM) conditions. Therefore, the sensing systems developed in this thesis are not limited to cantilever geometries and therefore open new application environments.

The basic architectures for gas sensing applications are free-standing, quasi-1D nano-pillars with thicknesses in the sub-100 nm regime. Adjacent electrodes are used to exert electric AC fields on these nano-pillars which put them into oscillation according to its mechanical resonance frequency. In order to address reproducibility issues the thesis starts with in-depth investigations of the consequences of preparation parameters concerning geometrical, chemical and mechanical properties and thereby the resonating behavior. Next, the tunability of nano-mechanical properties is studied in detail via post-growth e-beam treatments which allows specific adaption of Young’s moduli by almost one order of magnitude. These findings are correlated with theory leading to an adapted mathematical model in good agreement with all experimental findings. These nano-resonators are subjected to extensive gas-exposure experiments leading to the identification of adsorption and diffusion influences as essential outcome of this thesis. Finally, the sensor concept had been tested with different 3D architectures and allowed a first proof-of-concept for the application of quasi-1D nano-pillars in the highly sensitive gas-sensing concept. By that, this thesis does not only provide the foundation for further developments but also gives a fundamental insight into the mechanics of nano-granular composite materials fabricated via FEBID in a fast and direct manner.

Kurzfassung

Cantilever-Sensoren haben in letzter Zeit in der Wissenschaft vermehrte Aufmerksamkeit erhalten, da durch sie die selektive Umgebungsanalyse sowohl in gasförmigem als auch flüssigem Zustand höchst sensitiv durchgeführt werden kann. Der Schlüssel für diese hohe Sensitivität und eine schnelle Detektion liegt in ihren extremen Seitenverhältnisse. Allerdings konnte die Herstellung solcher Sensoren häufig mit bedeutenden Hindernissen verbunden und vielfach nur in solchen Fällen möglich, wo klassische Lithographie-Verfahren basierend auf empfindlichen Lacken (Resists) angewendet werden konnten. Der Abscheidung durch fokussierte Elektronenstrahlen (FEBID) sind jedoch als maskenfreier, direct-write Synthese von funktionellen Nanostrukturen hinsichtlich Form und Gestalt praktisch keine Grenzen gesetzt und das innerhalb eines mehr als akzeptablen zeitlichen Rahmens. Zudem ist die Abscheidung auch auf strukturierten Oberflächen und allen Materialien möglich, die sich für die Betrachtung mittels Rasterelektronenmikroskop (REM) eignen. Die in dieser Arbeit entwickelten Sensorsysteme sind daher in ihrer Geometrie bei weitem nicht nur auf Cantilever-Plattformen beschränkt und eröffnen neue Anwendungsmöglichkeiten.

Als Basisstruktur wurden quasi 1-dimensionale Nanostäbchen verwendet mit Durchmessern unter 100 Nanometer (nm), die über benachbarte Elektroden durch elektromagnetische Kräfte, in Eigenschwingung versetzt wurden. Um ein tiefgreifendes Verständnis der Resonatorstrukturen zu entwickeln und die Reproduzierbarkeit der Versuche zu garantieren, mussten zuerst die durch die geometrischen, chemischen und mechanischen Eigenschaften bestimmten Schwingungseigenschaften untersucht und darauf einflussnehmende Herstellungsparameter ermittelt werden. Im nachfolgenden Schritt wurde die Veränderung der nanomechanischen Eigenschaften in Form des Elastizitätsmoduls (bis zu einer Größenordnung!) durch eine Nachbehandlung der Nanoresonatoren mit dem Elektronenstrahl und damit die Durchstimmbarkeit der Resonanzfrequenz eingehend beleuchtet. Die Ergebnisse zeigten eine gute Übereinstimmung mit einem entsprechend adaptierten mathematischen Modell aus der Schwingungsmechanik. Auf Grundlage dieses Wissens wurden diese Nanoresonatoren in umfassenden Experimenten verschiedenen gasförmigen Umgebungen ausgesetzt, wodurch Einflüsse von Adsorption und Diffusion auf das Schwingungsverhalten ermittelt werden konnten. Dies stellt zugleich ein weiteres wesentliches Ergebnis dieser Arbeit dar und bestätigt die Anwendbarkeit von quasi 1-dimensionalen Nanostäbchen als hochsensitive Gassensoren. Abschließend wurde das verwendete Sensorkonzept auch an dreidimensionale Nanoresonatoren getestet. Damit liefert diese Arbeit nicht nur die Grundlage für weitere Forschungen sondern gibt auch einen tiefgreifenden Einblick in die Eigenschaften nanogranulare Materialien hergestellt durch FEBID.

Acknowledgements

I would like to express my deep gratitude to all persons, which provide support and advices during my work. First of all I would like to thank Professor Ferdinand Hofer, head of our institute, for offering the possibility to write this thesis.

I would also like to thank Professor Werner Grogger for being my supervisor and for his cooperation.
My deepest appreciation goes to my co-supervisor Harald Plank for his imperturbable trust and belief in this project, his invaluable inspiration and our partly persistent but always fruitful and fulfilling discussions.
This thesis would not have been possible without my colleagues at the FELMI-ZFE, who always provided guidance, support or encouragement. In particular my sincere thank goes to Roland providing guidance in and outside of work; to Robert with his unshakeable patience and serenity; and to Thomas for sharing his knowledge with me and advising an electro-technical scrub.
Special thanks and appreciation goes to Martin for his outstanding work, which offers me the possibility to build on his excellent concept.
I also would like to express my sincere thanks to my friends for providing both, amusing distraction from and useful input for my work.

Mein größter Dank aber geht an meine Eltern und Großeltern, für ihre Unterstützung und ihr Vertrauen, ihre Erziehung und Anleitung, ihre lebensbejahende Einstellung und Naturverbundenheit, ihre Liebe. Ihr habt mich zu dem gemacht, der ich bin!

Motivation

The detection of ambient parameters has become a central part of modern technology, e.g. the presence of harmful gases in the surrounding air. What is more, the ongoing miniaturization of technical devices is pursued by the desire for enhanced mobility in normal life. The aim of this thesis meets both trends.

On the one hand, focused electron beam induced deposition (***FEBID***) is a direct write technique of increasing importance and allows the fabrication of 3-dimensional structures in the sub-10nm scale. This allows wide range control of mechanical properties.

On the other hand, it is naturally of wide-spread interest to detect even smallest traces of undesired components. In addition, the development of a gas-sensing system with extreme sensitivity is a highly challenging task which demands comprehensive knowledge about the particular components of the gas sensing system.

A wide variety of FEBID fabricated sensors has already been developed. Some of them were developed at the Institute for Electron Microscopy and Nanoanalysis (Graz University of Technology) taking advantage of the nano-granular metal-matrix structure conditioned by the use of $\mathrm{MeCpPt^{IV}Me_3}$ as gaseous precursor. This work is intended to follow up previous paths and develop a gas sensing system based on the knowledge of previous works.

Table of contents

List of Abbreviations

aC	…	*amorphous carbon*
BSE	…	*back scattered electrons*
ELR	…	*Electron limited regime*
FWHM	…	*full width at half maximum*
FEBID	…	*focused electron beam induced deposition*
DBM	…	*dual beam microscope*
DE	…	*diffusion enhanced*
DT	…	*dwell time*
FIB	…	*focused ion beam*
ETD	…	*Everhardt Thornley detector*
FEG	…	*field emission gun*
FSE	…	*forward scattered electrons*
gC	…	*glassy carbon*
GFR	…	*gas flux replenishment*
GIS	…	*gas injection system*
keV	…	*kilo electron volts*
kHz	…	*kilohertz*
MLR	…	*molecule limited regime*
nm	…	*nanometer*
pA	…	*picoampere*
PE	…	*primary electrons*
PGT	…	*Post-growth treatment*
POP	…	*Point pitch*
PSD	…	*position sensitive detector*
RRL	…	*reaction rate limited*
RT	…	*refresh time*
SDR-D	…	*Deposit related surface diffusion replenishment*
SDR-S	…	*Substrate related surface diffusion replenishment*
SE	…	*secondary electrons*
SEM	…	*scanning electron microscopy*
TEM	…	*transmission electron microscopy*
TET	…	*total exposure time*
TLD	…	*through the lens detector*
VGR	…	*Volume growth rate*
zGR	…	*Vertical growth rate*

Motivation

The detection of ambient parameters has become a central part of modern technology, e.g. the presence of harmful gases in the surrounding air. What is more, the ongoing miniaturization of technical devices is pursued by the desire for enhanced mobility in normal life. The aim of this thesis meets both trends.

On the one hand, focused electron beam induced deposition (***FEBID***) is a direct write technique of increasing importance and allows the fabrication of 3-dimensional structures in the sub-10nm scale. This allows wide range control of mechanical properties.

On the other hand, it is naturally of wide-spread interest to detect even smallest traces of undesired components. In addition, the development of a gas-sensing system with extreme sensitivity is a highly challenging task which demands comprehensive knowledge about the particular components of the gas sensing system.

A wide variety of FEBID fabricated sensors has already been developed. Some of them were developed at the Institute for Electron Microscopy and Nanoanalysis (Graz University of Technology) taking advantage of the nano-granular metal-matrix structure conditioned by the use of $MeCpPt^{IV}Me_3$ as gaseous precursor. This work is intended to follow up previous paths and develop a gas sensing system based on the knowledge of previous works.

1 Focused Electron Beam Induced Deposition (FEBID)

The direct write technique focused electron beam induced deposition (**FEBID)** allows additive 3-dimensional nano-fabrication[1–3], typically performed in a scanning electron microscope (**SEM**) or in dual beam microscopes (BDM) with additional focused ion beam (**FIB**) capabilities. The functional properties of final deposits depend on the used precursor gas and spans from insulating, over semi-conducing to conductive or magnetic[3–5].

1.1 Basic Requirements

The deposition of materials requires two essential components: a gaseous precursor provided by a gas injection system (**GIS**) as basic material of the deposits and a focused electron beam which initiates the deposition process.

Electron beam

The electron column of a typical SEM consists of an electron point source (e.g. a Schottky emitter) and a system of electron lenses which are responsible for the demagnification of the electron beam and focusing onto the specimen of interest. The resulting beam exhibits a Gaussian lateral distribution and diameters down to about 1 nm. Two pairs of scanning coils deflect the electron beam and enable the highly accurate positioning on the sample.

Precursor gas

The second main component which is inevitable for performing FEBID is the precursor gas. There exists a variety of precursor materials[4]. The precursor of choice depends on the intended functionality of the deposited structure. However, all gaseous precursors have in common that they comprise a central atom or ion and several ligands. This complex has to meet one particular exigency: a volatile character in vacuum conditions at reasonable temperatures to prevent temperature related degradation of the sample surfaces (typically below 80 °C). In order to satisfy this essential demand, it is indispensable that the total charge of the overall complex disappears[1,6]. In addition, the charge of single components must also not exceed moderate values to avoid facile polarization.

The precursor gas is typically stored in a heated reservoir in order to guarantee a stable gaseous phase. A thin needle (Ø < 500 µm) injects the gaseous precursor in close proximity onto the specimen surface (< 100 µm) and leads to a directional gas flux towards the site of deposition providing a high density of precursor molecules around the electron beam.

1.2 Concept

High vacuum conditions are inevitable for FEBID because chemisorbed gas species would degrade the pureness of the deposits. What is more, the spatial resolution of the deposition process would be deteriorated as well as the efficiency.

Figure 1-1 reveals the basic concept of FEBID. Precursor molecules are inflated via the GIS and absorb onto the specimen surface, followed by random diffusion and final desorption with typical diffusion lengths and residence times[7]. Then impinging electrons including their secondary processes (cf. chapter 1.3) cause dissociation of the precursor complex into volatile and non-volatile fragments. The latter remain on the exposed spot and form the deposit. Volatile parts are pumped out.

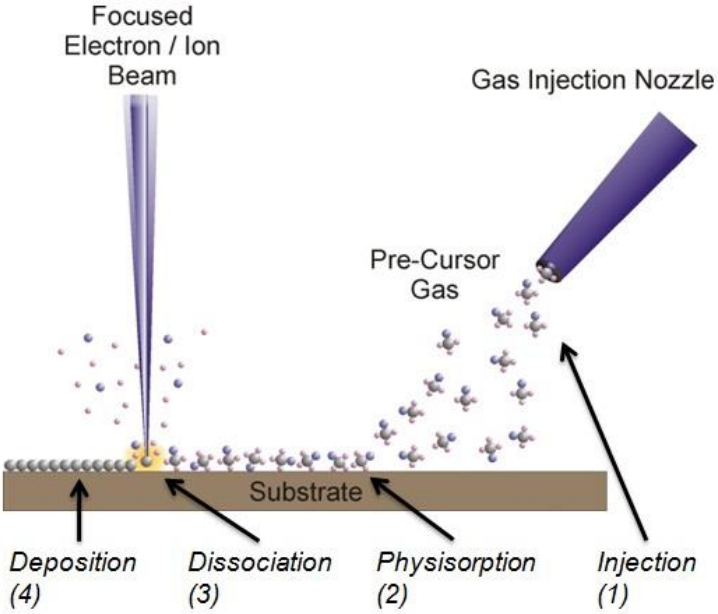

Figure 1-1: Simplifying working scheme of FEBID: Precursor molecules are injected via a gas injection system (1) and absorb on the sample surface (2). The beam particles lead to a dissociation of the precursor (3) and non-volatile particles build the deposit (4).[8]

1.3 Electron Induced Processes

The scheme in Figure 1-1 may give the impression that only primary electrons (**PE**) of the electron beam cause the dissociation of precursor molecules. In fact, primary electrons impinge the substrate and lead to a multitude of processes and side effects within the specimen. It is common to distinguish between processes in which the energy of the electron is conserved (elastic scattering) and those which lead to a transfer of energy (inelastic scattering). However, all scattering processes change the original path of the primary electrons.

Elastic scattered electrons

The path of electrons may be altered by an interaction with the coulomb field of an atom's nucleus. As a result, this process is influenced by the atomic number Z of the atom which leads to the scattering process[9].

Back-scattered electrons (BSE): These electrons escape from the substrate on trajectories which differ more than 90° from the original path of PE. These trajectories may extend several µm into the substrate before BSE eventually leave the specimen.

Forward-scattered electrons (FSE): This term includes all electrons eluding from the deposit on paths whose deviation from the original trajectory is < 90°. Hence, FSE cannot be generated on flat substrates but are highly relevant for higher side walls or free-standing 3D nano-scale architectures.

Inelastic scattered electrons

The kinetic energy of electrons can also be transferred via a collision with bound electrons. This may initiate several follow-up processes:

Secondary electrons (SE): Electrons with kinetic energies exceeding the ionization potential may also interact with electrons of outer shells and generate free electrons of low kinetic energy (secondary electrons). The upper limit of SE energy is conventionally defined at 50 eV. SEs are not exclusively generated by PE but also via BSE which led to the notation as SE-type I (SE_I) and SE-type II (SE_{II}) electrons, respectively. For an easier differentiation – although slightly again the classical notation – we further denote FSE related SEs as type III and by that as SE_{III} throughout this thesis.

Ionization of inner atomic shells: When an electron of an inner shell is ejected another electron of higher shells fills up the vacancy and a characteristic X-ray photon is emitted. A concurrent process that may take place after ionization of an inner shell is the emission of an Auger electron, where the energy released by the de-excitation is transferred to another atomic electron.

Excitation of molecules: The largest fraction of energy lost by inelastic scattering processes is converted into heat via creation of phonons.

These processes lead together to an energy spectrum of electrons leaving the specimen ranging from the initial energy of the PE to almost 0 eV. What is more, all electrons may cause dissociation of precursor molecules, although the probability depends on the electron energy, which makes the deposition process even more sophisticated (see chapter 1.3).

Figure 1-2 reveals the energy spectrum of electrons emerging from impinging PE (left). The largest amount is accounted for SE (< 50 eV). Due to their low energy SEs can only escape from a very thin layer near the surface in the range of a few nanometer. The penetration depth of BSE is considerably higher (Figure 1-2, right). These energy dependent trajectories of electrons define the ***interaction volume*** which depends on both, primary electron energy and chemical composition of the penetrated volume.

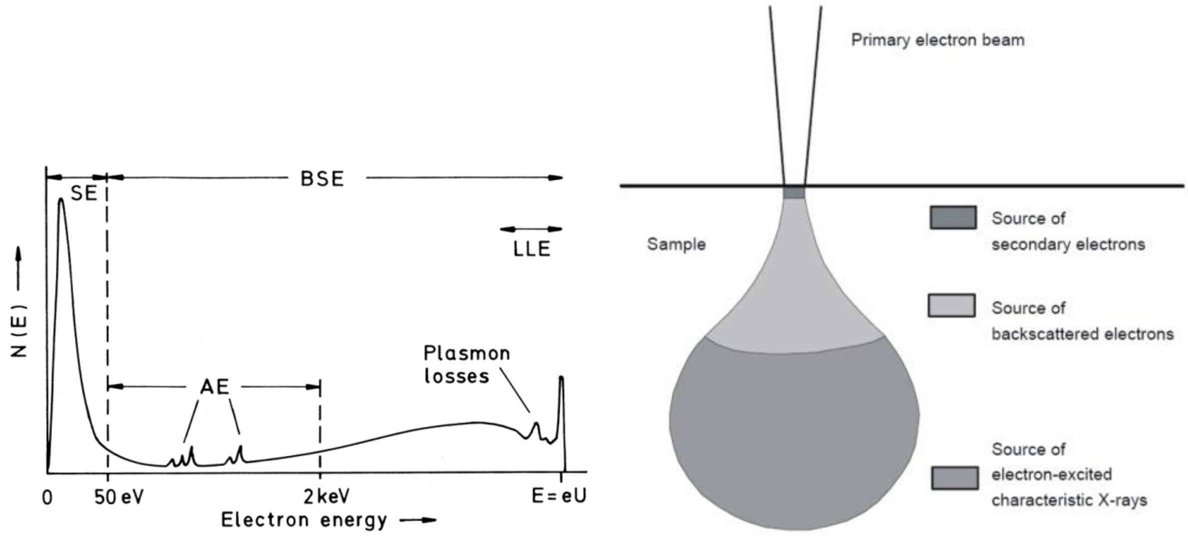

Figure 1-2: left: relative energy distribution of reemitted surface electrons. Right: schematic interaction volume inside the specimen together with individual assignment for different electron species.[10,8]

1.4 Dissociation Process

First of all, electrons naturally have to be able to reach the sample's surface to fulfill the spatial requirement for a dissociation of precursor molecules adsorbed on the surface. These electrons shall be collectively denoted as *surface electrons*. Initially, PE electrons impinge the sample and therefore cross the surface and are one kind of electrons which could interact with precursor molecules. PE may be scattered inside the growing deposit (FSE) or inside the substrate under high angles so that they can leave the specimen (BSE), as described above in section 1.3. In both cases, these electrons (FSE and BSE) may encounter precursor molecules. What is more, all electrons mentioned above can generate low energy SE on the specimen surface. Whether a precursor molecule gets dissociated by an electron or not depends on the dissociation cross section.[11] Practically speaking, this cross section describes the dissociation probability for a given electron energy. Dissociation of precursor molecules is mainly caused by electrons with energies of a few eV and therefore SE (***dissociative electron attachment***). The dissociation mechanism for electrons with energies in the range of the ionization energy is called **dissociative ionization** but this process is less likely due to the large amount of SE around 3 eV (Figure 1-2).[9] Electrons with high energies like PE rarely cause dissociation of precursor complexes.[1,3] However, a precursor molecule has to undergo tens of dissociation processes for complete dissociation of the precursor's central atom and surrounding ligands. As a result, the ratio of precursor molecules adsorbed on the sample surface and potentially dissociating electrons is decisive factor for FEBID which will be discussed in the following.

1.5 Adsorption Rate Model

The initial density of precursor molecules on the sample surface depends on the rate of adsorption. According to the adsorption rate model, four different processes contribute to a changing number of precursor molecules on the surface $\frac{\partial n}{\partial t}$ and hence the precursor coverage on the sample[12,13]:

$$\frac{\partial n}{\partial t} = \underbrace{sJ\left(1 - \frac{n}{n_0}\right)}_{1} + \underbrace{D\left(\frac{\partial^2 n}{\partial r^2} + \frac{1}{r}\frac{\partial n}{\partial r}\right)}_{2} - \underbrace{\frac{n}{\tau}}_{3} - \underbrace{\sigma f n}_{4} \qquad \text{1-1}$$

Each term describes one of the contributing processes

1) ***Gas adsorption***
2) ***Diffusion***
3) ***Desorption***
4) ***Decomposition***

The gas adsorption depends on the sticking probability *s*, the gas flux *J* and the instantaneous coverage n/n_0, where n_0 is the number of molecules in a complete monolayer. In the regions exposed to the beam occurs depletion of precursor molecules[1,14]. The resulting gradient of concentration leads to diffusion of molecules from other areas. *D* is the diffusion coefficient and the term inside the brackets describes the concentration gradient. The residence time τ (third term) determines the spontaneous thermal desorption and the fourth process is related to the decomposition of precursor molecules by the electron beam with the electron impact dissociation net cross section $\sigma(E)f$ and the Gaussian beam distribution f. $\sigma(E)$ and $f(r,E)$ also affect the laterally resolved, vertical rate of deposition $R(r)$[15]:

$$R(r) = Vn(r)\int_0^{E_0} \sigma(E)f(r,E)dE \qquad \text{1-2}$$

V is the Volume of the decomposed molecule and *n(r)* the number of adsorbed molecules per surface unit. Assuming rotational symmetry *r* is the distance to the center of the electron beam.

As can be seen the situation is highly complex. Even more critical, it changes over time and the current deposition situation.

1.6 Beam Parameter

The complementary part to precursor molecules at FEBID is given by dissociating electrons. The electron density and electron energy spectrum can be controlled by beam diameters. At first, the **acceleration voltage** determines the primary electron energy and therefore the number of generated SE and the area they may originate from. The **beam current** pretends the time between two incident electrons and influences the order of local precursor molecule depletion in the impacted area. As discussed in section 1.3, the primary energy changes the expansion of the interaction volume. Figure 1-3 demonstrates the influence of the electron energy on the spatial distribution by an in-scale-comparison. On the left, Monte Carlo simulations are shown for electrons with high energies of 30 keV in a silicon (Si) substrate, performed via CASINO® 2.4.2[16–18]. The right plot reveals the results for equal electron settings but changed the acceleration voltage. The electron energy was decreased from 30 keV to 5 keV. Taking the use of an equal number of electrons into account, two effects become obvious: ***1)*** the lateral densities of BSE (red trajectories) and by that SE_{II} are much higher for lower energies; and ***2)*** the smaller vertical penetration leads to a higher number SE_{I} on the surface. The virtually same effect is occurring for different materials: lighter chemistry leads to larger interaction volumes and vice versa. The latter has a strong effect when heavy element deposits (e.g. Pt) are fabricated on low weight substrates such as Si. Then the density of surface electrons is dynamically changing until the deposit's growth process has progressed sufficiently so that the entire interaction volume is captured within the deposit. These dynamics further complicate the deposition process[7].

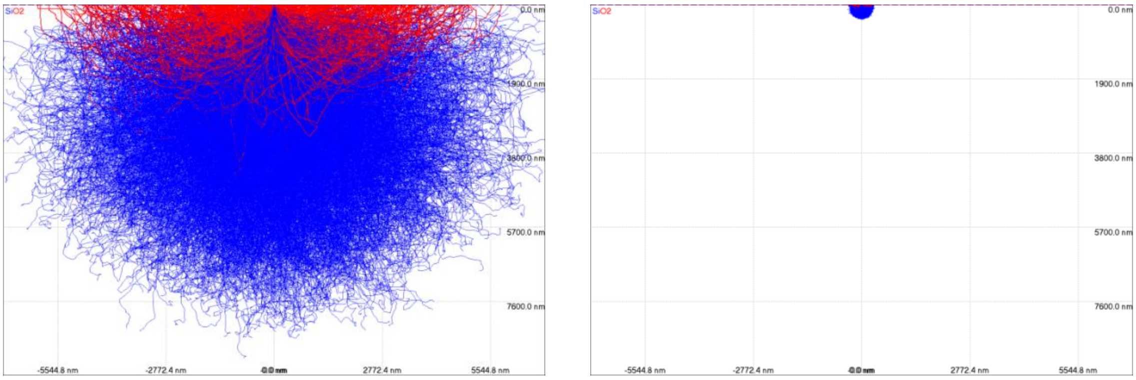

Figure 1-3: Direct comparison of the interaction volume for electrons in Si with primary energies of 30 keV (left) and 5 keV (right) by Casino® Monte Carlo simulations. Red indicates the trajectories of BSEs, which generates SEII on the surface. The considerably smaller interaction volume explains the higher electron density around the electron beam on the surface at acceleration voltages of 5 keV.

1.7 Working Regime

As described in 1.4, the dissociation process and therefore many deposit characteristics, e.g. the chemical composition[1,14] , functionality[19] or growth rates[14], are determined by the ratio between available precursor molecules and potentially dissociating electrons[1,14,20,21]. Two extreme conditions can occur:

1) The depletion of precursor molecules can be compensated and sufficient precursor molecules cover the surface around the electron beam. As a result, the rate of deposition is determined by the presence of dissociating electrons. This working regime is referred to electron limited regime (***ELR***).
2) In molecule limited regime (***MLR***), the rate of deposition is not limited by electrons but the presence of precursor molecules and their replenishment.

Assuming the surface emission of electrons to be constant in first approximation for given primary energies / beam currents, the local number of precursor molecules depends on the so called replenishment mechanism which “reloads” local areas. This mainly consists of two components:

i) *Directly from the precursor gas flux → gas flux replenishment (**GFR**)*
ii) *By diffusion from surrounding areas → surface diffusion replenishment (**SDR**)*

While the former is constant over time, the latter gets more complicated for a growing deposit. In more detail, the SDR component splits into two components: ***1)*** SDR from surrounding substrate (**SDR-S**); and ***2)*** SDR from the deposit itself (**SDR-D**) once the deposit is high enough that precursor molecules desorb before they can diffuse from the substrate to topmost areas. Considering quasi-1D nano-pillars, the basic geometry in this thesis, we are faced with enormous aspect ratios. Hence, SDR-D components quickly dominate the replenishment mechanism since it becomes very complicated for substrate related molecules (SDR-S) to diffuse along the narrow pathway towards the top of the growing nano-pillar. As a result, for higher pillars almost all precursor molecules originate from adsorption from the gas flux which replenish the new growth area directly (GFR) but also in their vicinity leading to weaker SDR-D components. With this framework of a widely constant replenishment rate for high pillars (typically above 2 µm as shown by Plank et al.[14]) it is possible to discuss the influence of the beam current: the more electrons are present the higher is the growth rate due to an enhanced dissociation rate. However, this has strong implications on the chemistry: for a very low number of electrons the local dissociation is incomplete leading to the incorporation of unwanted precursor fragments. On the other hand, a high number of electrons lead to high degrees of dissociation and to an excess of electrons. These surplus electrons, in turn, start to polymerize precursor fragments which fact increases again the carbon content in the FEBID deposit. This describes a classical transition from electron limited towards molecule limited regimes denoted as ELR and MLR, respectively (cf. section 3.1.4).

1.8 Summary

FEBID bases on two main components: Precursor molecules and dissociating electrons. The precursor molecules can originate from either the gas flux of the GIS system (***GFR***) or diffusion from surrounding areas (***SDR***). The latter naturally decreases for growing deposits. Whereas the influencing parameters of adsorption and replenishment of precursor molecules for a given precursor and substrate are fixed by adsorption rate, morphology, gas flux etc., the electron density and their energy can be simply accessed via microscope's beam parameters, e.g. acceleration voltage and beam current. Hence, varying these electron beam parameters can alter the ratio between precursor molecules and electrons in the deposition area and therefore the working regime with implications to the chemistry and its final functionalities.

The concept described in the previous sections consistently explains an increasing volume growth rate (**VGR**) for lower primary energies: ***1)*** the dissociation probability is higher for lower primary energies according to the dissociation cross-sections; and ***2)*** the smaller interaction volume results in a higher electron emission of all electron species per area. Both factors together simply increase the VGR of growing deposits for decreasing electron energies. However, the more important consequence is the chemistry and the structure as discussed later in chapter 6.

2 Related Previous Work

Although there exists a wide variety of methods which allows the determination of mechanical quantities (e.g. stiffness, strength, elasticity), these properties are rarely investigated for FEBID nano-deposits which is mostly related to the very small dimensions.

2.1 Mechanically Induced Bending and Vibration Experiments by Ivo Utke

Ivo Utke et al.[22] explored mechanical properties of quasi 1D pillars fabricated by FEBID using a Copper based precursor, to be specific $Cu(C_5HF_6O_2)_2$. Stiffness and Young's modulus of these pillars were derived from bending experiments using a SiO_2 cantilever with well-known mechanical characteristics. By moving the cantilever against the pillar using a high accuracy piezo stage, bending of both components occurred. Deflection measurements allowed calculating appearing forces and the force constant of the deposited pillar according to Hooke's law, as the force constant of the cantilever was known. In addition, Young's modulus ***E*** could be derived from

$$E = \frac{64}{3\pi}\frac{l^3}{w^4}\frac{F}{d_{max}} \tag{2.1}$$

with length ***l***, diameter ***w***, the applied force ***F***, and the maximum deflection $\boldsymbol{d_{max}}$ of the cylindrical deposit.

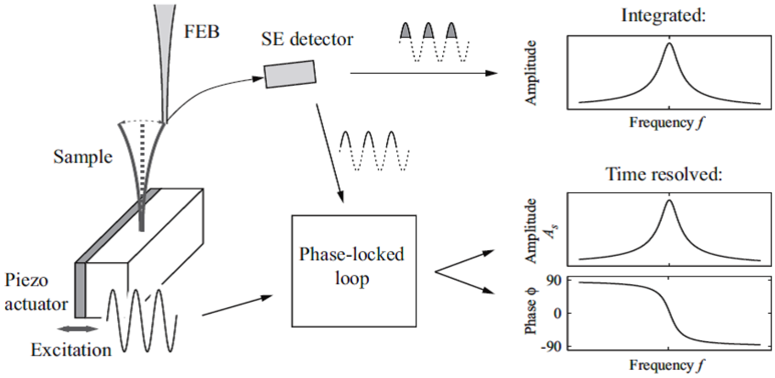

Figure 2-1: Schematic experimental setup of vibration experiments performed by Utke et al. [23].

In order to receive the deposits' densities vibrational tests were performed as there is a particular relation between the resonance frequency and a structure's density and Young's modulus respectively (cf. equation (2.1)). The mechanical excitement of the pillar was carried out by a piezo driven actuator and the deposit's response at the intrinsic resonance frequency was detected via SEM. A lock-in amplifier separated the superposing signal of the substrates piezo driven movement and the pillar's oscillation. The deposition took place at electron beam energies of 5 keV and 20 keV. Unfortunately, the corresponding currents are not known. Some important results are given in Table 2-1 for comparison to the results in this thesis. As one can see, the average density is rather low and therefore similar to that of carbon. 20 keV deposits exhibit both a higher density and an increased Young's modulus compared to those deposited with 5 keV electrons.

Table 2-1: Mechanical properties for $Cu(C_5HF_6O_2)_2$ pillars determined by Ivo Utke et-al.

	5 keV	**20 keV**
Young's modulus	(17 ± 6) GPa	(25 ± 8) GPa
Average density	(2.2 ± 0.2) g/cm^3	(2.8 ± 0.2) g/cm^3
Matrix density	(1.2 ± 0.3) g/cm^3	(2.2 ± 0.5) g/cm^3

2.2 Electrically Induced Deflection and Resonance Experiments by Martin Stermitz

Martin Stermitz and Harald Plank developed an approach different to the mechanical excitation of Utke by using electromagnetic fields.[22] In addition, deflection experiments could be carried out with the same experimental setup except applying a DC voltage instead of an AC field.

The idea behind this strategy was the electric force ***F*** acting between electrodes of a plate capacitor (capacity ***C***, plate area ***A***, distance ***d***, voltage ***U***) in vacuum:

$$F = \frac{1}{2}\frac{CU^2}{d} = \frac{1}{2}\varepsilon_0 A \left(\frac{U}{d}\right)^2 \tag{2.2}$$

Structures deposited with an appropriate precursor exhibit a certain electrical conductivity, even if it uses to be very low. Hence, these structures could serve as an electrode and application of a voltage between the deposit and a nearby counter electrode would lead to a force between them. A constant voltage induces an electrostatic force, which causes bending of the deposit if the geometry is suitable, e.g. a pillar with rather small diameter resulting in low stiffness. Naturally, the amount of deflection is proportional to the force, i.e. the applied voltage.

Calculating the force between deposit and counter electrode is a highly sophisticated procedure as the force causes bending which, in turn, varies the force. Hence, this is a dynamic system. Stermitz coped with this task via simulation program COMSOL® and developed a procedure that calculated Young's modulus.

Applying an AC field with the appropriate frequency, i.e. the intrinsic resonance frequency of the deposit, leads to oscillation of the deposited structure. This can easily be detected via SEM. The results of these two experiments, namely electrostatic and electrodynamic investigations, can be combined by equation (5.16) to gain the density, which will be explained in detail in sections 5 and 6.

What is more, post-growth treatment enabled the tunability of the resonance frequency. TEM and EDX investigations revealed that outer dimensions and the chemical composition remained rather constant while changes in the internal structure led to a strong increase of resonance frequency and Young’s modulus depending on the exposure time of the electron beam.[22]

Hence, the method developed by Stermitz offers advantages, especially the less extensive experimental setup, with the single drawback that the investigated deposits need to be conductive. Those achievements form the main basis for the electric resonating concept in this thesis.

2.3 Gas Sensing Concept

Building on the resonating approach, the main aim of this thesis was proving a gas sensing concept that works with quasi-1D-resonators. Previous work[22] revealed the possibility of fabricating deposits with extreme aspect ratios. Quasi-1D pillars can exhibit diameters down to 50 nm at lengths exceeding 10 000 nm. Furthermore, pillars deposited with Pt based precursors are conductive and simultaneously highly elastic. Hence, the approach described above (section 2.2) can be applied and such structures can be put on resonance, resulting in a detectable oscillation of the nano-pillar. Due to the huge aspect ratio the oscillating behaviour is highly sensitive to changes of the ambient conditions, e.g. the surrounding pressure or presence of particular gaseous molecules. The initial gas sensing concept bases on this feature, as the adsorption of gaseous molecules changes the geometric dimensions and therefore the resonance frequency. If the exciting frequency is equal to the deposit’s intrinsic resonance frequency of the structure, there will be a visible oscillation under vacuum conditions. Increasing the pressure leads to the presence and adsorption of appropriate gaseous molecules. This changes the resonance frequency of the structure. As a result, the frequency of the exciting force does not match the resonance frequency of the resonator and the oscillation diminishes or even vanishes (Figure 2-2).

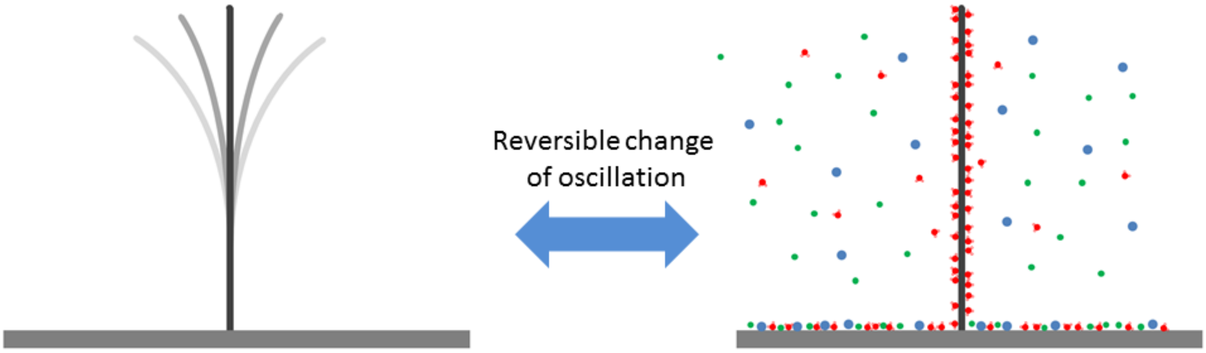

Figure 2-2: Scheme of the working principle of quasi-1D nano-pillars as gas sensing application.

The magnitude of change depends on the number of adsorbed molecules. The resonance frequency of the pillar is determined, inter alia, by the geometric dimensions of the cylindrical pillar with diameter ***d*** and height ***h***, which will be described in more detail in section 5.3:

$$f_{res} \sim \frac{d}{h^2} \tag{2.3}$$

Neglecting in a first approximation the diffusion of gas molecules inside the structure and changes of the structure and its density, one can state, that the shift of resonance frequency at adsorption is caused by a change of the geometric dimensions. An increase in height reduces the resonance frequency, a larger diameter increase it. Assuming similar aspect ratios to those described above, it is obvious, that an increase in the (sub-)nm range affects the diameter (e.g. 50-70 nm) comparatively more than the height (5000-10000 nm). Figure 2-3 illustrates this fact. It reveals the resonance frequency shift of a pillar (height: 6000 nm, diameter: 70 nm) for an increase by adsorption up to 3 nm in height and diameter respectively. The frequency of pillars with an assumed height variation of 3 nm (adsorption monolayer) is rather constant at specific diameters (lines parallel to axis “height”). In contrast, changes in the pillar’s diameter from 70 nm to 73 nm lead to a significant rise in the resonance frequency of about 30 kHz and ought to be detectable by appropriate measuring setup. Hence, there can be expected an overall increase of the resonance frequency at adsorption.

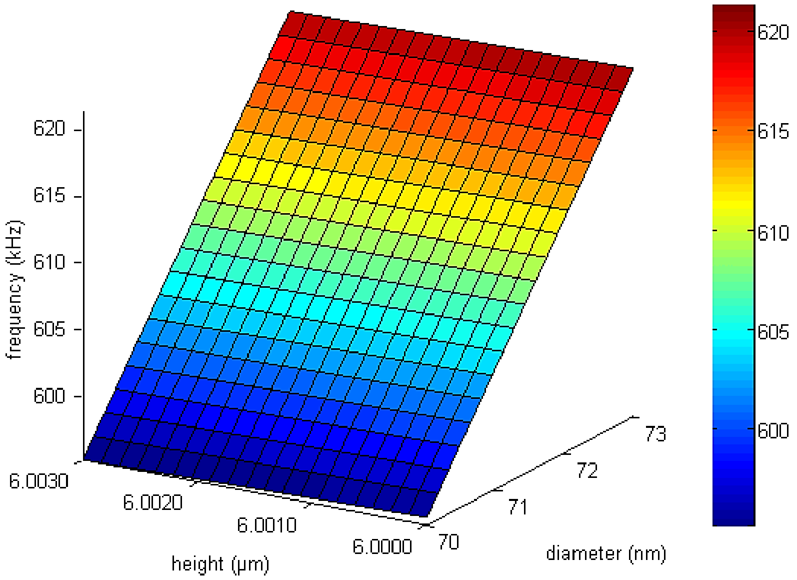

Figure 2-3: Influence on the frequency of a pillar of 6 µm in height and a diameter of 70 nm at changes in diameter and height respectively up to 3 nm.

Please note that this illustration is intended for better understanding and is of qualitative character. Naturally, the considerations above are not only valid for cylindrical geometries. As will be shown during the course of this thesis by an in-depth analyses this initial assumption still holds. However, it is convoluted by diffusion effects which on the one hand complicates the situation but on the other hand opens the door for even more sophisticated sensing concepts.

3 The Microscope Setup

3.1 Dual Beam Microscope - DBM

A combination of an electron microscope (**SEM**) with a focused ion beam (**FIB**) microscope was used for additive and subtractive structuring processes. A heated field emission gun (Schottky emitter) with an electron energy range of 1 keV to 30 keV served as electron source in this FEI Nova 200 Nanolab dual beam microscope (**DBM**). Electron beam currents ranging from 2.5 pA up to 37 000 pA could be used for processing. The lower limit for the beam diameter was specified with 1.2 nm (full width at half maximum - FWHM). The Gallium (**Ga^+**) ions originated from a liquid metal ion source (**LMIS**). The acceleration voltage could be varied from 5 keV to 30 keV and the current range extends from 0.15 pA to 20 000 pA. The FIB was used for sputtering processes, i.e. subtractive nano-structuring. In order to enable additive structuring several GIS systems were installed to provide different gaseous precursor materials with varying properties suitable for the application in question. In this thesis, *custom* and *working GIS*, both containing platinum precursor, were used for FEBID processes. Roughing pumps and a turbo-molecular pump create a high vacuum in the specimen chamber (typically between $2 \cdot 10^{-6}$ mbar and $5 \cdot 10^{-6}$ mbar). The enhanced vacuum in the columns was generated by ion getter pumps and reached down to 10^{-10} mbar.

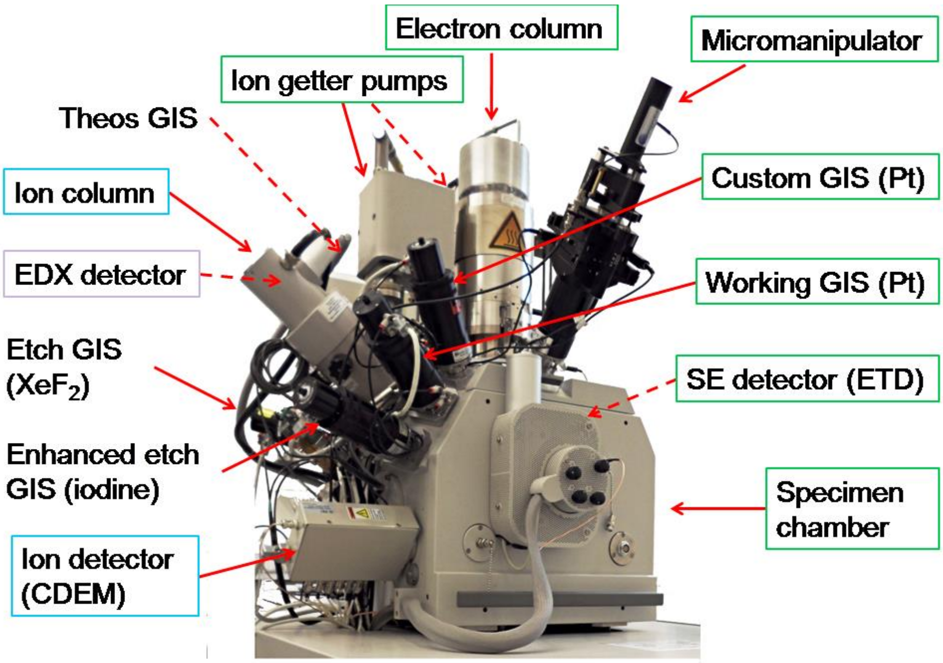

Figure 3-1: Dual beam microscope FIB Nova 200 Nanolab. Green framed components were used for additive structuring i.e. FEBID processes, blue framed for subtractive structuring (sputtering) and constituents used for analytical methods are enhanced by a purple outline. The microscope is additionally equipped with a silicon BSE detector inside the specimen chamber and a through-the-lens detector (TLD) for SE and BSE in the final lens system of the electron column[24 (modified)].

3.1.1 Scanning Electron Microscope – SEM

3.1.1.1 Source

As described above the electron source situated at the top of the electron column was a so called Schottky emitter. This kind of source typically consists of a tungsten tip coated by ZrO_2 which decreases the work function significantly from 4.5 eV to 2.7 eV[25]. Applying an electric field in addition to heating of the tip leads to the emission of electrons. A Wehnelt cylinder holding a negative potential condenses the emitted electrons by repulsive electric forces to a spot which is called gun crossover. An aperture determines the area where electron can pass through and are accelerated to the anode.

3.1.1.2 Lens System

Electromagnetic lenses in combination with apertures further de-magnify the electron beam. Such lenses consist of current carrying copper wires generating an axial magnetic field with rotational symmetry. The entering electrons experience the Lorentz force $\vec{F} = q(\vec{v} \times \vec{B})$. The component of the magnetic field $\overrightarrow{B_{\perp}}$ which is perpendicular to the original, straight-lined electron trajectory $\vec{v}_{\parallel}$ causes a helical path of the electron through the lens. Furthermore, this leads to a rotation of the image. However, this modified spiral trajectory includes components of the velocity $\overrightarrow{v_{\perp}}$ being perpendicular to the initial velocity of propagation. In combination with the magnetic field component $\vec{B}_{\parallel}$ a force towards the central axis is generated which produces the lens effect: electrons will converge at a defined focal point after leaving the lens. The position of this focal point along the main axis can be varied via the strength of the current through the copper windings, i.e. the strength of the magnetic field. The magnetic field is concentrated on small gaps by a surrounding iron shield. The stray field emerging through these gaps leads to a bell shaped distribution of the magnetic field.

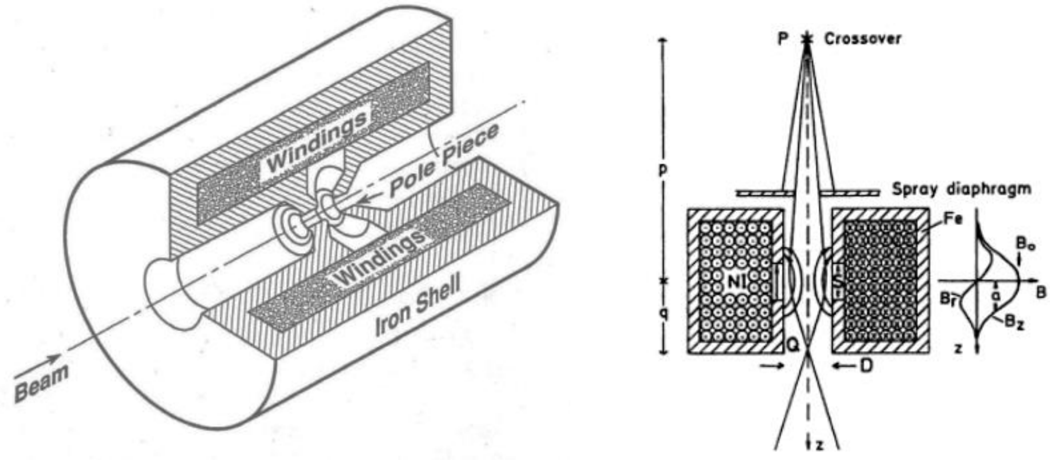

Figure 3-2: Design of an electromagnetic lens (left). A cross section of the lens including the magnetic field inside (right) describes the effects explained in the main text. The gaps in the surrounding iron shields generate a bell shaped magnetic field[9,10].

3.1.1.3 Lens Errors

Four main lens defects limit the achievable minimal beam diameter even after carful on-axis alignment of the electron beam and the use of small apertures:

Spherical aberration: The magnetic field becomes weaker with decreasing distance to the optical axis. Hence, the focal point of electrons far off the axis is closer to the lens exit. Apertures reduce the influence of spherical aberration.

Chromatic aberration: Electron sources exhibit a slight energy spread. The focal length of an electromagnetic lens depends on the velocity of electrons propagating through the lens. Thus, differences in the electron energy lead to a disc of least confusion instead of a single focal spot.

Axial astigmatism: Due to deviations from the optimum distribution caused by charging effects or limitations in production an axial symmetry of the magnetic field is no longer fulfilled. This leads to separated focus points in perpendicular planes and a circle is imaged as an ellipse. This lens defect can be compensated by a magnetic field of four or more poles, and can be manually corrected by adjusting stigmator settings in the “FEI system control” software corresponding to the NOVA 200. As will be described in this thesis, this aberration disserves high attention and careful correction.

Diffraction error: The finite dimensions of apertures cause a Fraunhofer diffraction pattern and an airy disc is formed in the focal plane instead of a well-defined point.

Achievable resolution: Beside the above mentioned effects, the achievable resolution is crucially determined by the interaction volume of the impinging electrons (cf. section 1.6) since the electrons used for imaging in a SEM originate from a large area around the electron beam.

3.1.1.4 Detectors

The signal of choice used for topographic imaging issues is related to SEs and in particular to SE_I as they provide best spatial resolution due to their low energy and, as a result, their diminishing possibility to escape the specimen from regions not deeper than a few nm. The SEM in the NOVA 200 uses Everhart-Thornley detectors (**ETD** in Figure 3-3). The electrons are collected by a positively biased grid (100 V – 200 V) and afterwards accelerated to a scintillator (10 kV) where they produce a large number of electron-hole pairs. These charge carriers recombine and generate light. Passing through a light pipe the photons strike the photocathode material of a photomultiplier and generate photoelectrons. In turn these electrons are accelerated towards dynodes where they create other electrons by secondary emission. Finally, 1 - 10 electrons will be generated for every incoming SE. The Everhart-Thornley detector is situated laterally in the specimen chamber. Hence, electrons from surfaces facing the ETD are more likely to end up in the detector and these regions appear brighter. This creates a three dimensional impression for the human eye.

In addition, a through-the-lens detector (**TLD**) is located above the final lens inside the electron column which is connected to the ETD scintillator via a light pipe. As a result of the top-view arrangement, a three dimensional impression cannot be provided. However, this detector proved to be extremely helpful in some situations, especially for the alignment of the stigmator settings at quasi-1D-deposits as discussed in detail later.

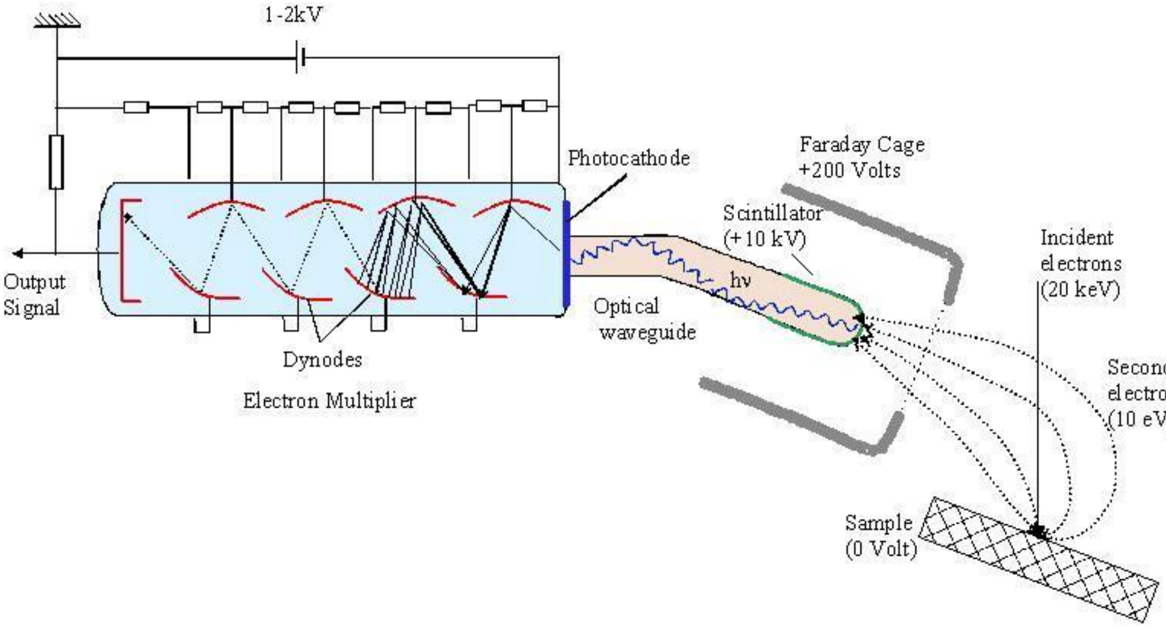

Figure 3-3: Scheme of an Everhart-Thornley detector. SEs are collected by a faraday cage and generate light at the scintillator. The photons in turn create photoelectrons at the photocathode which are multiplied in the electron multiplier and finally form the output signal[26].

Chemical analysis was performed via an energy dispersive X-ray (**EDX**) detector. X-rays striking the semiconducting material of the detector generate electron-hole pairs that are separated by an external electric field. The energy of the incoming X-ray is proportional to the number of the produced charge carriers i.e. to the generated signal.

3.1.2 Focused Ion Beam Microscope - FIB

The used ion beam consisted of Ga^+ particles stemming from a reservoir heated above the melting point. Essential parts of the ion column can be seen in Figure 3-4 (left). A typical liquid metal ion source works as follows: due to gravity assisted wetting the liquid metal coats a tungsten tip and forms a Taylor cone by the application of a strong electric field opposing the surface tension. Gallium atoms start to evaporate and are ionized around the lower end of the cone since this area exhibits the highest curvature and potential gradient. An extractor electrode attracts the Ga^+ ions and a subsequent beam acceptance aperture grips the central part of the beam (Figure 3-4, right). Furthermore, a system of apertures and lenses collimates and de-magnifies the ion beam. Acceleration voltages from 5 kV to 30 kV are possible as well as beam currents from 0.15 pA to 20 000 pA. Coils in the lower part of the column are used for the axial astigmatism correction and the FIB deflection to scan the specimen surface.

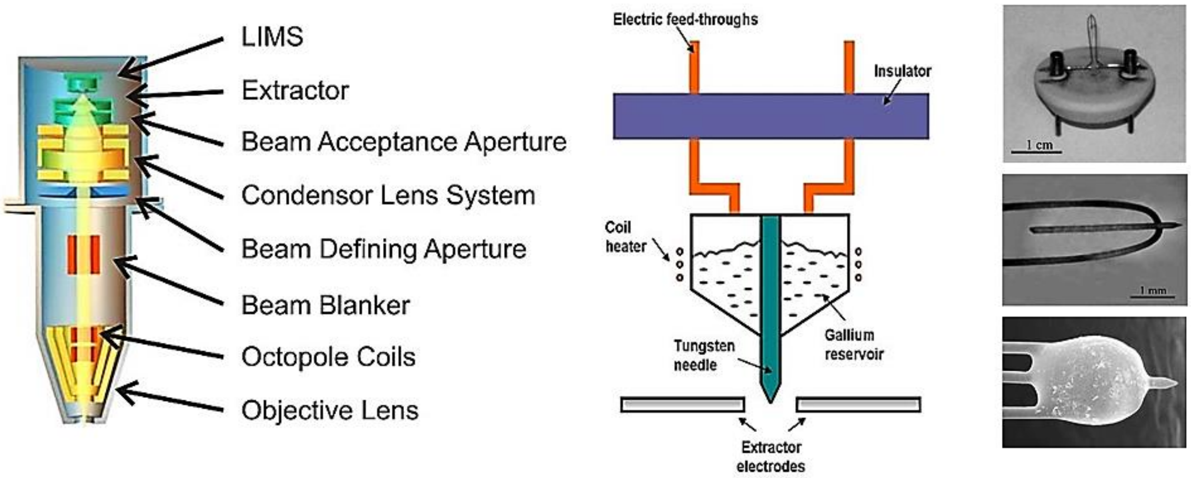

Figure 3-4: Main components of an ion column (left) and schematic design of a liquid ion metal source (center). On the right hand side, one can see a LMIS socket with filament (top), the apex region of this filament with the tungsten needle (center) and the filament filled with a droplet of liquid metal.[8,27]

The penetration depth of ions is significantly decreased due to the larger diameters of ion compared to electrons. This leads to a reduced spatial expansion of the interaction volume. The mass of Ga^+ ions is considerably higher than those of electrons (by a factor of $\approx 10^6$). As the energy is therefore much higher for a given primary acceleration voltage, the impinging ions lead to massive phonon generation (heating) which evaporates material at the beam center and further removes material via cascade effects in the proximity. This is called sputtering and the bases for subtractive FIB structuring. Detailed consideration can be found in literature[1,28]. Beside the surface emission of atoms, ions and clusters, strong cascades of SEs are entailed which are used as imaging signals during FIB imaging or SEM assisted FIB processing.

3.1.3 Eucentric Height

The ion column of the used FIB Nova 200 was tilted by 52° relative to the electron beam. The focal points of both beams met in one spot. The corresponding z-coordinate was called eucentric height and equivalent to the working distance, i.e. the distance between the lower pole piece of the electron column and the specimen. The working distance for the used DBM was approximately 5 mm. In order to enable tilting of the specimen without a major deviation of the imaged area on the one hand, and the simultaneous use of both the electron and ion beam on the other hand, the specimen surface had to be adjusted to the eucentric height. As the entire GIS setup was aligned to this height, it was also inevitable for FEBID applications.

3.1.4 Gaseous Precursor

The used precursor was trimethyl-methylcyclopentadienyl-platinum (Me_3MeCpPt) consisting of a central platinum atom with four hydrocarbon ligands, schematically shown in Figure 3-5. In addition, Table 3-1 reveals some fundamental physical properties.

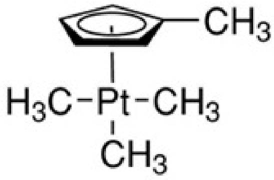

Figure 3-5: Chemical structure of trimethyl-methylcyclopentadienyl-platinum.[29]

Table 3-1: Summarized properties of used precursor gas.[30]

Color and form	off white powder
Molecular weight	319.32 g / mol
Melting point	30 – 31 °C
Boiling point	23°C at 0.053 Torr
Vapour pressure	0.2 Torr at 35°C, 0.053 Torr
Specific gravity	1.88
Odor	metallic
Solubility in water	insoluble

The plurality of ligands implicates a sophisticated dissociation process for this precursor molecule as the dissociation is not only a single electron based event. In detail, tens of electron-molecule interactions[6,31] have to take place for complete dissociation. The highest dissociation cross section for this precursor molecule can be found for electron energy of around 200 eV[6,31]. This explains the high affinity to low energy electrons (SE_I, SE_{II}, and SE_{III}). Due to the highly dynamic situation during deposition and replenishment, entirely pure Pt deposits are complicated to accomplish[6]. This implies a problematical conflict: An insufficient number of electrons would not imply a complete dissociation (ELR) leading to incorporation of incompletely dissociated precursor fragments[14]. On the other hand, a strong excess of electrons (MLR conditions) leads to polymerization effects of precursor fragments such as di-pentadiene which is barely volatile. This situation leads again to increased carbon contents (Figure 3-6). Even a balanced situation between pure MLR and ELR conditions does not provide completely carbon free deposits as the highly dynamic replenishment comes into play. Thus, deposition processes ultimately end up in small Pt nano-crystals crystals (1.5 – 3 nm), which are condensed in a disordered, loosely linked carbon matrix. Although considered as unwanted effect, this internal structure can be used as enormous advantage for e.g. sensor applications[32] due to the spatially homogeneous distribution of metallic nano-crystals in a widely insulating matrix.

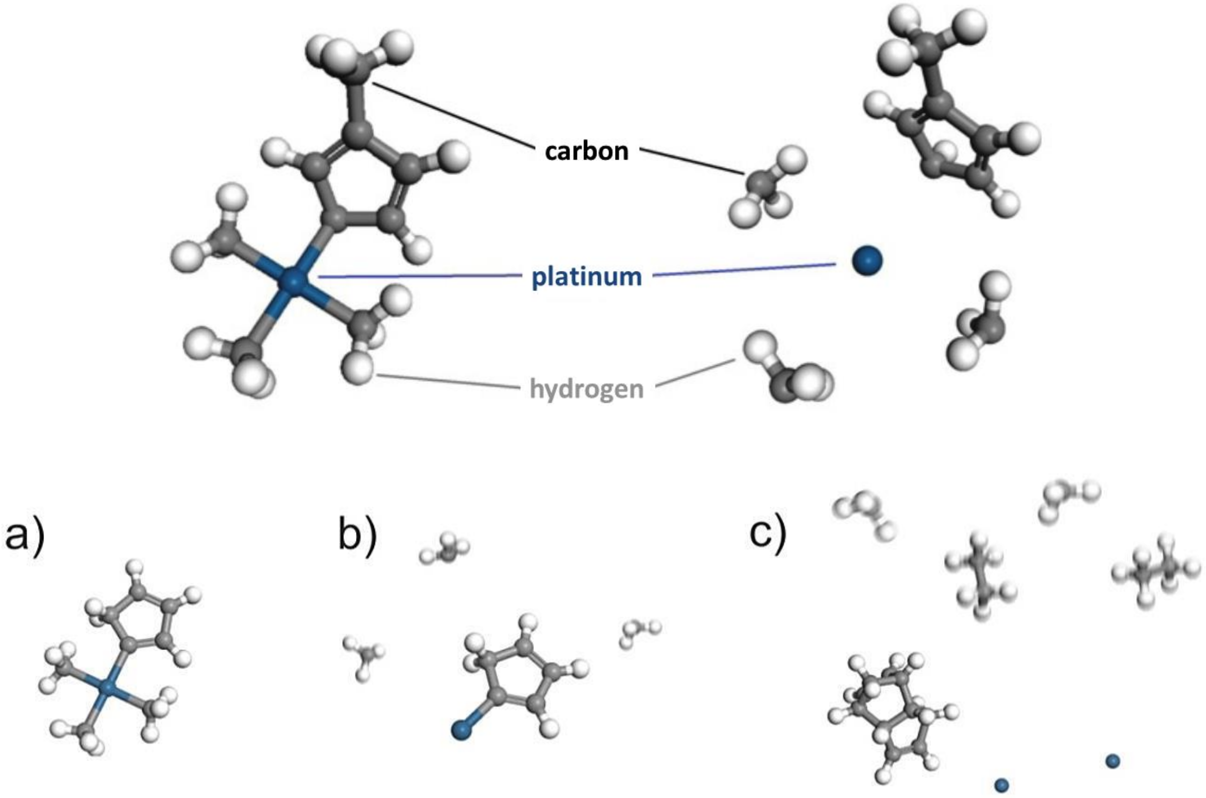

Figure 3-6: Ideal dissociation procedure of used precursor molecules into single fragments (top). In practice (bottom), the precursor molecule (a) gets either partially dissociated (b), which is typical for ELR conditions or, considering MLR conditions, all bonds from the central platinum ligand are broken and the platinum builds the deposit together with C-H-fragments polymerized because of the overspill of electrons.[8]

Figure 3-7 shows the typical composition of FEBID materials imaged via transmission electron microscopy (**TEM**). The separation into Pt grains (dark) and a surrounding highly defected carbon matrix (bright) is clearly evident. The used precursor typically provides 10 - 20 at.% Pt depending on the preparation conditions[7,14]. The consequence of the appearing carbon contamination are manifold, e.g. a reduced thermal and electrical conductivity or a reduced stiffness. Although complete post-growth purification has recently been demonstrated [22,33,34] a much more interesting approach for property tuning has been revealed by Plank et al.: post growth e-beam curing[34]. This procedure is capable of finalizing incomplete dissociation leading to slight growth of Pt grains in the range of 5 Å while center-to-center distances of individual Pt crystals remain the same. This naturally affects material properties like the electrical conductivity[34] (variable tunnelling barriers) or mechanical stiffness[22] (3D percolation system). However, ELR conditions are needed at fabrication to obtain strong effects of post growth treatment[34]. Thus, this specific nano-crystalline structure with an enhanced carbon percentage may entail some minor inconveniences we also have to face with in this thesis, especially because of the reduced electrical conductivity. However, in case of resonating applications the positive effects outweigh these drawbacks since the increased elasticity and reduced stiffness is an inevitable prerequisite to enable noticeable deflections or oscillations of a FEBID nano-structure at moderate voltages and frequencies respectively. Nevertheless, the use of ELR conditions is inevitable to enable effective post growth e-beam curing, it was important to extensively investigate influences of deposition parameters on geometry and chemical composition of resonating structures in order to determine suitable ones for the particular demands of this thesis.

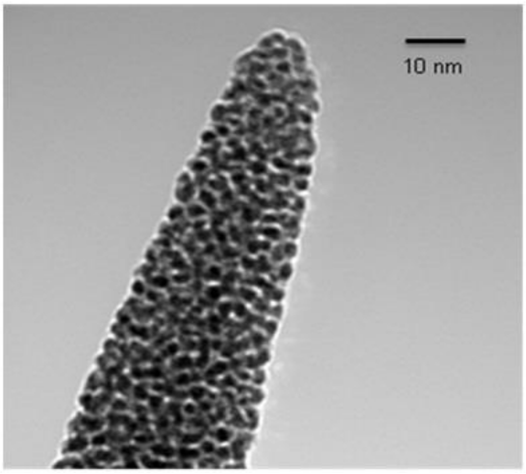

Figure 3-7: Bright field TEM image of a nano-pillar tip region fabricated via FEBID.[8]

3.1.5 Patterning

There are three approaches to assign a pattern to the electron or ion beam:

- Default geometries of the internal patterning generator
- Import of a bitmap (.bmp file)
- Import of a streamfile (.str file)

The internal patterning generator provides a large variety of possible geometries e.g. circles, rectangles, polygons…, and allows the individual tuning of different patterning settings for each pattern. The most important ones varied from experiment to experiment are:

- X/Y size: dimension of the pattern along the horizontal and vertical axis in unit length
- X/Y point pitch (**PoP**): distance between two successive points exposed by the beam
- Dwell time (**DT**): pulse duration per pixel
- Passes: number of loops the beam scans along the given pattern
- Refresh Time (**RT**): time between two consecutive passes
- Scan Type: defines if the scanning pursues a serpentine or raster strategy
- Scan direction: sets the edge of the pattern the beam scans towards
- Gas Type: sets the kind of precursor molecules used for deposition

Most of these settings are also adjustable via bitmap and streamfile patterns. Nevertheless, these two file types contain some information recognised by the patterning generator. For bitmaps, each pixel contains RGB values between 0 and 255. The blue component sets the dwell time of the pixel. A maximum value of 255 corresponds to the dwell time defined by the user in the patterning settings. 0 equates a minimum value of 100 ns per spot. The beam is blanked if the green component is different to 0. The value of "Red" is ignored. As a result, each pixel of a black area will be exposed to the electron or ion beam for a period of 100 ns. White areas would be left out, as the green component is unequal to 0. The point pitch is naturally defined by the ratio of size and pixels of the bitmap but can be limited by the minimal point pitch of the patterning engine. Although the sequence represents a decisive factor for image transfer it is only slightly variable which often prevents ideal results. In order to overcome these limitations the streamfile approach is available which overrules any DBM patterning component and directly communicates with the scan coils. These advantages make ASCII files to the method of choice for complex patterns. Streamfiles are separated into a four-line-header and command lines. The header assigns important information to the patterning engine. The "s" in the first line defines an ASCII file as a stream file for the patterning engine and the following number indicates the resolution (optional). The FIB Nova 200 offers a resolution of 16 bit. The value in the second line is referred to the number of passes and the third line provides the total number of command lines beneath that is limited to 8 million. A command line consists of up to 4 columns, whereas the last one is not necessarily specified. The first column contains the dwell time for the specific pixel whose position is defined by the values given in the second (X-coordinate in pixel) and third column (Y-coordinate in pixel). The coordinates in unit length naturally depend on the total number of pixel and the used magnification. The beam blanking status is specified in the fourth, optional column. 0 corresponds to a blanked beam, 1 to an unblanked beam. An example for a streamfile used in this thesis can be seen in Figure 3-8. More complex streamfiles were created by a streamfile generator designed and programmed by Robert Winkler. Further information to this programme can be obtained from his Master Thesis[35].

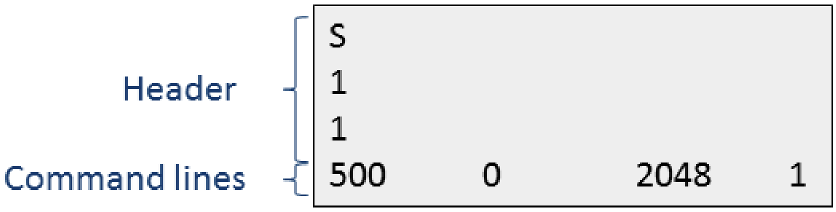

```
S
1
1
500      0         2048      1
```

Figure 3-8: Easy example of a streamfile. "S" indicates the stream file and "1" in the second line determines that the command line part should be performed once. "1" in the third line contains the number of command lines, in this case, one line, which is given beneath. The command line tells the patterning engine, that a point with coordinates (0/2048) pixel should be exposed to the electron beam for 500 µs. The beam shall be unblanked ("1").

4 Experimental Sequence and Additional Instrumentation

4.1 Resonator Characterization

As a first step, it was inevitable to gather a comprehensive insight into the mechanical, chemical and physical behavior of the resonating structure to find suitable parameters for further applications.

4.1.1 Fabrication

For a resonating system excited electromechanically by an AC field, two components are required: ***1)*** an exciting counter electrode and ***2)*** a resonating structure responding on the electric field applied on the counter electrode. In the following the preparation procedures are discussed to clarify the setup and its implications on the experiments and simulations.

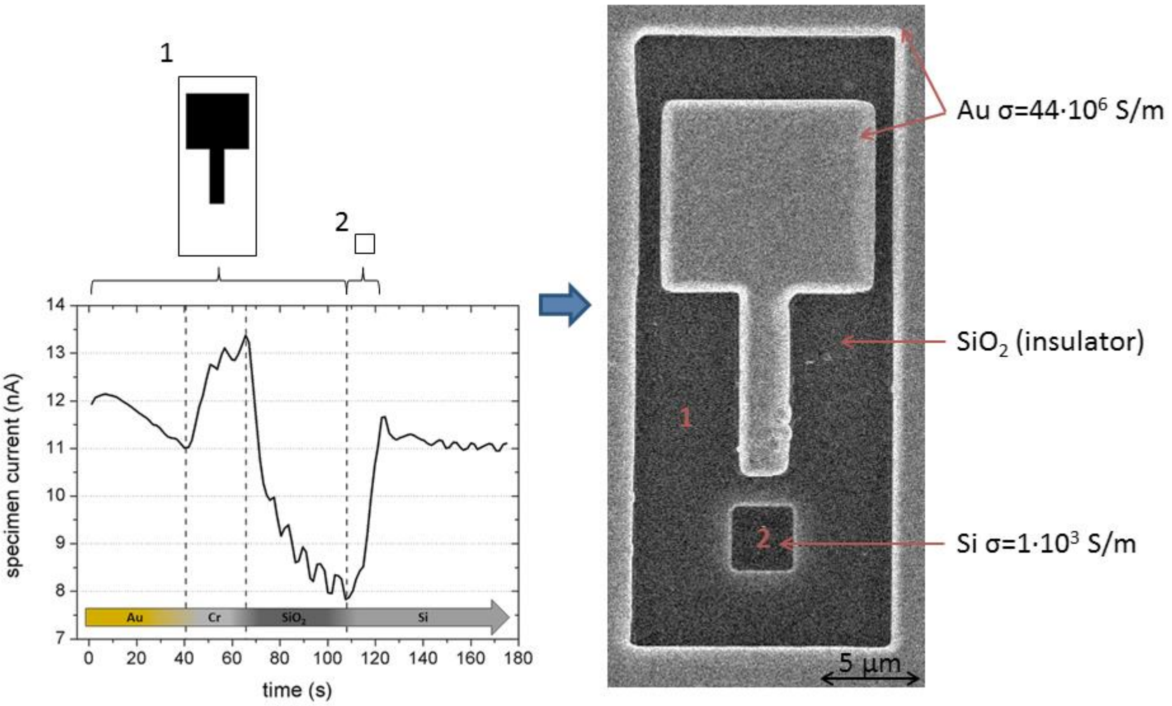

Figure 4-1: Time dependent specimen current during FIB processing (bottom left). The current is increased at materials with enhanced electrical conductivity. The first pattern removes material around the electrode (pattern 1) until the insulating SiO_2 is reached. Pattern number 2 sputters the insulating material on top of the substrate across a squared area in front of the electrode. A SEM image reveals the resulting electrode structure (right).

4.1.1.1 Fabrication of the Exciting Electrode and Surrounding Geometry

The used sample platform consists of a silicon (Si) substrate with an insulating layer of 500 nm silicon dioxide (SiO_2). A thin coating of chromium (Cr) provides adhesion to the topmost gold (Au) layer of about 3 µm prepared via sputter coating. A bitmap given in Figure 4-1 (pattern 1, top left) was used for sputtering Au layer and Cr coating which was executed by the ion beam. As a result, the Au counter electrode was surrounded by insulating SiO_2. In front of the electrode, the insulating SiO_2 was removed by the ion beam across an area of 3 x 3 µm (pattern 2) to enable electric grounding of the resonators via depositing it on the silicon substrate (see chapter 4.1.1.2). The resulting geometry is revealed in Figure 4-1 (right). Due to differences in the electrical conductivity of respective layers, the current progress of the sputtering process could be controlled by the specimen current Figure 4-1 (bottom left). Layers of high electrical conductivity lead to an enhanced specimen current. As a result, a significant drop indicates the boundary of the conducting Au (or Cr) layer to the insulating SiO_2, whereas an increase of the specimen current occurs at the transition from SiO_2 to the silicon substrate. This monitoring allows precise control about milling depth for a reproducible layout fabrication.

4.1.1.2 Fabrication of the Resonator Itself

In the center of the squared area where the insulating layer was removed, a platinum-carbon (PtC) nano-pillar was deposited on the silicon substrate via FEBID. This pillar represents the resonating structure in the following. Hence, the two reasons suggesting the used shape of the counter electrode are obvious: Firstly, the squared area on the back facilitates making contact to the electrode and in addition, the narrow branch towards the deposit provides a sufficiently directed force on the resonator induced by the electric field. The pattern originates from the streamfile given in section 3.1.5. The total time of deposition ranged from 280 s to 650 s depending on the process parameters and target heights. In addition, electron energy and beam current were varied to determine the influence of deposition parameters on the resonators behaviour, as described in chapter 6.1.

The extreme aspect ratio of the pillar requires ***highest demands*** for ***focal setting procedure*** and ***correction of the axial astigmatism***. At first, the settings for crossover, lens alignment, focus and stigmator were adjusted according to common proceeding until the highest possible resolution achievable with these strategies was reached. Remaining astigmatism can be identified via successive focusing and defocussing. Afterwards, this standard approach has to be followed by a much more complex focusing and stigmator setting strategy to achieve optimum settings required for quasi-1D-deposition.

High end focusing strategy

Single Pt test pillars were deposited with TETs of only 5 s. Hence, it is more precise to speak about test points instead of pillars. In further parts of the thesis we define ***test spots*** as single point deposits with a TET of 5 s maximum and we refer to ***pillars*** or ***resonators*** as single point deposits with TETs of a few hundred seconds leading to pillar heights of a few µm. The sharp borders of this test point can be used as perfectly fitting object for focusing as the Pt spot deposit appears bright in SEM imaging and therefore highly stands out against the dark Si background.

High end stigmator setting strategy

A second and even more important feature of these test points is that their shape represents the current quality of stigmator settings. The reason for that is obvious: If the electron beam is influenced by axial astigmatism this deviation is naturally reflected in deposition and theoretically circular test points exhibit elliptic shapes after deposition. As a result, an almost circular shape of test points is an initial indicator for good stigmator settings. In order to achieve that, x- and y-stigmator settings were varied independently in smallest possible step sizes. At the used FIB Nova 200, the stigmator settings along stigmator's x-direction controlled axial astigmatism of the electron beam along diagonal axes (45°, 135°, 225° and 315°), stigmator settings in y-axis corrected occurring astigmatism along the horizontal and the vertical axis. As empirically observed, the finding of good stigmator settings for the x-direction used to be less complex and time expensive than adjusting the y-stigmator. Hence, the x-stigmator was previously adjusted and the current settings controlled in a first way via focusing/defocusing a test spot. Afterwards, the y-stigmator has to be adjusted. As changes in the y-stigmator might also affect the x-stigmator, the x-stigmator had to be re-adjusted from time to time. Occasionally deposited test points reflected the quality of current stigmator settings. This procedure was performed until a circular shape of test point deposits was reached. However, the shape as controlling feature is a necessity but not a sufficiency for best stigmator settings. The final quality factor is given by the test points' diameter, which turned out to be highly sensitive to changes in stigmator settings. By that, stigmator settings providing a virtually circular test point were successively varied by smallest possible steps in each of all four directions. After each change, a test point was deposited and its diameter was measured. As re-deposition and related effects induced by electron beam exposure broadened the test point, the quality features shape and especially the diameter can only be reliably evaluated after minimal exposure to the electron beam. Despite changes in stigmator settings were minimal they caused significant changes in diameters of 2-5 nm around optimal settings. Finally, best stigmator settings were given by test points with ***smallest diameter*** and simultaneously an almost ***rotationally symmetric shape***.

As a small summary, we can state that the fabrication of quasi-1D resonators is highly complex and affords a conscientious and thoroughly performed adjustment of beam settings. Focus and stigmator settings were adjusted with the help of test spots, i.e. single spot deposits with TET of 5 s. The focus could be aligned highly precise and reproducible via these test points, whereas stigmator settings were extremely sensitive and had a great influence on the deposit's diameter.

4.1.2 Experimental Measurements

4.1.2.1 Electrostatic Deflection

In order to determine the ***pillar's deflection*** with respect to an applied DC voltage, the Au counter electrode was contacted via micro-manipulator OmniProbe 200 by Oxford instruments®,[36]. This device consists of a fine tungsten tip with an end radius in the lower micron range and can be moved along three axes. What is more, manipulating is completely independent from the microscope's stage position. The voltage was supplied to the micro-manipulator by a Keithley® 230 programmable voltage source and typically ranged from -30 V to +30 V. As the deposit was connected to the substrate, there was a potential difference between pillar and counter electrode. The occurring electrostatic force led to bending of the structure towards the counter electrode. The maximum deflection of the resonator was measured in top view via SEM images. It was important to capture frames used for deflection measurements with a minimal exposure time at a satisfying image quality (low pixel, single frame with 100 ns DT). Otherwise the bombardment of electrons might lead to charging of the deposit due to its bad electrical conductivity which would change the electrostatic force between the counter electrode and the pillar. Several deflections were measured at different voltages to increase the reliability of statistics.

4.1.2.2 Resonance Frequency

The finding of the intrinsic ***resonance frequency*** of the resonating structure is an essential task of this thesis. For that purpose, the Au counter electrode was connected to a Picoscope 3204A computer oscilloscope[37] via OmniProbe micro-manipulator. If the exciting frequency of the ACV field matches the intrinsic resonance frequency of the deposit, the resonator reveals an obvious oscillation detectable by the SEM image (Figure 4-2). The voltage range of the oscilloscope was up to ±2 V at a maximum frequency of 1 MHz. It was operated by the graphical user interface (**GUI**) of a LabView® 2013 program designed by Martin Stermitz which enables easy adjusting of settings like voltage, frequency and wave form. Additionally, it is possible to use several modes of frequency sweeps, tunable in range and speed. Detailed information can be derived from his master thesis[22].

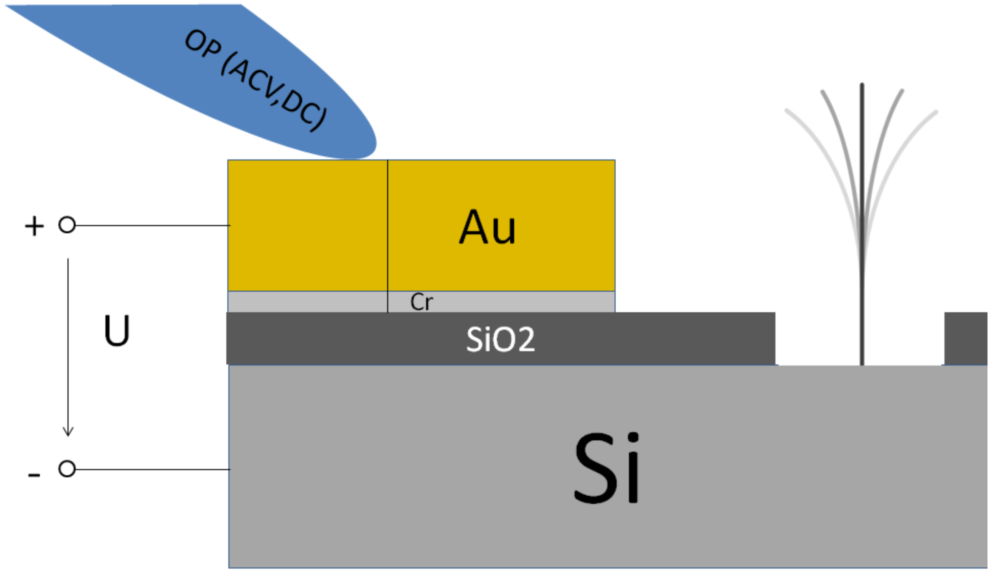

Figure 4-2: Side view scheme of the measurement setup for electro(-dynamic) stimulation. The resonator is deposited on the grounded silicon substrate. The micro-manipulator OmniProbe 200 contacted the 3 µm Au counter electrode insulated from the substrate by a 500 nm SiO_2 layer.

4.1.2.3 Geometrical Investigation

As deflection and resonance frequency both depends on the shape and dimension of the resonating structure, geometrical characterization is inevitable. The stage has to be tilted to the maximum angle of 52° to access a side view of the pillar and enable reliable measurements of the vertical resonator. ***Heights*** were measured at least three times per deposit using the arithmetic mean. The width of the structure varied due to different working regimes during deposition. This is obvious, as at enhanced heights (according to literature[14] approximately 2 µm) the precursor molecules can hardly diffuse from the substrate (***SDR***) surface but may only be absorbed from the gas flux (***GFR***). Hence, ***width*** measurements were executed at least every 500 nm, which is approximately a tenth of a pillar's height. All these length measurements were performed on SEM images via the internal measuring routine. In addition, the counter electrode and surrounding areas were measured in order to completely reproduce the physical conditions in simulations.

4.1.2.4 Post Growth Treatment (Curing)

Exposing the deposits to PE energies initiates several processes inside the structure and is commonly known as post growth treatment (**PGT**). PGT was performed in top view across a particular pattern (Figure 4-3). The structure was kept in resonance to provide e-beam curing from both sides of the pillar along the entire length of the structure. This approach guarantees a widely constant e-beam exposure as CASINO® simulations (cf. section 1.6) suggest a penetration depth of about 3 – 5 µm for high energy 30 keV electrons in similar material consisting of 15 - 20 at.% Pt. Furthermore, high energy electrons less likely interact with FEBID deposits. Using lower primary electron energies led to highly undesired deformation of the quasi-1D structure due to the smaller interaction volume and thereby higher local electron densities within the pillars. Similar behavior could also be observed for too high beam current leading to the same effect concerning local electron densities. On the other hand, higher beam currents increase the curing efficiency. Thus, highest possible current where no pillar bending occurred was chosen for PGT: 44 pA at 30 keV. The exciting frequency of the electromagnetic field had to be permanently adjusted, since the resonance frequency of the pillar increases during curing. All curing processes were performed for 3600 s.

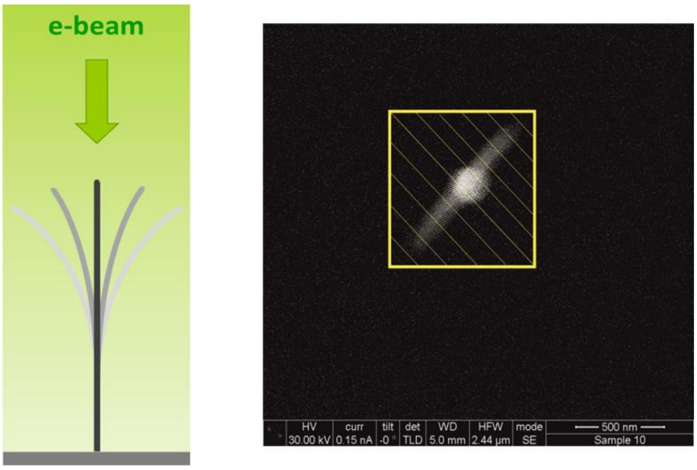

Figure 4-3: Scheme of top view curing (left) and corresponding SEM image[22] (right) with indicated e-beam curing frame (yellow).

4.1.2.5 EDX Measurement

Analysis of resonators' chemical composition was carried out by a **Bruker** EDX detector mounted at the used DBM FIB Nova 200 and processed by software **Esprit**[38]. In order to minimize undesired signals from surrounding areas, crescent – shaped disc TEM grids were used as substrates for EDX measurements. Due to its small thickness of about 10 µm this grid contributes in a minor way to the EDX spectrum than other substrates, e.g. wafer-like samples. 26 pillars were deposited with different beam setting on the grid (Figure 4-4). The e-beam scanned only a small area in the upper third section of the quasi-1D resonator in order to receive similar precursor regimes independent of the electron energy, i.e. the interaction volume.

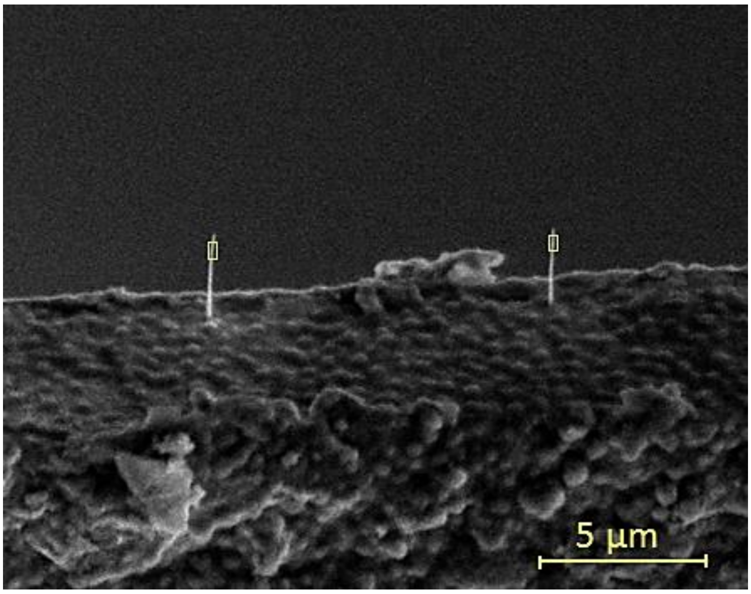

Figure 4-4: Two 30 keV / 21 pA pillars on the used TEM grid with a minimal distance of 10 µm in between. The area used for EDX measurements is marked by a yellow rectangle.

4.1.3 Further Procedure and Analysis

For crystals, bending is directly related to a changed distance between neighboring atoms inside. As a consequence, the interatomic bonds determine the strength of forces opposing a deflection. In turn, the knowledge of macroscopic material quantities might give a better insight and understanding of the internal structure and is therefore an important approach for the characterization of quasi-1D nano-resonators. For two phase PtC materials the situation is more complex due to the nano-scaled metal-matrix composition which will be discussed later in detail. In general, the stiffness of a pillar opposes the electrostatic force between counter electrode and resonator. ***Young's modulus*** is a quantity which describes the tensile elastic deformation with respect to the applied force and is the ratio of tensile stress and tensile strain. Hence, it is a parameter used to quantify the elastic properties of a material independent of unit length and represents an internal material quantity. According to beam theory described in detail in chapter 5.1.1 the bending moment $\boldsymbol{M}$ equals

$$M = EI\frac{\partial^2 x}{\partial z^2} \tag{4.1}$$

with Young's modulus $\boldsymbol{E}$ and $\boldsymbol{I}$ the area moment of inertia about the axis of interest. The last term indicates the curvature along the beam height $\boldsymbol{z}$. Hence, Young's modulus is directly related to the bending stiffness. As shear deformation can be neglected for large relations between height and length (also cf. 5.1.1), Young's modulus along the main axis can directly be calculated from bending experiments. In this case, the stress is caused by the

electrostatic force, and the strain is induced by the pillar's deflection. As both parameters are accessible by measurements of deflection, it is possible to calculate Young's modulus.
For this purpose, simulations made by finite element analysis software COMSOL Multiphysics® (version 4.3b) were integrated in a Matlab® (2013a) code, including a GUI. It was basically designed by Martin Stermitz and modified and improved in accuracy as part of this thesis[22]. The calculation bases on three successive steps:

1. *Creation of deflected pillar, counter electrode and the surrounding geometry including material properties like the dielectric constant.*
2. *Calculating the electrostatic forces on the deflected pillar by applying a DC voltage on the counter electrode.*
3. *Calculation of Young's modulus in an iterative process by comparing acting forces (stress) with the revealed deflection (strain) via equation* (2.1)*.*

Please note that, as in all simulations, several simplifications and approximations had to be made. The most important ones should be mentioned:

- *The pillar's geometry was assumed to be cylindrical with a mean diameter gathered from width experiments, although the diameter changes up to 40 % with highest diameters at bottom and top.*
- *Gravity was neglected.*

However, these assumptions weren't made thoughtlessly but appeared to be appropriate. At first, the pillar's diameter was widely constant along the main axis. All analyzed resonators with heights of approximately 5 µm only revealed a significant increase in diameter at the bottom tenth as well as the topmost area. Secondly, the influence of gravity is comparatively small due to the nano-scale dimensions and the high voltages applied.

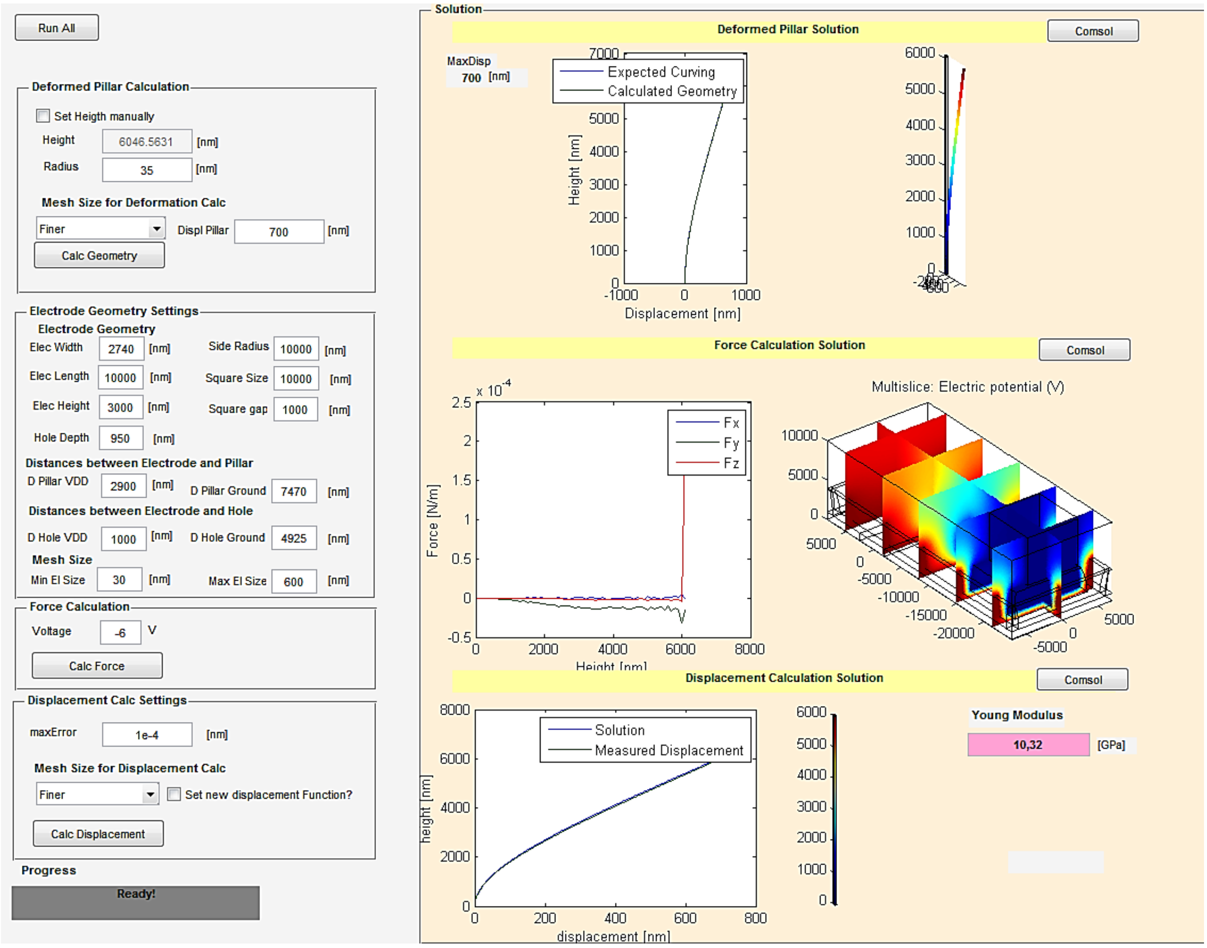

Deformed Pillar Calculation

☐ Set Heigth manually

Height 6046.5631 [nm]

Radius 35 [nm]

Mesh Size for Deformation Calc: Finer

Displ Pillar 700 [nm]

Electrode Geometry Settings

Electrode Geometry

Elec Width 2740 [nm]; Side Radius 10000 [nm]

Elec Length 10000 [nm]; Square Size 10000 [nm]

Elec Height 3000 [nm]; Square gap 1000 [nm]

Hole Depth 950 [nm]

Distances between Electrode and Pillar

D Pillar VDD 2900 [nm]; D Pillar Ground 7470 [nm]

Distances between Electrode and Hole

D Hole VDD 1000 [nm]; D Hole Ground 4925 [nm]

Mesh Size

Min El Size 30 [nm]; Max El Size 600 [nm]

Force Calculation

Voltage -6 V

Displacement Calc Settings

maxError 1e-4 [nm]

Mesh Size for Displacement Calc: Finer

☐ Set new displacement Function?

Progress: Ready!

MaxDisp 700 [nm]

Young Modulus 10,32 [GPa]

Figure 4-5: GUI of the corresponding Matlab® program with integrated COMSOL® simulations[22].

The corresponding GUI including all variable parameters assigned to COMSOL® simulations is given in Figure 4-5. The cylindrical deposit's height and radius and the revealed maximum deflection are the determining quantities for the creation of the bended pillar (step 1). Size and position of the surrounding boundaries and the counter electrode have to be defined by several distance parameters visually explained in Figure 4-6. An important factor influencing the force on the pillar is naturally the front area's shape of the counter electrode, as it is closest to the pillar. Hence, the largest force on the resonator emanates from this area. On that account, the front of each electrode was individually measured and the parameter "side radius", which defines the curvature of the vertical edges, was adjusted in the simulation in a way that simulated front geometries exactly match their real shapes (Figure 6-17).

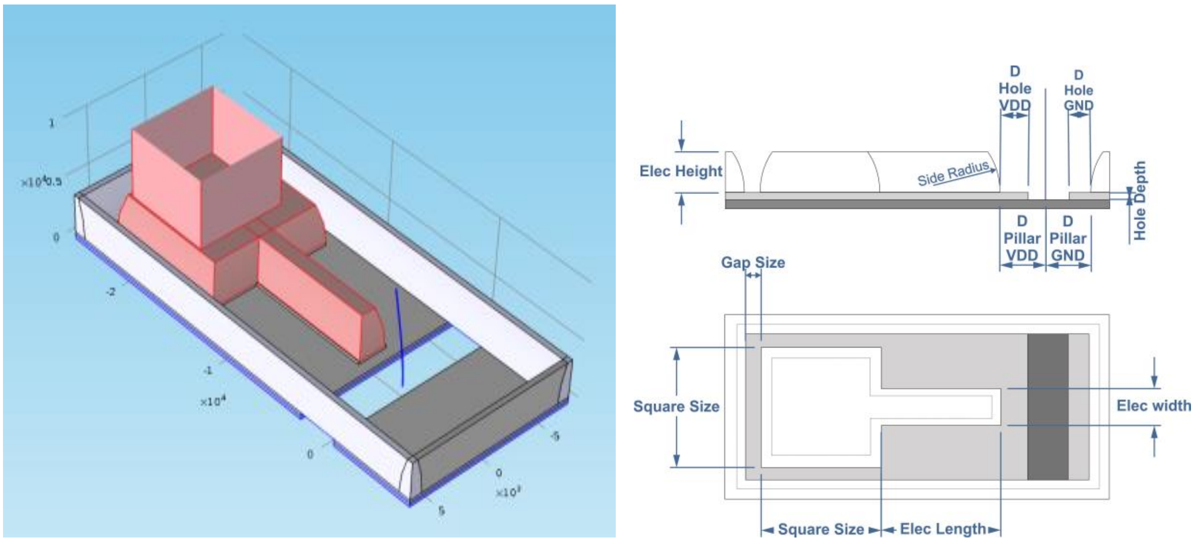

Figure 4-6: Simulated geometry of the experimentally investigated structure (left). The high terminal is marked red (the cube on top represents the OmniProbe® micro-manipulator); conductors on ground potential are given in blue. Both terminals are separated by the SiO_2 layer in between. The geometrical parameters changeable by the GUI are revealed in the plots on the right[22].

4.2 Gas Sensing Experiments with the Electron Beam

Now, the focus changes from oscillation related fundamentals towards the main aim of this thesis: The application of oscillating resonators as gas sensing elements. For that, emphasis has to be put on relative resonance shifts during varying ambient gases instead of absolute values. In the following the general procedure is described in detail.

4.2.1 Fabrication

A different sample was used in this experimental setup. Again silicon served as substrate. The metal layer with a thickness of 200 – 400 nm was separated from the substrate by an insulator of 2.5 µm which is much larger than in the specimen used before. However, the main difference is the presence of conductors pre-fabricated by reactive gas etching which spares the sputtering process described in section 4.1. A detailed description of the sample is given in Figure 4-7. The main structure of the sample can be seen on the top. It consists of 12 main electrodes, each with a conducting line heading towards the opposite electrode without being connected to it. This construct results in two parallel strips insulated from each other. The test structures are situated in the center of these lines separated by 50 µm to 100 µm and comprise four perpendicular orientated structures: The horizontal ones are connected to the strips left and right respectively. Therefore, each of them is contacted to one main electrode. The shape exhibits a triangular front section. The leading edge of the vertical electrodes (up and down) is flat. These electrodes are isolated from the conducting strips and are further referred to as minor electrodes. Hence, two opposite electrodes with their branching off conducting strips build one experimental unit with several test

structures. These sophisticated structures have gratefully been provided by the work group of Philip D. Rack at the Oak Ridge National Labs in Tennessee, US.
The quasi-1D resonators were deposited in the center of the test structure at a distance of about 2 µm to the exciting electrode (cf. 4.1.1).

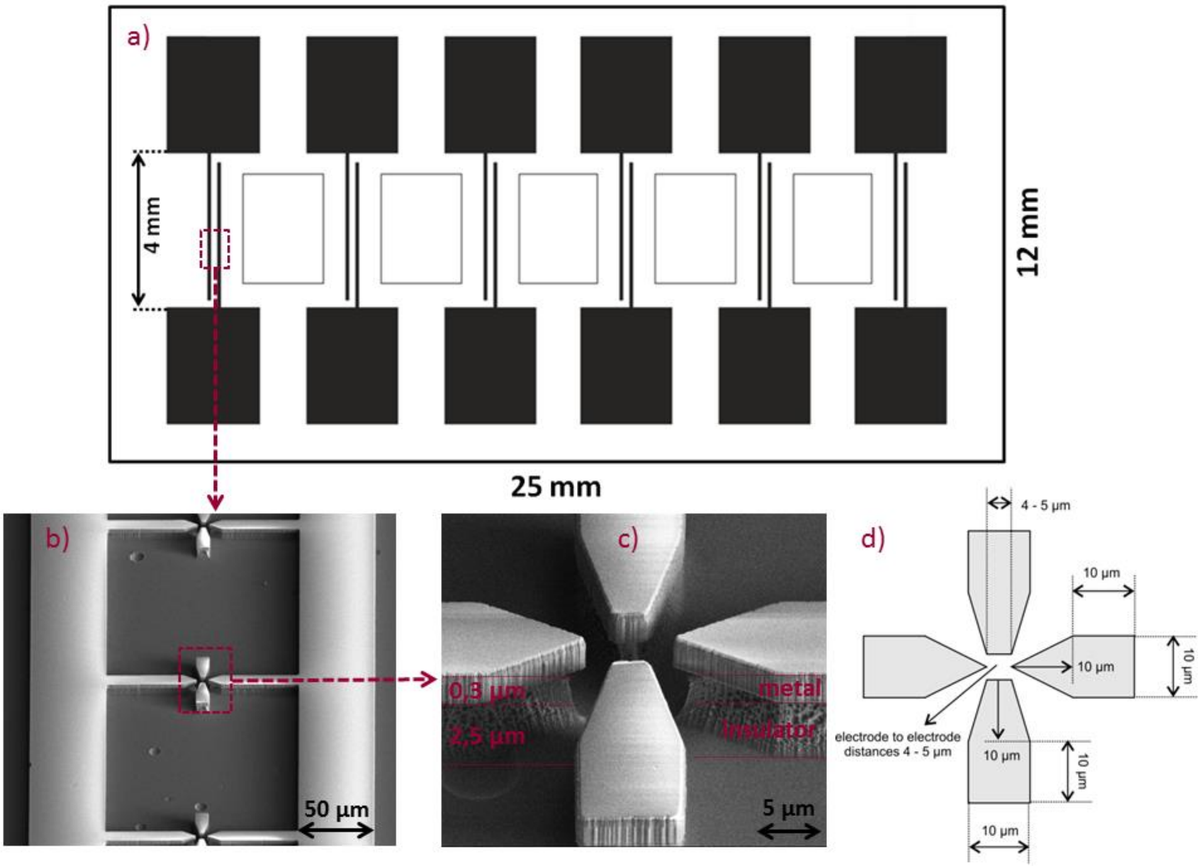

Figure 4-7: Schematic overview about the etched samples (a) including detailed SEM image of two conductors (b) and one 4-electrode-structure (c) with its dimension (d)30.

4.2.2 Active Stage

In order to apply voltages on the main electrodes with voltage / current sources and use electric measurement equipment placed outside the microscope's specimen chamber a particular stage was constructed, basically similar to that used by Stephan Michelitsch[30]. As shown in Figure 4-8, main electrodes are contacted by clamps which additionally fix the sample. Shielded coaxial cables connect these clamps to BNC connectors outside of the microscope via 25-pin D-sub sockets at the specimen chamber walls. This is enabled by a 25-pin D-SUB male-male adapter integrated in the microscope's housing. The coaxial shield was floating. An additional clamp is used to ground the silicon substrate. All connections were established by soldering.

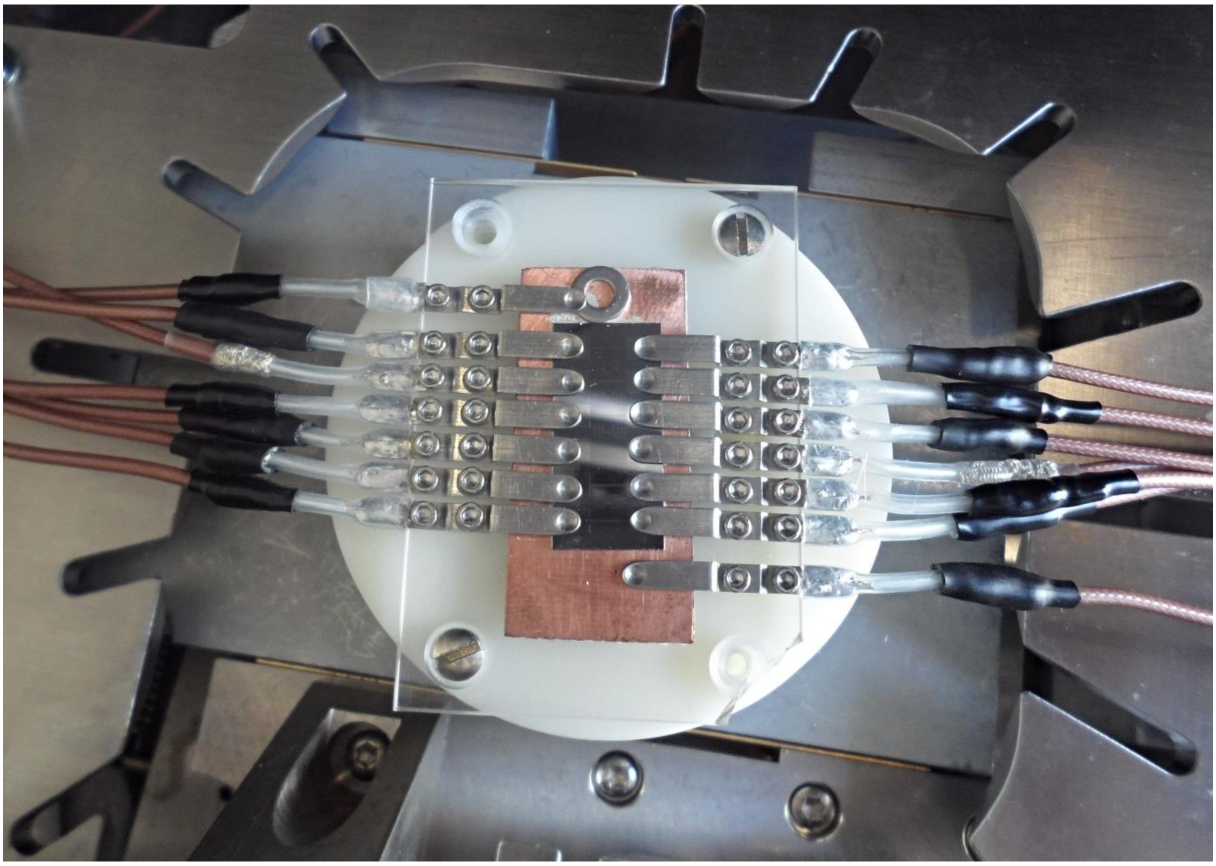

Figure 4-8: Clamps fix the specimen and contact the main electrodes. The clamp on top is connected to the substrate and put on ground potential. The further connection is established by coaxial cables.

4.2.3 Measurements

Again, the exciting AC voltage was applied by Picoscope® 3204A[37] computer oscilloscope. At resonance, frequency sweeps were performed and the pillar's oscillating behaviour was recorded by SEM movies, capturing a complete frame approximately every 300 ms. The frequency increment of the sweep was adjusted accordingly to approximately 1 kHz/s. The sweep consisted of one sweep up and a subsequent sweep down. This procedure was performed for different pressures and varying ambient gases. The gas inlet was carried out by a valve in the specimen chamber walls. The influence of several different gases on the resonance frequency of the resonator was investigated: ambient air, O_2, N_2 and SF_6. The rise in pressure inside the specimen chamber was made gently without exceeding the upper pressure limit recommended / limited by FEI. By this, an increase in pressure of one order of magnitude was possible. In order to further increase the density of gas molecules in proximity of the resonator the MM3A-EM micromanipulator by Kleindiek Nanotechnik®,[39] was used. In contrast to micro-manipulator OmniProbe[36] whose position was independent of the specimen coordinates, the MM3A-EM micromanipulator has to be mounted on the stage. However, a motion system basing on piezoelectricity enables movement in three independent directions with an excellent accuracy. In addition to a tungsten tip, which was also used to establish electrical contact with electrodes in later experiments, a fine GIS nozzle can be placed on top of the micromanipulator. A small aperture at the nozzle's tip offers two advantages: First of all, there is an isotropic gas flow in the aperture's center as it originates equally from the total edge of the aperture. Secondly and at least equally important it is possible to expose the area inside the aperture to the electron beam. Thus, the central area with the highest gas density can be monitored via SEM. In addition, the nozzle was connected to the valve integrated in the specimen chamber. This setup facilitates regulation of the gas flow and choosing the type of molecules as both can be made outside the microscope. What is more, it enables an isotropic gas flow from all sides onto the specimen's area of interest and the investigation of influences of different gases on the oscillation properties of resonators.

4.2.4 Further Procedure and Analysis

The measurements provided SEM movies with the temporal evolution of the resonator's oscillation and ranges of the simultaneously performed frequency sweeps. As a result, it is possible to associate each image revealing the momentary amplitude of the resonator with a corresponding frequency of the exciting AC voltage. This was achieved by open source ware Tracker 4.84[40] which allows the analysis of video files by the following steps:

1. *Setting of start frame and end frame at frequency sweep limits*
2. *Calibration of the lateral scale, possible by the scale provided by each SEM image*
3. *Setting of an origin in the center of the resonator*
4. *Tracking of the occurring amplitude in both directions.*

Figure 4-9 reveals the graphical interface of Tracker. According to the analytical procedure, four peaks in the amplitude, i.e. resonance frequencies, are available: One for the sweep up, one for the downsweep and for each direction of deflection.

Before performing further analysis, the arithmetic mean value of individual peaks occurring in different directions at one sweep up or down respectively was ascertained. In most cases, the maximum deflection of both peaks was in perfect agreement with respect to the frequency. In very rare occasions the peaks were separated by one frame which corresponds to about 0.75 kHz. However, this value is equal to the expected uncertainty.

Final analyzing was done by Origin® 8.5. For better understanding, this procedure is described in section 7.2.

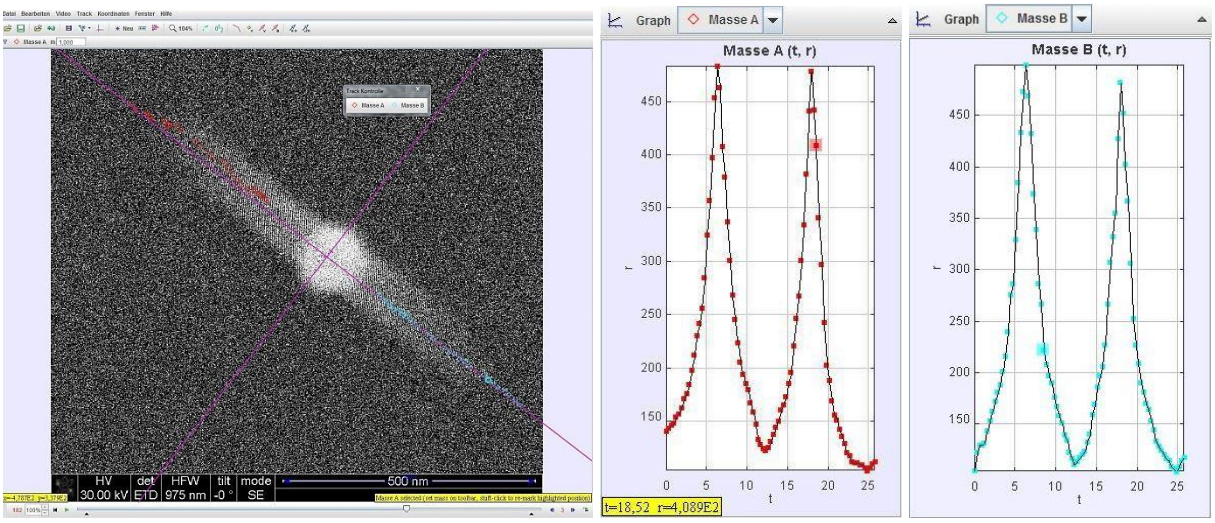

Figure 4-9: Screenshots of freeware Tracker with the corresponding amplitude in each direction. The plots reveal two peaks due to the up-and-down sweep characteristic.

4.3 Resonance Frequency Read-out without Electron Beam

Due to curing effects the presence of the electron beam shifts the resonance frequency which is intolerable when aiming for small resonance shifts. A promising approach is given by current measurements across oscillating structures in comparison with current measurements out of resonance.

4.3.1 Samples

At first, the same etched samples as for previous measurements were used (chapter 4.2.1). Afterwards, four-point structures served as samples for facilitation reasons. These structures will be described in detail in the following (chapter 4.3.2.2).

4.3.2 Tripod Structures

4.3.2.1 Etching Samples: Fabrication and Measurements

At first, tripods were deposited on etched test structures as connection between two main electrodes and one insulated electrode (cf. section 4.2.1).

Figure 4-10 shows an image of the parallel arranged structures with four electrodes whereat two of them are isolated electrodes. Tripods are always deposited between two conducting and one insulated electrodes with a pillar, i.e. resonator in the center. The branches are of equal lengths of 2.0 – 2.5 µm depending on the largest distance between the electrodes.

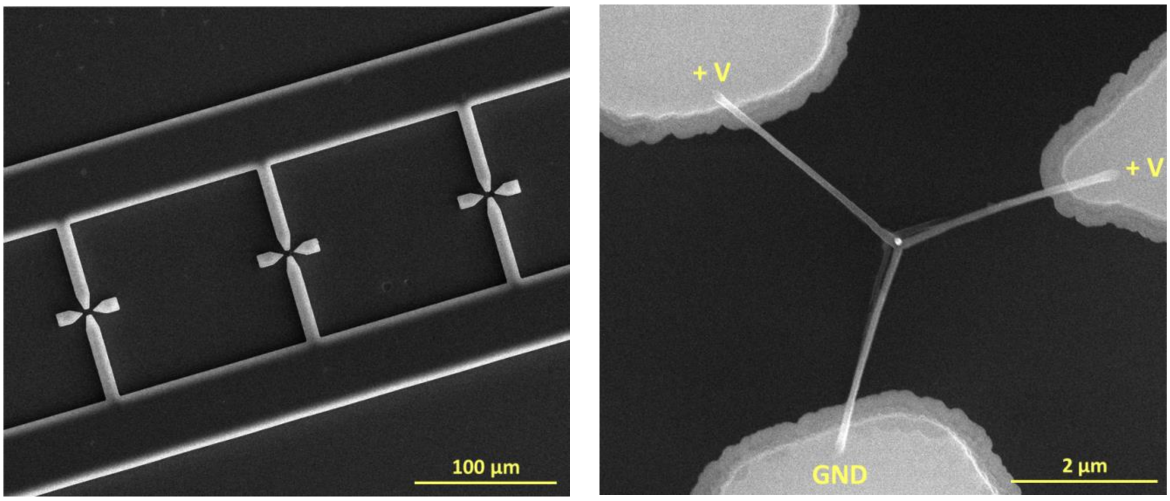

Figure 4-10: Test structures with two insulated electrodes and another two connected to the conducting paths. The Tripod connects two conducting electrodes and one insulated electrode (upper right corner). The pillar is situated in the center of the tripod and appears only as white spot (top view). In order to avoid bending of the pillar there were not captured any frames from a lateral perspective. The used connections are marked.

For investigating electrical conductivity the isolated electrode was connected via 3-axes OmniProbe micro-manipulator. The high level DC voltage was applied at the isolated electrode and one conducting electrode. The residual electrode was put on ground potential. A Keithley® voltage source 230 was used for the voltage supply. The current measurements were performed with a Keithley® Picoammeter 6485. The measuring device was controlled by a Labview program developed for that purpose (further referred to as **VI**) that accesses the Picoammeter via RS-232 interface. The interface of the VI is given in Figure 4-11. Considering again the exigency to associate the frequency data of the sweep with the temporal evolution of the measured quantity, i.e. the current, the VI offers an important feature: It returns the net measuring time (1) without initiating processes and time used for data transfer (time offset, 2). This allows bringing the time axis of current measurements in compliance with a frequency axis and enables to plot the current with respect to the frequency.

Resonance experiments with a pillar deposited onto the central point of tripod structures turned out to be highly sophisticated: As each of the branches is connected to one electrode, the residual one is to be used as exciting electrode applying the AC voltage. Thus, all four electrodes of the test structure need to be contacted. OmniProbe micromanipulator and Kleindiek® micromanipulator equipped with an OmniProbe tungsten tip instead of a nozzle were used for establishing connection to the insulated electrodes (Figure 7-14). In this setup, the left tip connected to the tripod was set on high level voltage and the right tip served as exciting electrode.

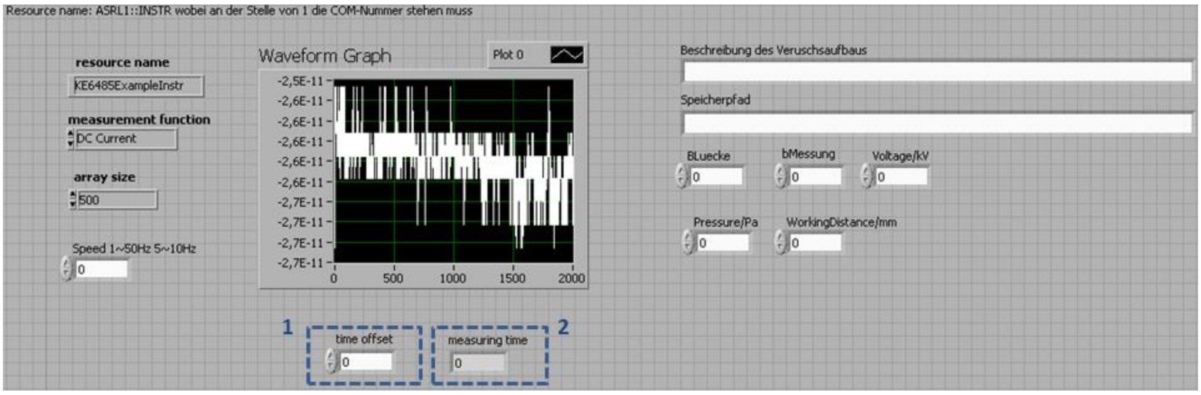

Resource name: ASRL1::INSTR wobei an der Stelle von 1 die COM-Nummer stehen muss

resource name: KE6485ExampleInstr
measurement function: DC Current
array size: 500
Speed 1~50Hz 5~10Hz: 0
Beschreibung des Veruschsaufbaus:
Speicherpfad:
BLuecke: 0
bMessung: 0
Voltage/kV: 0
Pressure/Pa: 0
WorkingDistance/mm: 0
time offset: 0
measuring time: 0

Figure 4-11: User interface of the Labview VI used for measurements with Keithley® Picoammeter 6485. The output “measuring time” (2) returns the net time interval in which data points were collected and enables to correspond each data point to a certain frequency of the exciting AC field.

4.3.2.2 Four-Point-Structures: Fabrication and Measurements

In order to facilitate the complex contacting procedure, a different specimen was used in posterior measurements. In this sample conducting strips emanate from each main electrode (yellow areas in Figure 4-13, a). Four each lead to the center of the corresponding electrodes (b) and continue in parallel lines simultaneously being insulated from each other (c). The strips’ width was equal to the distance in between and was about 2 µm. This final section of about 2.5 mm in length is intended for deposition and measurements. The position of contact electrodes (yellow) and outer dimensions (25 mm x 12 mm) are equal to the specimen fabricated by etching (section 4.2.1). Hence, electrode contact could be established by the active stage described in section 4.2.2. The name originates from the initial purpose these samples were defined for: 4-point-measurements.

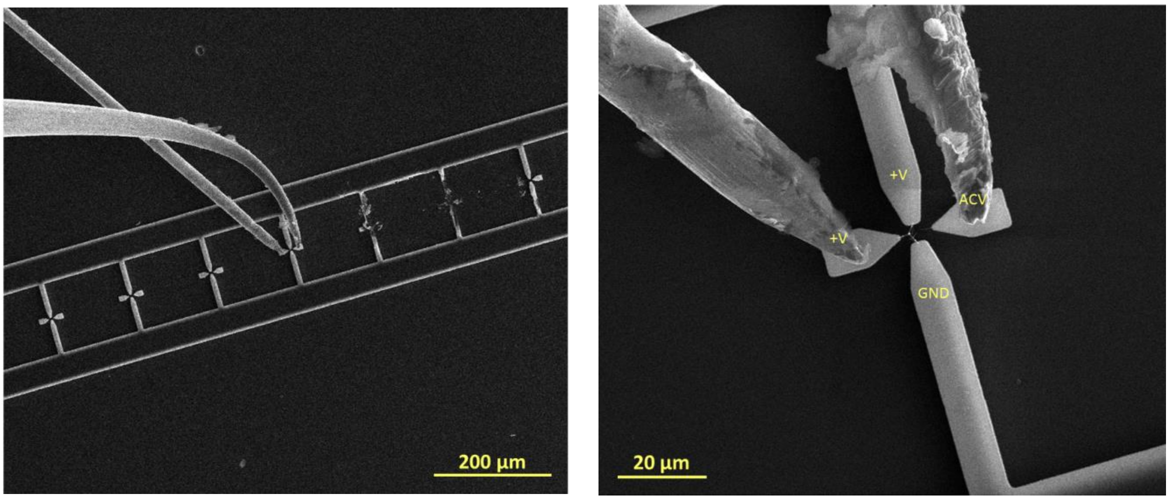

Figure 4-12: Connection of the isolated electrodes via Omniprobe® micro-manipulator and Kleindiek® GIS. The left image reveals the difficult approach, in the right image one can see the connected tips and the tripod with the resonator (white point in the center) in between.

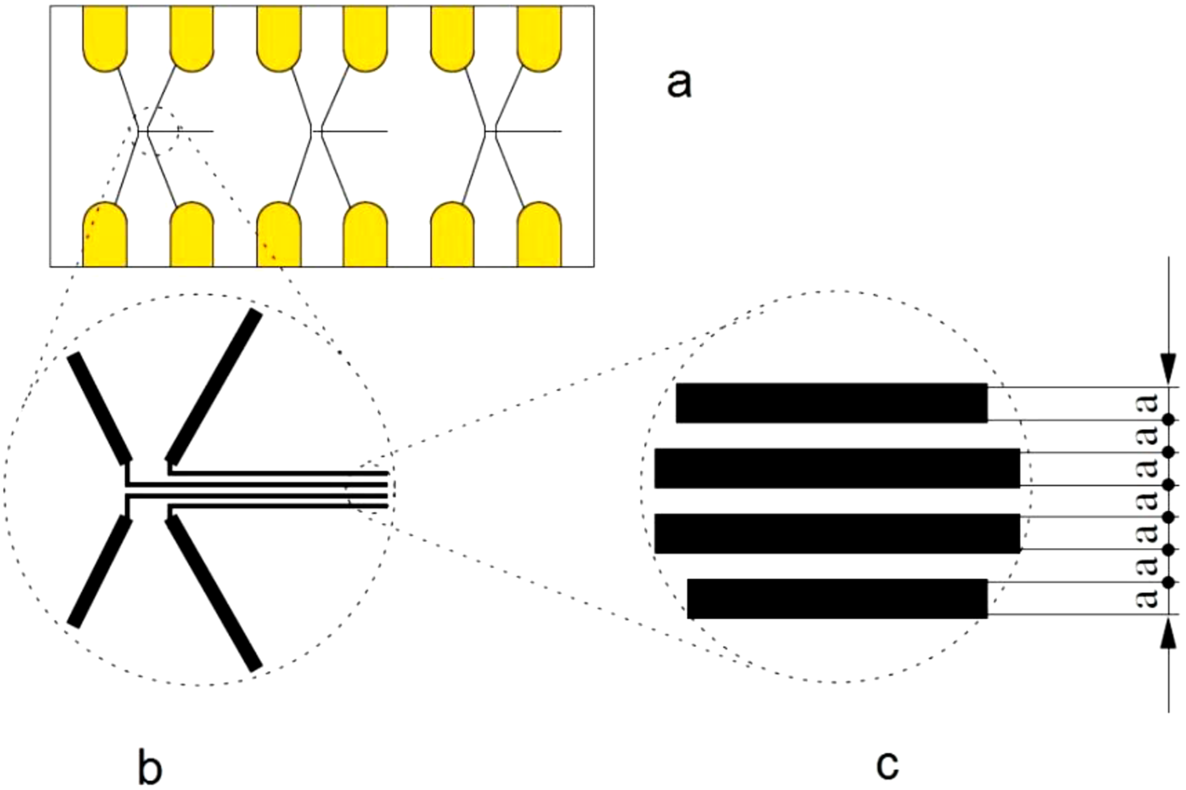

Figure 4-13: Schematic design of the used four-point-structures. Overall, there are twelve main electrodes (a), resulting in three areas the conducting strips congregate (b). The last part consisting of four parallel strips with equal width and distance (c; a = 2 µm) is used for experimentals.[30]

Different resonating structures were deposited onto adjacent conducting strips in order to close the connection between two conductors (Figure 4-14). Deposition started at the very end of the strips. This offered the advantage that connection between two conductors established by a deposit could easily be interrupted: the section comprising the deposit just had to be cut off the remaining strip by ion sputtering. Theoretically, the ion beam could also be used to destroy the deposit but this approach contains the risk of unwanted contact by parts of the disfigured deposit. Due to the use of the active stage, electrodes could be connected to voltage supply (Keithley® voltage source 230) and amperemeter (Keithley® Picoammeter 6485). The exciting AC field was applied on OmniProbe® 200 micro-manipulator via Picoscope® oscilloscope. The micro-manipulator served as electrode by approaching it sufficiently close to the resonator.

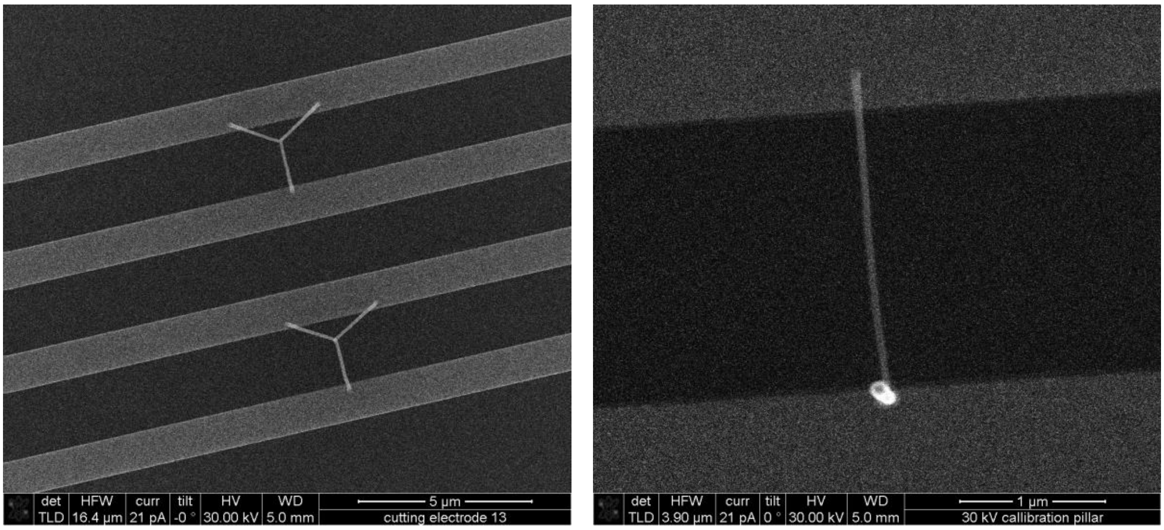

Figure 4-14: Two examples of FEBID fabricated architectures serving as connecting part between two parallel conducting strips. Tripod structures with a pillar situated in the center (left) and a pillar connected to an arch (right). Again, the high sensitivity of the architectures towards interaction with the electron beam requires that frames are only captured from top view.

5 Mathematical Background and Introduction

5.1 Elastic Beam Theories

5.1.1 Euler-Bernoulli Beam Theory

At first, we derive the expression for a quasi-cylindrical resonator concerning its resonance frequency in dependency on its material properties. A potential difference between a conducting nano-pillar and a nearby electrode leads to an electro-static / -dynamic force which leads to a deflection of the nano-pillar. Mathematically, this situation can be described by the Euler-Bernoulli beam theory[41,42] based on the following equation:

$$EI\frac{\partial^4 x}{\partial z^4} + \rho A\frac{\partial^2 x}{\partial t^2} = 0 \tag{5.1}$$

in which *z* is the symmetry axis along the pillar. The pillar's deflection occurs along the perpendicular *x*-axis. *E* is the elastic Young modulus and *I* describes the moment of Inertia about the ***beam's neutral axis***. *A* stands for the cross sectional area and *ρ* is the density of the material. There naturally occurs rotation when the beam deflects. The arising rotational inertia is neglected at Euler-Bernoulli beam theory and the cross section is assumed to be perpendicular to the bending line. The more thorough model of a Timoshenko beam accounts for a rotation between cross section and bending line arising from shear deformation. However, at high aspect ratios the deviation between these two models is insignificantly small.[43] This is obvious as elastic deformation along the bending line dominates over shear deformation if the ratio between length and thickness is high enough. Hence, regarding quasi-1D-resonators with extremely high aspect ratios according to Euler-Bernoulli is acceptable.

Assuming two independent variable of the overall solution for the deflection $x(z,t)$ one can derive a solution by the method of separation of variables. The resulting two independent ordinary differential equations are

$$\frac{\partial^4 \Psi(z)}{\partial z^4} - \frac{{\omega_n}^2}{c^2}\Psi(z) = 0 \tag{5.2}$$

$$\frac{\partial^2 \Phi(t)}{\partial t^2} + {\omega_n}^2\Phi(t) = 0 \tag{5.3}$$

The wavelength c is given by

$$c = \sqrt{\frac{EI}{\rho A}} \tag{5.4}$$

The spatial function $\Psi_n(z)$ describes the shape of the bending mode. The time dependent function $\Phi(t)$ gives the temporal response for a given mode, a classical oscillation with the respective natural resonance ω_n. Introducing the modal parameter ${\beta_n}^4 = {\omega_n}^2/c^2$ the natural resonance frequency of the system is given by

$$\omega_n = \frac{(\beta_n h)^2}{h^2}\sqrt{\frac{I}{A}\frac{E}{\rho}} \tag{5.5}$$

According to literature, the $\beta_n h$ value for the first mode of vibration of a fixed-free beam equals 1.875[41]. Before this framework can be applied to our electric setup the harmonic response of the system has to be considered in the following chapter.

5.1.2 Uniform Loaded Elastic Beam

Applying a uniform load q_0 on a fixed-free beam leads to deflection. Assuming again a negligible shear deformation (Bernoulli beam) the deflection along the transverse axis $w(x)$ at a position z can be described by the fourth order differential equation[44]

$$\frac{\partial^2}{\partial z^2}\left(EI\frac{\partial^2 d(x)}{\partial z^2}\right) = q_0 \tag{5.6}$$

with Young's modulus *E* and the area moment of inertia *I*. The product *EI* is often constant with respect to the beam's main axis and equation (5.6) becomes

$$EI\frac{\partial^4 d(x)}{\partial z^4} = q_0 \tag{5.7}$$

Assuming a constant distribution for the beam temperature and introducing a variable $\xi = z/h$ the deflection $w(x)$ is given by:

$$d(x) = \frac{q_0 \cdot h^4}{24EI}(6\xi^2 - 4\xi^3 + \xi^4) \tag{5.8}$$

The maximum deflection naturally occurs at the topmost part of the beam and equals:

$$d_{max} = \frac{q_0 \cdot h^4}{8EI} \tag{5.9}$$

5.2 Investigated Modes and Harmonics

If we consider a doubly clamped system, e.g. a guitar's string, modes and harmonics has the same shape and frequency. For higher vibration modes the standing wave gets one more knot and, as a result of a fixed beam system's boundary conditions, the frequency of the *n*th mode is *n* times the frequency of the fundamental mode. This is equivalent to the definition of harmonics. In general, however, modes and harmonics are different, like for an oscillating pillar, which is equivalent to a cylindrical cantilever beam. In this case, the frequencies of higher modes cannot be gathered from multiplication of the first mode by an integer. In this thesis, only the ***first mode of vibration*** was considered as it has the highest amplitude. Hence, the following discussion refers to harmonics (integer multiples) of the first mode. As we consider driven oscillators (resonators) it is important to distinguish between the exciting frequency Ω and the intrinsic resonance frequency of the resonator ω_n. The second harmonic of the resonator is at $2\omega_n$. However, the frequency of the driving force Ω has to equal $\omega_n/2$ to excite the resonator by its second harmonic component. At the third harmonic at $3\omega_n$ the exciting force must drive with $\omega_n/3$ and so on.

If a voltage is applied between two conductive plates, the electrostatic force between these conductive structures is proportional to the voltage squared, as described in section 2.2 for a parallel plate capacitor. If one part of the capacitor is oscillating, the proportionality between force and applied voltage remains the same but only the capacity is changed:

$$F = \frac{1}{2}\frac{\partial C}{\partial x}V^2 \tag{5.10}$$

Therefore, applying a voltage between a static electrode and the oscillating systems leads to an electrostatic force which is still proportional to the square voltage. Thus, both, the DC part and the AC voltage components at a driving frequency Ω have to be considered:

$$V(t) = V_{DC} + V_{AC}\cos(\Omega t) \tag{5.11}$$

After squaring equation (5.11) according to equation 5.10 there occurs a cosine squared which can be trigonometrically rewritten as follows:

$$\cos^2(\Omega t) = \frac{1}{2}(1 + \cos(2\Omega t)) \tag{5.12}$$

As a result, squaring equation (5.11) and combining it with equation (5.12) gives the proportionality between the applied voltage on the counter electrode and the electrostatic force, acting between counter electrode and resonating electrode

$$F_{elec} \sim V^2(t) = {V_{DC}}^2 + \frac{1}{2}{V_{AC}}^2 + 2V_{DC}V_{AC}cos(\Omega t) + \frac{1}{2}{V_{AC}}^2\cos(2\Omega t) \tag{5.13}$$

Now we have to rationalize that once the excitation frequency Ω is equal to the natural frequency ω_n from equation (5.5), the oscillator goes into resonance. Considering equation (5.13), however, it follows that two resonances are observable: ***1)*** at ω_n which means the natural frequency but ***2)*** also at $\omega_n/2$ due to the last term in equation (5.13), which is equivalent to the second harmonic resonance. Although the second harmonic resonance usually exhibits reduced amplitudes, the arising force is higher due to the squared AC component. Hence, resonance oscillations at $\omega_n/2$ are easily observable and reveal comparable amplitudes in experiments to those at the first harmonic resonance point. This is the foundation for our experiments in this thesis: we always considered the ω_1 /2 resonance and double checked that with the natural resonance at ω_1.

As a short summary, it can be stated that Euler-Bernoulli beam theory provides a sufficient description for the resonance behavior of our quasi-1D-resonators and allows the determination of the natural resonance frequency via equation (5.5). As the resonator is at least weakly conductive, a voltage between the resonator and a nearby counter electrode leads to an electrostatic force proportional to the voltage squared. If an AC field is applied and the frequency of this exciting field is equal to the first mode resonance frequency of the resonator ω_1 or its half value $\omega_1/2$, resonance occurs and the resonator oscillates with highest amplitude in the first mode of vibration.

5.3 Dynamic Response

As discussed in chapter 5.1, the natural frequency $\boldsymbol{f_n}$ of arbitrary geometries can be calculated by the formula

$$f_n = \frac{(\beta_n h)^2}{2\pi h^2} \sqrt{\frac{I}{A} \frac{E}{\rho}} \tag{5.14}$$

with ***h*** as pillar height; ***A*** the cross-sectional area, ***I*** the area moment of inertia about the beam's neutral axis, ***E*** the Young's modulus and ***ρ*** the density. β_n is the modal parameter and has a value of 1,875 for the first mode for cylindrical structures in well agreement with the real pillar geometry. The area moment of inertia ***I*** of cylinders about ***z-axis*** is

$$I_{Z,cyl} = \frac{w^4 \pi}{32} \tag{5.15}$$

with pillar width ***w***. Inserting this equation in equation (5.5) yields

$$f_{res,pillar} = 0.1978 \frac{w}{h^2} \sqrt{\frac{E}{\rho}} \tag{5.16}$$

This equation provides the basis for following discussions. The resonance frequency $\boldsymbol{f_{res}}$ can be found by applying an electromagnetic field to the counter-electrode, sweeping the frequency across a large range and observing the amplitude of the pillar via SEM inspection. The geometrical quantities ***w*** and ***h*** can also be derived by SEM imaging and Young's modulus ***E*** is simulated as described in the following section.

5.4 Adjusting Euler-Bernoulli's Formula to Nano-granular FEBID Deposits

5.4.1 Systematic Deviations

The proportional dependency between f_{res} and w/h^2 (cf. equation (5.17)) has been confirmed by Stermitz et al[22]. The internal composition is contained in the overall Young's modulus ***E*** and mean density ***ρ***. However, considering equation (5.16) it is evident that measuring the resonance frequency only allows access to the ratio E / ρ but not to individual quantities. As Young's modulus is of particular importance, we follow the approach developed in the master thesis of Martin Stermitz[22] who used an electrostatic experiment combined with finite element simulations to determine Young's modulus. Detailed information is given in sections 4.1.2 and 4.1.3. Knowing Young's modulus, it is possible to obtain the mean density ρ of the deposits by rearranging equation (5.16). On the other hand, ρ can also be determined via EDX in certain accuracy ranges as the quantification of carbon in an SEM is a complicated issue. Nevertheless, ***all five quantities Euler-Bernoulli's formula can be fixed by experiments***. Due to the discrepancy from ideal conditions and real FEBID fabricated nano-pillars (inconstant diameter and changing chemical composition with respect to height etc.), systematic deviations from the theoretical formula occur.

In order to account for this convolution, the proportionality constant in equation (5.16), 0.1978, is replaced by a different constant $\boldsymbol{c_{np}}$ (nano-pillar):

$$f_{res,pillar} = c_{np} \frac{w}{h^2} \sqrt{\frac{E}{\rho}} \tag{5.17}$$

This procedure is valid, as all quantities in equation (5.16) are obtained from independent experiments. However, there exists a second constraint: This proportionality factor c_{np} has to be ***constant*** for all pillars fabricated. The reason for that is obvious: If deviations of experimental investigation from the theoretical consideration of Euler-Bernoulli are systematic, they have to be equal for all pillars. Changes in geometry (w, h) or internal structure (E, ρ) ***must under no circumstances*** be reflected in this constant c_{np}. To address this issue extensive pre-testing was performed as discussed in the next main chapter 6.

5.4.2 Nano-Granular Structure

Another important discrepancy from theory is implied by the ***nano-granular structure*** of the deposits. In more detail, FEBID materials used in this thesis consist of a unique metal-matrix-structure by means of 2-3 nm Pt crystals which are spatial homogenously embedded in a disordered carbon matrix as discussed in section 3.1.4. As a result, the mechanical properties of the resonators, i.e. Young's modulus, differ from those expected for a material composed homogeneously by Pt and C. Previous work revealed that, in case of as-deposited nano-structures the mechanical properties are mainly determined by the carbon matrix. TEM investigations[22] and simulations[45] revealed similarities of this matrix to loosely linked fragments for both, structure and properties.
However, it turned out that the properties of as-deposited pillars are highly changeable via post-growth e-beam treatment[,33,34]. By that, graphitization of the carbon matrix takes place and a glass-like carbon state is established[22]. Mechanical properties are naturally affected by this change and thereby Young's modulus E as discussed in detail in chapter 6.8. Hence, Young's modulus is tunable over a wide range and can even exceed values for glassy carbon. In this case one has to take the Pt nano-crystals in account. Hence, we can compare the value for glassy carbon E_{gC} with actual Young's modulus obtained from experiments and simulations, E_{sim}. The deviation from glassy carbon behavior is caused by the nano-granular metal-matrix-structure which is accounted for by the nano-granular factor c_{ng}:

$$E_{sim} = E_{gC} * c_{ng} \tag{5.18}$$

This expression connects real Young's modulus of the resonator E_{sim} with the modulus which can be expected for a glassy carbon material E_{gC}. Hence, equation (5.16) has to be expanded by another expression concerning the ratio E/ρ:

$$f_{res,pillar} = c_{np} \frac{w}{h^2} \sqrt{\frac{E_{hom} * c_{ng}}{\rho}} \tag{5.19}$$

The expression above can be considered as core equation for this thesis which will be used throughout the study.

5.5 Summary

The high aspect ratios of quasi-1D-resonators allow the application of Euler-Bernoulli beam theory. This model predicts the intrinsic resonance frequency of a perfect cylinder with respect to its dimensions, Young's modulus and density as given in equation (5.16).

For resonators fabricated via FEBID deviations from this ideal cylindrical shape occur, especially at the bottom and topmost areas where the diameter is significantly increased. However, this broadening is caused by the deposition process and similar for all fabricated resonators. As a result, it represents a systematic deviation, which can be accounted for by a proportionality factor $\boldsymbol{c_{np}}$ (equation (5.17)) which is constant for all ***n***ano-***p***illars fabricated within the framework of this thesis. As all physical parameters in this equation are determined by different and measuring procedures independent from each other, a constancy of this factor $\boldsymbol{c_{np}}$ simultaneously proves the validity of all basic proportionalities in Euler-Bernoulli's idealized formula (equation (5.14)) for real FEBID nano-pillars.

An important part within this resonance concept is the unique carbon-metal nano-granular structure which enables higher amplitudes at oscillation as the Pt / C ratio would suggest for a homogenous material.[22] In order to consider this deviation, we assume Young's modulus for a one phase carbon material in similar state E_{gC} and compare it with real Young's modulus gathered from experiments and finite elements simulations, referred to as E_{sim}. By that, equation (5.17) gets expanded by another factor $\boldsymbol{c_{ng}}$which takes the ***nano-g***ranular structure of the quasi-1D-resonators into account.

6 Geometrical, Chemical and Mechanical Characterization

Basing on the proof-of-concept study for electrically excited resonance by Martin Stermitz in 2014[22], this thesis provides a deeper insight in geometrical, chemical and mechanical properties of quasi-1D resonators. In more detail, Stermitz et al. revealed that the unique internal metal-matrix nano-structure provides both, electrical conductivity and mechanical flexibility. Moreover, it is the key for the mechanical tunability (and therefore for the tunability of the resonance frequency) of nano-pillars. As the main idea is the development of a gas sensing concept discussed in chapter 2.3, a fine control of material properties is indispensable for a successful application as electronic device. FEBID processing has been demonstrated to be versatile but also very sensitive with respect to its preparation properties. In particular, chemical composition and structural details can considerably change relying on the so called working regime which describes the local ratio between available precursor molecules and potentially dissociating electron species (cf. chapter 1.7). Therefore, a detailed investigation of the material properties regarding deposition parameters is needed for analyses from a fundamental point of view followed by studying the consequences on the resonance behavior which is the content of this chapter.

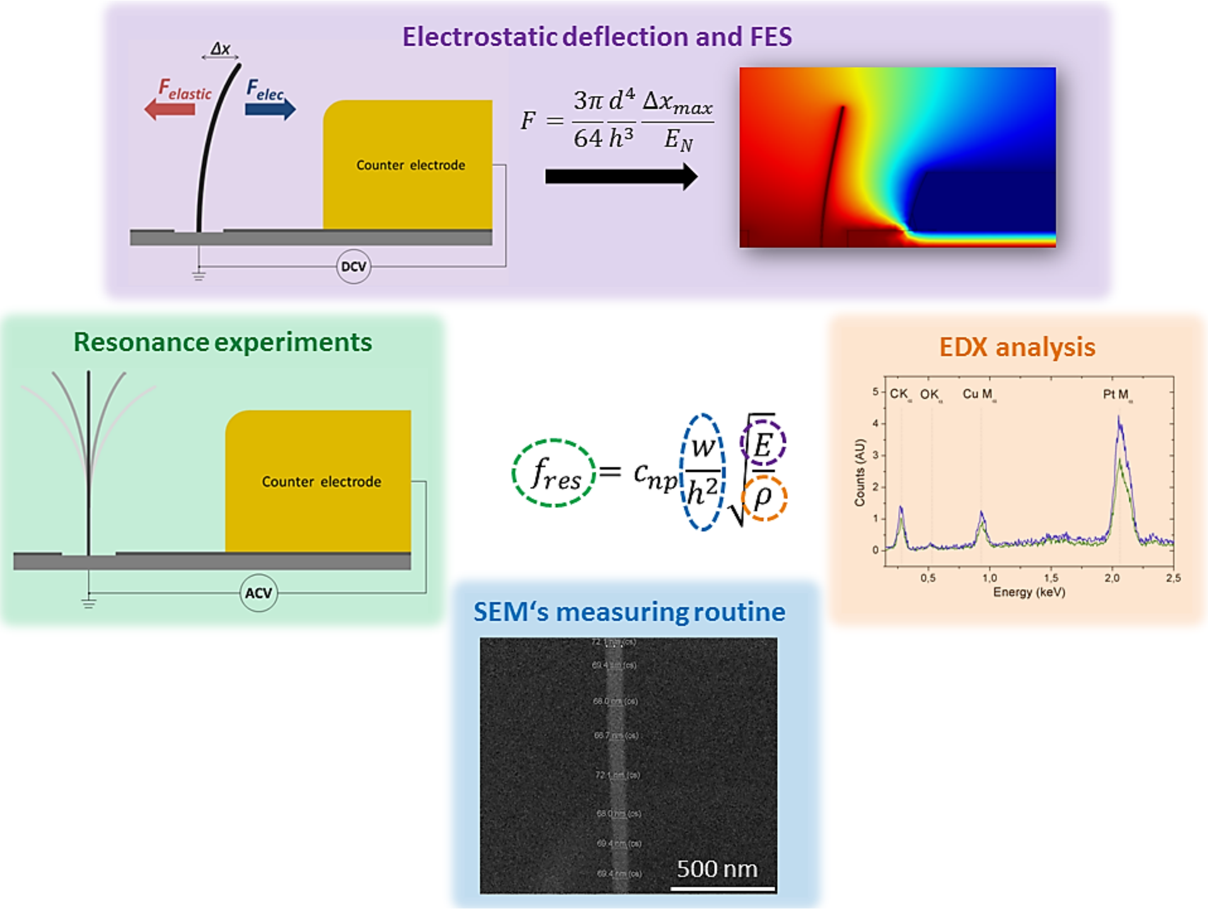

Figure 6-1: Experimental determination of basic parameters in the adapted equation of Euler-Bernoulli (equation (5.17)).The individual parts of the central equation are accessed by different experiments following the line and background color in the equation and the schemes, respectively.

Figure 6-1 demonstrates the experimental sequence for finding individual quantities in equation (5.17). First thing to study was the relation between process parameters and final geometries. The latter is closely related to the growth rate which in turn bases on the precursor working regime as described in more detail in section 1.7. Hence, in the first sub-chapter the influence of primary electron energies and beam currents on the geometry of quasi-1D-nano--pillars is investigated in detail and connected to fundamental regime processes. The second sub-chapter then links these findings with the resonance behavior revealing strong variations in a non-linear fashion. Next, e-beam based post-growth procedures are analyzed demonstrating the fine tunability of resonance frequencies by almost an order of magnitude. To access mechanical material properties in detail, static deflection experiments and compositional characterization were performed to decouple Young's modulus and the resonators' mean density. The outcomes of these investigations are discussed in chapter 6.4 and chapter 6.3, respectively. The results are then combined with finite element simulations (cf. chapter 6.5) providing mechanical quantities in correlation with resonance frequencies at varying process parameters. This comprehensive experimental insight finally allows expansion of the mathematical model (chapter 5) by the nano-granular nature of the materials. As shown in chapter 5.4.2, the nano-granularities of FEBID materials in conjunction with the small structures' dimensions are the key elements of the resonator's tunability. Apart from this main finding, the respective chapter also provides guidelines how the quasi-1D resonators have to be fabricated for a predictable resonance behavior and in a reproducible way for final gas sensing applications which are discussed in the following main chapter.

6.1 Geometries and Volume Growth Rates

As described in the 3.1.4 electron limited regime (**ELR**) conditions are required as foundation for strong effects of post-growth treatment and as gateway for the mechanical tunability. This relies on the fact that these conditions incorporate a high number of incompletely dissociated precursor molecules on purpose. Such molecules can then be fully dissociated via post-growth e-beam exposure leading to slightly increased Pt grains due to released Pt atoms while the center-to-center distances of Pt grains remain the same. The relevant consequences for this thesis are changed mechanical properties as the distance between neighbored grains is reduced which influences bending experiments. The requirement of ELR is the main reason why lowest beam currents have been used for following investigations as summarized in Table 6-1. The resulting slightly different beam currents at different primary energies are technically prescribed and lead to different behavior as will be shown in detail later. In this chapter we focus on reproducibility aspects of quasi-1D nano-pillars concerning their heights and widths.

Table 6-1: Experimental parameters of deposited pillars for VGR results

Pillar set … Identification of the pillar; the first number corresponds to a particular date of fabrication, the second to the PE energy
U_{PE} … Acceleration voltage of primary electrons in kV
I_{PE} … Current of electron beam in pA
TET … Total exposure time
h … Height of the deposited pillar in µm
w … Mean width of the deposited pillar in nm

Pillar set	***U_{PE} / kV***	***I_{PE} / pA***	***TET / s***	***h / µm***	***w / nm***
1 - 5	5	5	300	5.03	74.6
2 - 5			280	5.02	75.0
3 - 5			280	5.07	80.0
4 - 5			280	5.10	76.9
1 - 10	10	7.5	400	4.97	74.8
3 - 10			400	5.07	65.9
1 - 20	20	13	500	5.10	75.5
3 - 20			500	4.83	66.7
1 - 30	30	21	450	4.18	66.1
3 - 30			550	4.85	72.9

The main intention was to extract the dependency of pillar widths and heights on primary electron energies and corresponding minimal beam currents. Therefore, single pillars with continuous point exposure have been deposited on Si substrates close to Au counter electrodes according to the procedure given in chapter 4.1.1 including the complex and thorough focusing and stigmator setting strategy described in chapter 4.1.1.2.

Table 6-1 summarizes primary energies, beam currents, total exposure times (**TET**) and the resulting pillar heights and widths. Figure 6-2 shows the vertical growth rate (**zGR**) and VGR in dependency on the primary energy on the left as well as the right, respectively. For the calculation of the volume, the pillars were approximated as ideal cylinders. The used widths are the arithmetic mean of multiple data measured at equidistant steps along the main axis of the pillar. Both plots are normalized to lowest growth rate values for highest primary energies to extract an energy dependent efficiency factor. As expected, both growth rates decrease for increasing primary energies due to less appropriate dissociation cross-sections and decreasing areal emission of surface electrons as described in chapter 1.4. However, although the overall tendencies are always the same, a comparable large splitting occurs related to different sets of the experiments (compare with the legend). This becomes particularly evident for the VGRs on the right hand side. Figure 6-3 shows a height (blue squares, left axes) and diameter (red triangles, right axes) plot for 5 keV pillars in dependency on the date of fabrication. As evident, there is no clear correlation to the date which was initially thought to be responsible as the precursor reservoir is empting.

Nevertheless, the observed diameter variations of up to ± 4 % for equal deposition parameters at 5 keV / 5 pA cannot be neglected. A closer look in context of reproducibility is required.

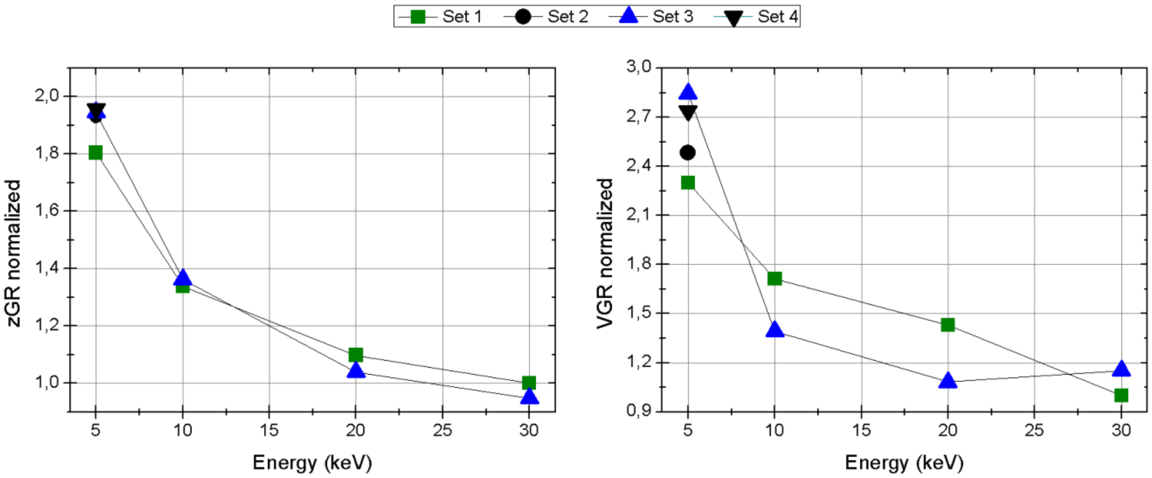

Figure 6-2: The normalized mean growth rate along the main pillar axis (left) and normalized mean volume growth rate of deposited pillars, the product of area cross section and height per deposition time (right). In consensus with a declining cross section for dissociation of precursor molecules and an additional wider spread out of electrons growth rate diminishes nonlinear. While the zGR at a given PE energy slightly varies with respect to different sets the VGR reveals strong variations.

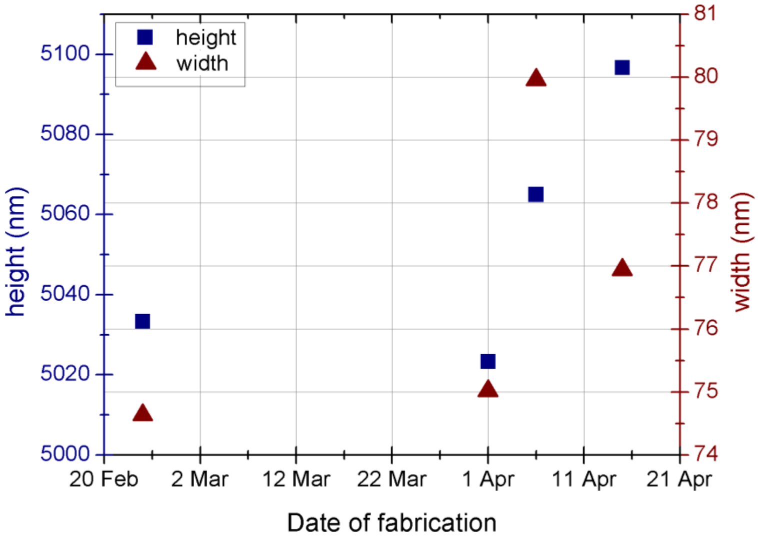

Figure 6-3: Mean heights (blue squares, left scale) and widths of pillars (red triangles, right scale) deposited with 5 keV and 5 pA with respect to the date of fabrication. The plot does not reveal any correspondence between the variations in pillars' geometries and the dates they were fabricated.

Assuming a widely constant gas flux due to identical technical setup and negligible effects of the precursor reservoir, two main parameters could be responsible for these variations:

i) *Focus point*
ii) *Axial astigmatism*

First, we consider the width variations which lie between 74 and 80 nm (< ± 4 %) for 5 keV as summarized in Figure 6-3. Following equation (5.16) for e.g. a typical 400 kHz resonator this means a predictability and reproducibility of < ± 4 % relative which represents an acceptable accuracy. Same holds for the pillar heights at 5 keV for which a Δh of ± 80 nm has been found (< ± 1 %) also being equivalent to a good accuracy of the resonance frequency of < ± 2 %. However, as shown by Stermitz et al.[22], similar height variations in absolute values can be found for smaller heights of 3 - 4 µm, too. Hence, height variations seem to originate from early growth stages below the critical limit of about 2 µm (cf. chapter 1.7).[14] This stems from the fact that in terms of precursor replenishment the SDR-S component still has a strong influence on short pillars and changes the vertical growth mode depending on beam-diameter and -shape. Once the critical length of about 2 µm is exceeded, the working regime becomes widely stable predominantly governed by GFR and SDR-D components and reaches a constant vertical growth mode. Therefore, the relative height variation and by that the resonance frequency becomes height dependent while the relative width variation is independent from the pillar height.

Although an overall deviation of less than 5 % seems to be acceptable we take a closer look on the origins of these variations as it reveals surprising results. Considering test point deposition as described in chapter 4.1.1.2, i.e. single spot deposits with continuous exposure for approximately 5 s, there occur significant differences in the area cross-section of these spots even for equal deposition parameters. As described in chapter 4.1.1.2, experiments revealed that the focusing procedure could be performed precisely enough that it had little influence on the test spot’s profile. However, smallest variations in stigmator settings highly affected the diameters of test spots and led to a change in diameter of 2 - 5 nm around the minimal value given by ideal stigmator settings. By that, deviations in pillars’ diameters at a scope of a few % could not be avoided even by most thoroughly performed stigmator adjustment. This explains the occurring width variations even for equal deposition parameters.

Furthermore, we want to expand these considerations and compare test points deposited at different PE energies / beam currents. There occured two remarkable differences depending on the deposition parameters: The test point’s size and shape. Smallest diameters for pillars with heights of ca. 5 µm can be found for 10 keV, 20 keV and 30 keV (cf. Table 6-1). This qualitative behavior is also evident for test points with minimal heights. Naturally, widths of test points are significantly smaller than those for high pillars of several µm in height, mainly because of changing means of precursor replenishment above 2 µm and the increasing involvement of FSE for growing pillars[14] (cf chapter 1.7). However, the difference between 5 keV test points (~ 60 nm) to other PE energies (~ 54 nm) is in a similar range as for 5 µm pillars (~ 76 and ~ 70 nm, respectively). In addition, test spots deposited with different PE energies / current vary also in their cross sectional shape. 5 keV test points reveal a significant discrepancy from a circular profile and 10 keV and 20 keV test points have even more resembles to a triangular shape (Figure 6-4). Only point structures deposited with 30 keV (left) exhibit an almost circular cross section.

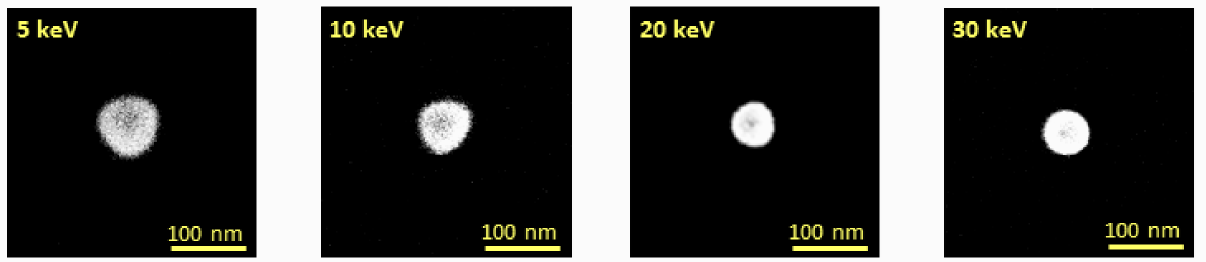

Figure 6-4: Test point deposition (pillars with a total exposure time of 5 s) for 5, 10, 20 and 30 keV (from left to right) and lowest possible currents. The cross sections significantly differ in their particular shape.

So far, it can be stated that there occur minimal variations in diameter and height for equal fabrication procedures up to ± 4 % and ± 1 %, respectively. Although the influence of these variations on the resonance frequency is acceptable for the reproducible fabrication of resonators, the origins of differing heights and widths should be mentioned. Depending mainly on stigmator settings, pillars exhibit slightly varying cross sections. This cannot be avoided since the diameter is extremely sensitive to stigmator settings. Height variations are a consequence of these variations of the cross sectional size and stem from early growth stages. The SDR-s component dominating for deposits < 2 µm depends on the deposits' size and shape and changes the vertical growth rate. As a result, for higher pillars, i.e. higher than 2 µm, the relative height variation diminishes with increasing height. As an extreme aspect ratio is intended for quasi-1D nano-resonators, the relative variation of heights at equal deposition parameter tends to be very small.

The fact, that other unstable experimental parameters such as precursor gas flux have a smaller influence than the beam settings, which cause significant changes in width, leads to the consideration that pillars should be categorized according to their diameter, i.e. to their quality of beam setting alignment. This means that it is beneficially to compare pillars with minimal, mean and maximal diameter. Figure 6-5 reveals the astounding results of this rearrangement. In the left plot, one can see the mean volume growth rate of two complete sets containing one pillar per PE energy. All pillars of one set are fabricated ***successively***. The two VGR trends with respect to PE energy seem to disagree completely (Figure 6-5, left). On the right hand side, the pillars were categorized ***per diameter***. This means that those pillars

with smallest (cyan) and highest (red) diameter at a specific PE energy respectively were joined to one set. Now, VGR trends are similar, only shifted slightly upwards for thicker pillars, which is in agreement to the fact that the zGR shows less variation than the VGR (cf. above Figure 6-2). Consequently, the growth of thicker pillars is not at the expense of reduced vertical growth but mainly leads to increased total VGR compared to thinner pillars. All exponential fits were performed with $y(x) = y_0 + Ae^{-x/t}$.
Hence, geometry related results ought to be categorized by their diameter, i.e. the beam setting alignment. Especially comparing thinnest pillars and therefore those deposited with best beam settings lead to good results (Figure 6-5, right, cyan). In terms of reproducibility we can conclude that apart from technical limitations pillars grow in a very reproducible way, however, with slightly different diameters. The latter aspect is of acceptable influence as for sensing applications the initial resonance frequency functions as basis in order to observe relative shifts without absolute demand for a fixed value.

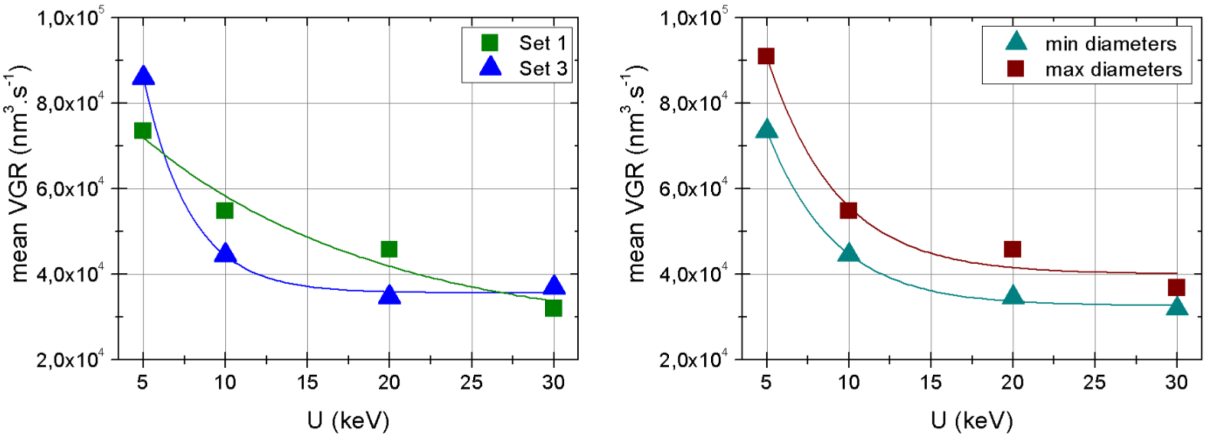

Figure 6-5: Mean VGR for pillars deposited in successive deposition processes (left) reveals no identifiable trend. Joining pillars with minimal (cyan) and maximal (red) diameter in the right plot follow the expected exponential decay of the VGR for increasing PE energies.

Apart from the acceleration voltage there is another electron beam parameter that strongly influences deposition: The beam current. In order to assess this influence, three pillars were deposited at 30 keV for an equal TET (550 s) but with different beam currents. The results are presented in Table 6-3 and Figure 6-6. For pillars discussed so far, the lowest available currents were always used at specific PE energies. Unfortunately, at the used FIB Nova 200, the beam current is not arbitrary tunable but provides discrete levels. For investigation of the beam current influence, the three lowest possible currents at 30 keV (21 pA, 44 pA and 150 pA) were used for deposition. Detailed experimental parameters and geometric dimensions can be derived from Table 6-2.

Table 6-2: Experimental parameters of pillars deposited with 30 keV and varying currents

Pillar set … Identification of the pillar; the first number corresponds to a particular date of fabrication, the latter to PE energy and beam current
U_{PE} … Acceleration voltage of primary electrons in kV
I_{PE} … Current of electron beam in pA
TET … Total exposure time
h … Height of the deposited pillar in µm
w … Mean width of the deposited pillar in nm

Pillar set	**U_{PE} / kV**	**I_{PE} / pA**	**TET / s**	**h / µm**	**w / nm**
5 – 30 – 21	30	21	550	6.31	81
5 – 30 – 44	30	44	550	6.04	89
5 – 30 – 150	30	150	550	5.46	97

First of all, the total height decreases with increasing currents (cyan squares in Figure 6-6, left). Simultaneously, significant broadening (red rectangles) and aberrancy of ideal pillar shape at the base occurs. According to that, using higher beam currents for nano-pillar deposition leads to a reduced vertical growth rate (Figure 6-6, right), although the overall VGR increases. As the VGR does not saturate the condition for a general regime shift from ELR to MTR is not fulfilled. However, the reason again can be found in precursor replenishment related issues. As discussed in detail in chapter 1.7, diffusion of precursor molecules from the substrate (SDR-S) quickly diminishes for growing quasi-1D nano-pillars and precursor molecules can only be replenished by diffusion from surrounding areas of the deposit (SDR-D) or direct absorption from gas flux. Using higher currents leads to a higher electron density. Thus, depletion at topmost areas, which can hardly be reached by substrate related diffusion, occurs. As a result, fewer electrons are involved in dissociation processes. Instead, they can get scattered by the deposit (FSE) and thereby end up in areas close to the base. There FSE and generated SE_{III} dissociate precursor molecules and therefore prohibit diffusion of these precursor molecules to higher areas of the growing structures. Hence, the zGR decreases and the pillar gets broadened. For this reason, instead of a general regime shift from ELR to MTR conditions at higher beam currents depletion occurs only at topmost areas and leads to broadening at the base of the deposit.

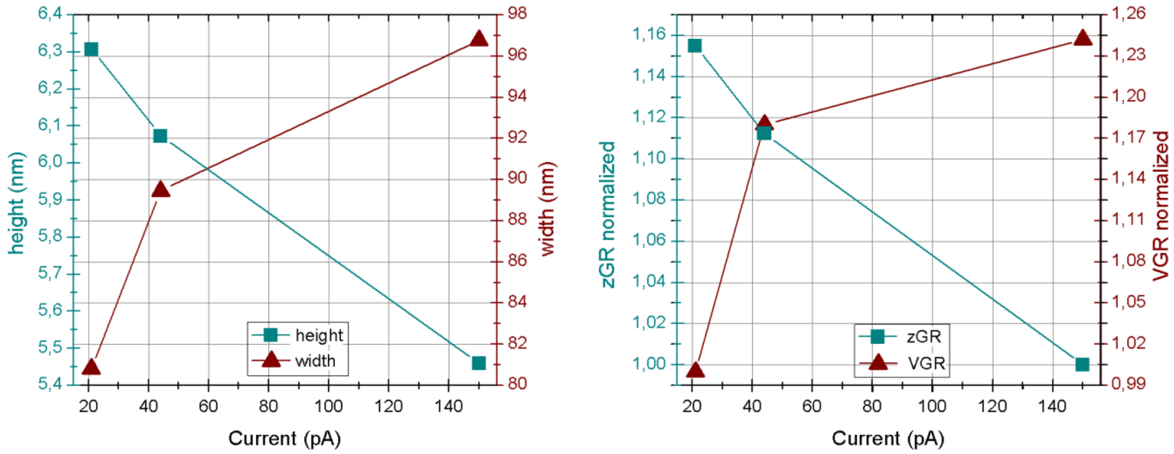

Figure 6-6: Left: Evolution of pillar's heights (cyan squares) and widths (red triangles) for increasing beam currents at 30 keV. The right plot reveals the according zGR (cyan squares) and VGR (red triangles). Whereas the VGR increases for higher currents (more electrons) the zGR gets reduced.

Summing up the results gathered from experiments concerning geometric issues and related growth rates: At this point we can state that there are variations of ± 3 nm (± 4 %) in diameter and up to 200 nm in height (20 keV / 13 pA, cf. Table 6-1) at comparable experimental parameters, i.e. same PE energies and currents. These variations are mainly determined by varying stigmator settings which cannot be avoided completely but only minimized via thorough and careful alignment. Nevertheless, the growth rates for equal geometrical dimensions are very similar which testifies to good reproducibility. In general, low-keV deposits provide higher growth rates as expected. However, they reveal the strongest deviation from cylinders in their cross sectional profiles. In contrast, 30 keV pillars exhibit smallest diameters and almost circular cross sections. The use of higher currents significantly broadens the structures. This is highly disadvantageous concerning our gas sensing concept as the minimal diameters of quasi-1D-resonators ought to provide extreme sensitivity. From this fact, there could be drawn two important conclusions:

1. ***It is strongly recommended to use smallest currents and high PE energies.***
2. ***As far as possible, geometric variables ought to be cancelled out of further experimental results, e.g. resonance considerations etc.***

6.2 Resonance Experiments

6.2.1 Qualitative Analysis

A comprehensive characterization of the resonance behavior is inevitable for following gas sensing applications of quasi-1D resonator. As already mentioned in section 2.2, the resonance concept was proven by Martin Stermitz[22], who managed to put 5 keV pillars on resonance. The first investigations concerning geometric issues revealed significant differences in pillars' outer dimensions with respect to deposition parameters (cf. chapter 6.1). As a second step, it is important to examine the effect of these geometrical deviations on the resonance behavior, i.e. quantity and quality of the resonance peak.

In order to determine the intrinsic resonance frequencies of the quasi-1D-structures an AC voltage was applied at the counter electrode. The detailed experimental setup is described in chapter 4.1.2.2. Figure 6-7 illustrates the measuring technique (top). The bright structure on the left edge represents the counter electrode, which an ACV was applied to. An insulating SiO_2 layer covers the specimen below the Au metal layer (Figure 4-2). The quasi-1D-resonator had to be connected to the Si substrate, which works as complementary electrode. For that, the insulating layer was sputtered off across a squared area and the resonator was deposited on the Si substrate 2,5 µm apart from the counter electrode.

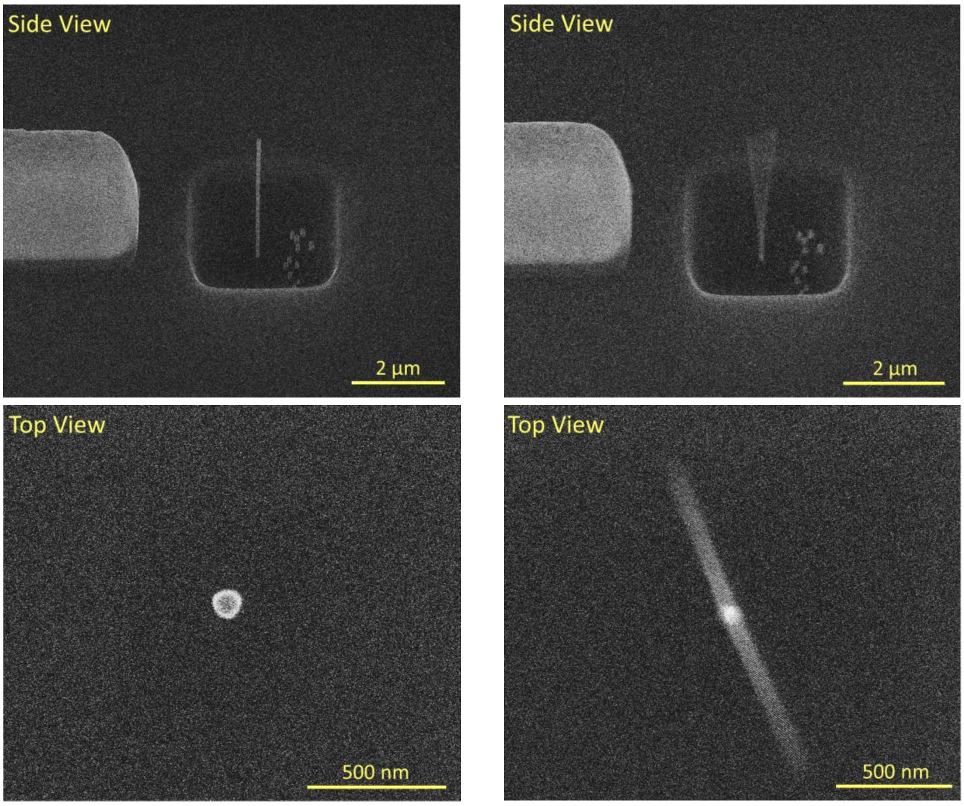

Figure 6-7: Side- (top) and top-view (bottom) of a 5 keV pillar off (left) and on resonance (right). Please note the different scales in the legends at the bottom of each SEM frame. The image noise originates from the applied ACV field.

Simultaneously, Figure 6-7 impressively demonstrates the extreme aspect ratios of the free standing quasi-1D deposits. What is more, the structures clearly reveal resonating behavior around the mechanical resonance frequency. The occurring deflection is obvious in top view (bottom) as well as in side view (bottom), comparing left (out of resonance) with right images (resonance frequency at maximal amplitude).

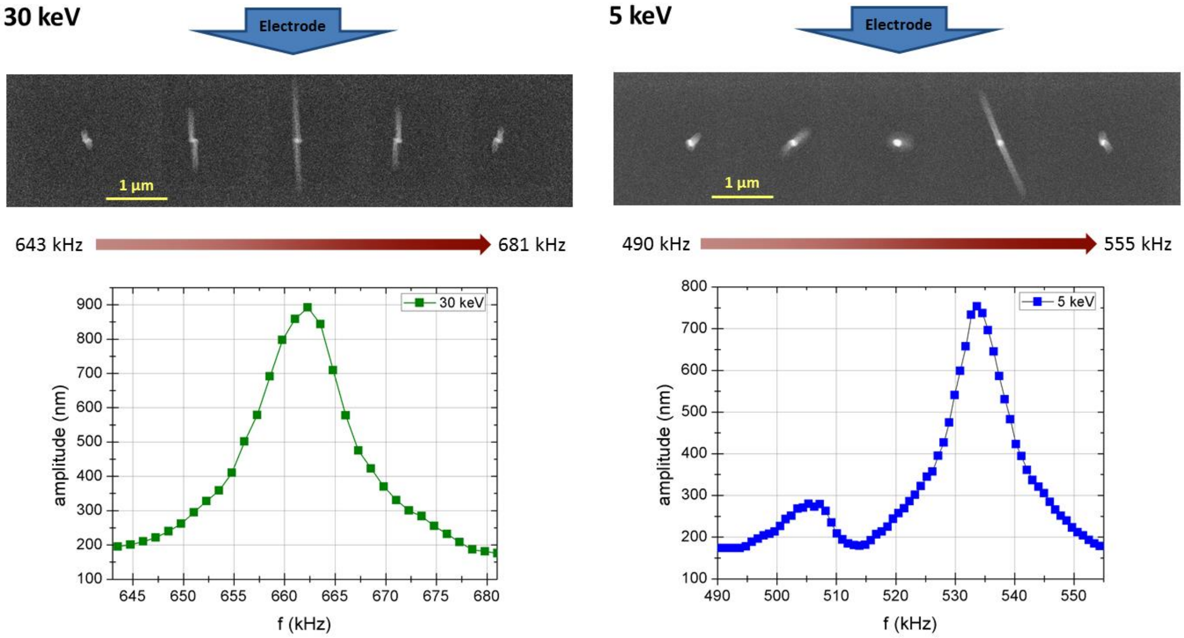

Figure 6-8: Top view SEM image (left) of typical resonance behavior and corresponding peak (bottom) of a 5 keV pillar (left) and a 30 keV pillar (right). Due to stigmator settings, 5 keV pillars use to have cross sectional profiles differing from a circle and exhibit two consecutive resonance frequencies. Pillars deposited with 30 keV are almost perfect cylinders and show resonance at one single frequency.

Characteristic oscillating behavior around the intrinsic resonance frequency reveals symmetric peaks (Figure 6-8): The amplitude rises with increasing frequency of the AC voltage up to a certain point, the resonance frequency, and diminishes with further ascending frequency of the alternating electric field. First thing to notice when comparing resonance of pillars deposited with 5 keV to 30 keV pillars is the direction of the occurring oscillation. A 30 keV pillar deflects almost exclusively along one axis towards the counter electrode which is in line with expectations for a perfectly cylindrical resonator excited from one well defined direction. Only a minimal translation along the transverse axis can be observed leading to slightly displaced amplitudes in opposite directions.

In contrast, the oscillating behavior of 5 keV pillars exhibits two main differences:

i) *There occur two neighboring resonance peaks.*
ii) *The angles between their directions of oscillation ranges from 100° to 120°.*

Similar resonance behavior is found for 10 keV and 20 keV, too. While one resonance peak is significantly smaller at 5 keV, pillars deposited at primary energies of 10 keV and 20 keV reveal two almost identical peaks.

In order to understand the reasons for this surprising behavior we have to return to the outcomes of the previous chapter. Test spot investigations revealed significant deviations from a circular cross section for lower keV which diminished for test spots deposited with 30 keV (see Figure 6-4). This geometric difference is also reflected in the resonance deflection. An ideally shaped circle is ***isotropic***. Hence, bending a cylindrical pillar requires equal efforts independent of the direction and the pillar is deflected towards the attractive force originating from the counter electrode. In addition, resonance occurs at one fixed resonance frequency. Similarly, this can be observed for 30 keV resonators.

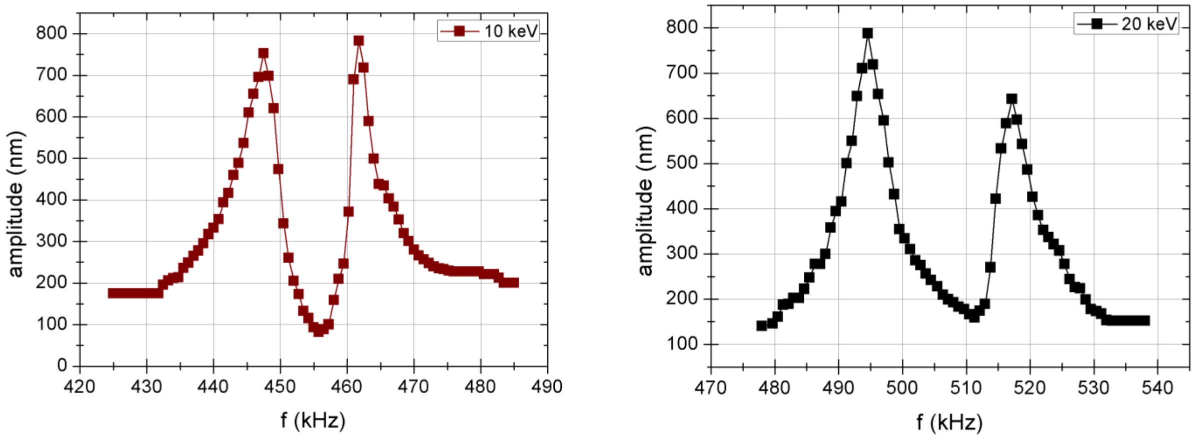

Figure 6-9: Amplitude in vicinity of the point of resonance. Similar to 5 keV there occur two resonance peaks but in contrast, they exhibit almost equal heights.

In contrast, all other pillars, i.e. those deposited with 5, 10, and 20 keV ***always*** revealed two clearly separated points of resonance. Considering test spots (Figure 6-4), there is an obvious aberrancy from a circle for these PE energies. The test spots' shape resembles the superposition of a circle and a triangle. Thus, the resulting geometry is similar to a triangle with rounded corners. By that, ***preferred directions*** occur since bending is carried out with less effort perpendicular to the sides of the quasi-triangle. As the force is applied from one side, there will appear an oscillation along two preferred directions. Moreover, the pillars' cross section is obviously neither an equilateral triangle nor a perfect circle. Hence, oscillation in different directions will appear at different frequencies. Figure 6-10 demonstrates this fact revealing the spatial resonance pattern of a certain set of pillars. Two resonance frequencies occur for all pillars except for those deposited with 30 keV, i.e. all pillars possessing this more or less triangular shaped cross section (cf. also corresponding resonance peaks in Figure 6-8 and

Figure 6-9).

Taking a closer look at the direction of oscillation, one can see that the directions differ from pillar to pillar, even though angles between both oscillations of one particular pillar are approximately similar (100° - 120°). Stermitz investigated these angles between oscillation and exciting electrode for 5 keV pillars and spoke about a random distribution[22]. The findings above display the reason for that behavior: As the electron beam is rotated by electron lenses the orientation of the quasi-triangle varies and by that the direction of oscillation varies as well. Naturally, the amplitude also varies with the oscillating direction as it corresponds to the angle towards the applied force. For the 10 keV and 20 keV pillar in Figure 6-10, this angle is between 45° and 60° for both oscillations. As a result, the amplitudes are similar for both resonances. At 5 keV the amplitude of one oscillation is significantly larger because of a greater spatial component parallel to the applied force.

Hence, it can be stated that the appearance of two resonance frequencies corresponds to slightly triangular shaped deviations from a circular cross section for 5, 10, and 20 keV even for perfectly adjusted stigmator settings.

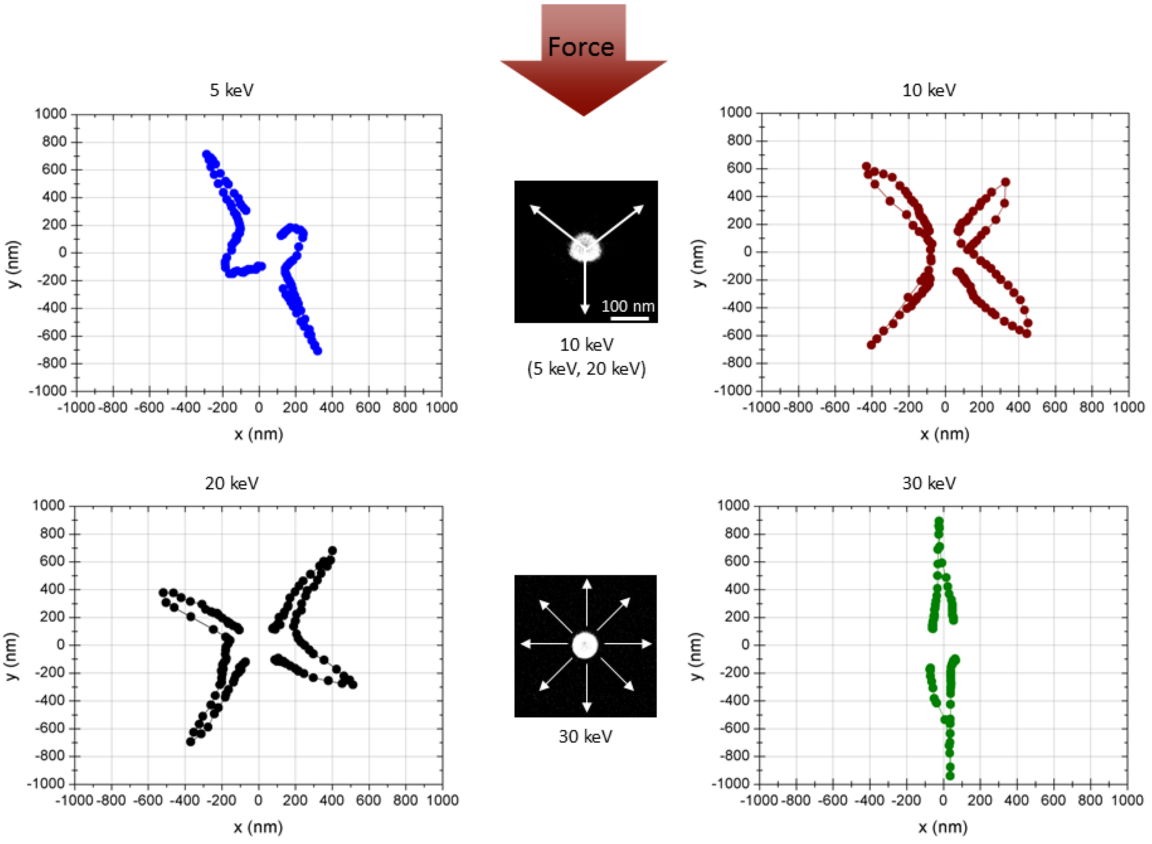

Figure 6-10: Characteristic resonance pattern for pillars deposited with different PE energies and lowest currents. Even for adjusted stigmator settings, 5, 10, and 20 keV pillars revealed a triangular cross section leading to two oscillations in different directions. An almost circular cross section for 30 keV pillars resulted in a single resonance peak and oscillation towards the counter electrode.

However, the user defined settings of the astigmatism corrector naturally have the power to change cross section dimensions along specified axes. As mentioned before it is possible to alter the ratio between horizontal and vertical scale by the y-stigmator settings and the ratio between diagonal axes via the x-stigmator. Stermitz et al.[22] revealed for 5 keV pillars that the distance in kHz between successive points of resonance increases with rising y-astigmatism, i.e. with stronger anisotropy of horizontal and vertical axis leading to an elliptic shape. What is more, he was able to suppress the appearance of one oscillation at strongly astigmatic pillars. This influence of intended astigmatism on the resonance behavior could also be confirmed empirically in the work of this thesis. In addition, a second resonance could be induced even for 30 keV pillars at strongly misaligned stigmator settings. Taking a closer look at the SEM images of the 30 keV resonance oscillation in Figure 6-8 they also reveal a slight transverse shift reversing at the resonance frequency. This stems from a second point of resonance arising from a minimal anisotropy between vertical and horizontal axis. The angle between these oscillations is exactly 90° which strongly suggests that the origin can be found in stigmator settings. As these deviations are very small, the resonance frequencies of vertical and horizontal oscillation rather coincide and the transversal shift reverses simultaneously with maximum vertical amplitude. As one oscillation is parallel to the counter electrode its amplitude naturally dominates.

At the end of this complex part, we need to summarize the main findings: Aberrancies from a perfectly circular cross section of quasi-.1D-resonators lead to the rise of preferred directions and more points of resonance. On the one hand, there appear ***intrinsic*** and triangular shaped deviations for all pillars except those deposited with 30 keV. These influences cannot be compensated by user controlled stigmator settings. By that, all these pillars exhibit two points of resonance at excitation from a single, well defined direction. On the other hand, ***elliptic*** deviations can arise from user adjusted stigmator settings which also affect resonance oscillations. For strong astigmatic pillars, i.e. dominating elliptic influences, an oscillation arising from intrinsic cross sectional deviations can be suppressed or even a new oscillation can be induced. Hence, the appearing resonance behavior is the result of superposed elliptic (stigmator settings) and triangular (intrinsic) geometrical deviations and implies at least two points of resonances at different frequencies. An exception is found for 30 keV pillars with perfectly aligned stigmator settings. Thus, generally the resonance behavior is the superposition of two oscillations (similar to Lissajous curves). The distance in kHz between resonance frequencies of the particular oscillation increases with stronger deviation from a circle, i.e. with stronger anisotropy.

Although the influence of stigmator settings is obvious and misaligned settings can even be taken as an advantage, we followed the strategy of best aligned stigmator settings to gain pillars with similar dimensions along all horizontal directions. This strongly facilitates and enhances the reliability of width measurements which are inevitable for the geometrical characterization of resonators (cf. chapter 6.1). Hence, deposited 30 keV pillars exhibit one oscillation towards the counter electrode while pillars deposited with other PE energies revealed two oscillations at different frequencies. For further analysis, the arithmetic mean of these two frequencies was used as resonance frequency of the particular resonator. These results strongly suggest using 30 keV pillars for gas sensing applications.

Please note, that the considerations above also imply some simplifications or assumptions, especially an identical cross section from the basis to the very top of the structure. In reality, pillars revealed much more complex oscillating behavior such as twisting, rotating, as well as the absence of any resonance without any visible geometrical reason. Especially pillars with small influences of both elliptical and triangular variations where none form dominates showed very complex resonance oscillations. However, a detailed and even more thorough analysis is firstly beyond the scope of this thesis and secondly extremely technically challenging due to the enormous requirements on lateral and temporal imaging resolution. Nevertheless, we were able to build quasi-1D resonators which reliably oscillated in accordance to the findings from above with the focusing and stigmator setting strategy from chapter 4.1.1.2.

6.2.2 Oscillation Comparison

In order to receive a first overview about the quantitative resonance behavior with respect to varying deposition parameters, we plot the resonance frequency gathered from electrodynamic experiments as described in chapter 4.1.2.2 against the PE energy. Unfortunately, these results provide no indication for a certain trend (Figure 6-11, left). Considering proportionalities in Euler-Bernoulli's formula, the resonance frequency strongly depends on geometry with $f \sim w/h^2$, which has been already proven experimentally by Stermitz et al.[22]. In turn, chapter 6.1 revealed that geometric dimensions depend on beam settings and therefore include some randomness which is highly undesired but cannot be avoided. Hence, it is of great importance to exclude geometrical influences from experimental results. This can be achieved by weighting the resonance frequency with the ***inverse of the geometrical factor, viz. $\boldsymbol{h^2/w}$***. This inconspicuous mathematical operation provides impressive results as shown in in Figure 6-11 (right). It is clearly visible that resonance frequencies are higher at both ends, i.e. for 5 keV pillars and 30 keV pillars if they are released from geometrical influences.

An unpleasant fact can also be derived from Figure 6-11. In the right plot groups of 30 keV pillars were emphasized by red circles. These circles refer to the corresponding pillar set, differing in the date of deposition. While geometric dimensions, i.e. diameter and height, did not reveal any clear correlation to the date of fabrication (cf. Figure 6-3) since influences arising from differing beam settings dominated, the resonance frequency adjusted for geometries exhibits a marked trend. Figure 6-11 clearly shows that pillars alter in their properties with respect to their date of deposition. The reasons are slight differences in the GIS system, the filling level of the precursor gas etc. All these parameters influence the sensitive process of a single spot deposition. From this point of view, it is obvious that only pillars deposited on the same or nearby dates, i.e. pillars corresponding to the same set, are comparable. Hence, in further discussion we want to focus on pillars which were fabricated within one continuous experiment.

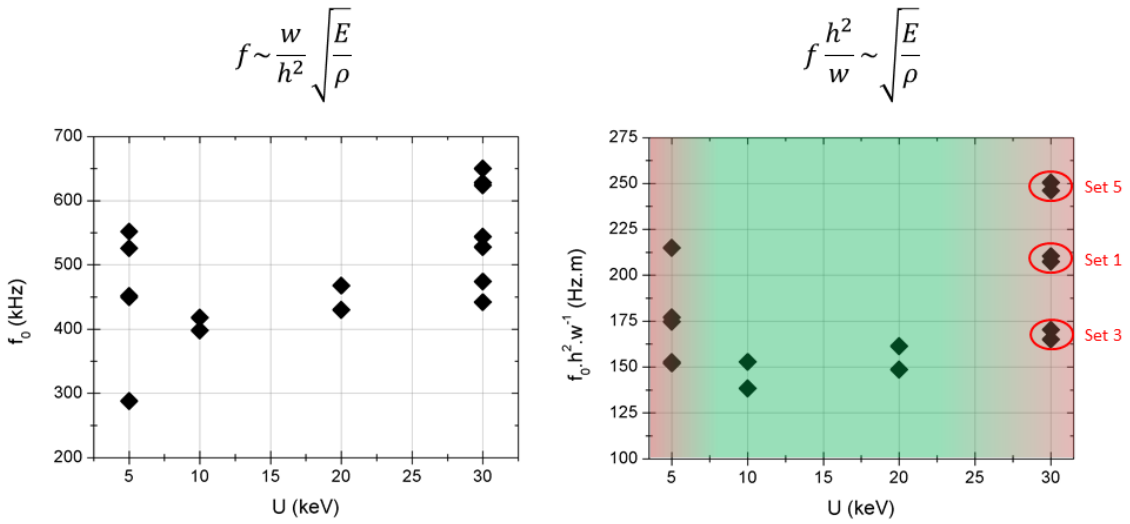

Figure 6-11: Comparison of pure resonance frequency (left) and those, weighted with w/h^2 *to cancel out geometric effects (right). The red circles indicate associating pillars at their date of deposition. Highest frequency adjusted for geometrical influences are provided by both lowest and highest PE energies (red background).*

Figure 6-12 again shows the resonance frequency with eliminated geometrical implications for varying PE energies (left) and varying beam currents at a constant PE energy of 30 keV (right). As mentioned above, the gained values are increased at both highest and lowest PE energies used for pillar deposition. This is a surprising fact as on first sight one cannot expect similar behavior for both highest and lowest PE energies since all deposition related parameter rise or fall permanently with increasing electron energy, e.g. the dissociation cross section for precursor molecules, as described in detail in chapter 1.4. In contrast, the situation for increasing currents (right) reveals a clear trend: The geometry adjusted resonance frequency rises with increasing currents.

Now considering Euler-Bernoulli's formula again, the ordinate of both plots reveals following proportionalities:

$$f_0\frac{h^2}{w} \sim \sqrt{\frac{E}{\rho}} \tag{6.1}$$

Thus, the values plotted in Figure 6-12depend on Young's modulus *E* and the mean density *ρ*, both of them being internal parameters independent of outer dimensions. Especially Young's modulus is of great importance for the gas sensing concept as it enables deriving elasiticity and stiffness, respectively. Unfortunately, Figure 6-12 only provides information about the ratio $\sqrt{E/\rho}$. As a result, further experiments necessarily had to be done to decouple these two parameters from each other. By that, electrostatic experiments and finite element simulations had been performed to gain Young's modulus (cf. chapters 6.4 and 6.5) and EDX measurement provided information about the chemical composition and thereby the mean density which will be discussed in the following. Of course, identifying E would determine ρ via Euler-Bernoulli and equation (5.13) and vice versa, but the applicability of this equation on quasi-1D resonators has not been already proven. Hence, reliable conclusions can only be drawn if both internal parameters have been determined independently which will be described in the following chapters.

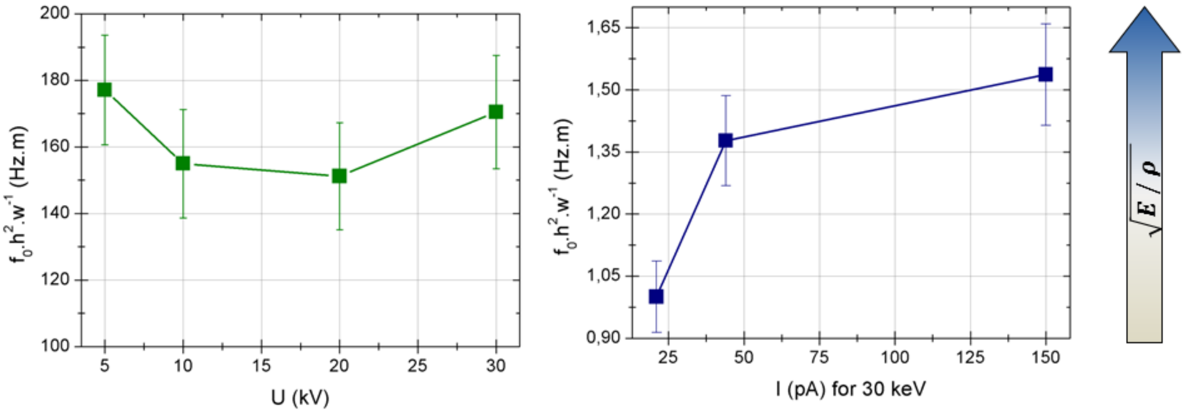

Figure 6-12: Resonance frequency released from geometric influences for one particular set of pillars for varying PE energies (left). It is enhanced for both highest and lowest PE energies. Results for varying beam currents at a PE energy of 30 keV reveals an increase with rising currents.

6.3 Chemical Analyses

Starting with the mean density ρ, EDX measurements were carried out as described in detail in chapter 4.1.2.5. The X-ray information originates from pillar sections above a height of 2 µm since this marks the critical threshold of constant precursor replenishment (GFR). Therefore, a constant Pt content for further growing pillars can only be achieved above this threshold as is proven by Plank-[14] It was also revealed that the Pt content usually is highest at the base of these Pt-C-structures, decreasing with increasing height until it reaches this constant level. However, we want to emphasize that the material properties ***in comparison*** to other deposition parameters for a fundamental understanding are more important than absolute values. The results are given in Figure 6-13. The C/Pt ratio reveals the peak-to-peak-ratio R_{PtC}.

The Pt content can be calculated using a quantification process described by Winkler et al.[7]:

$$Content_{Pt}[at.\%] = 12.04 \cdot {R_{PtC}}^{-0.879} \tag{6.2}$$

Overall, 26 pillars were investigated deposited with 5, 10, 20, and 30 keV and lowest currents (5, 7.5, 13, and 21 pA) and additionally with higher currents at 30 keV, viz. 44 pA and 150 pA. On the left hand side, one can see the results for lowest current at different PE energies; the right plot reveals those for varying currents at 30 keV. One can see that the Pt content decreases at higher currents, which was previously shown by Plank et al.[14] and strongly supports the results we gathered from growth rates (cf. in chapter 6.1). VGR results for higher currents indicate a depletion of precursor molecules on the top of the growing pillar. This local depletion is equivalent to a local lack of precursor molecules compared to potentially dissociating precursor molecules. It can be found in literature that an excess of electrons leads to a reduced Pt content for growing nano-pillars.[14] Hence, EDX measurements are in perfect agreement with the conclusions drawn in chapter 6.1.

The situation is different for varying PE energies and the respective lowest possible currents as the Pt content does not change monotonically. Nano-pillars deposited with 10 keV and 20 keV exhibit a smaller Pt content than those deposited with 5 keV and 30 keV. A similar behavior can also be observed for resonance frequencies with enhanced values at 5 keV and 30 keV (cf. Figure 6-12).

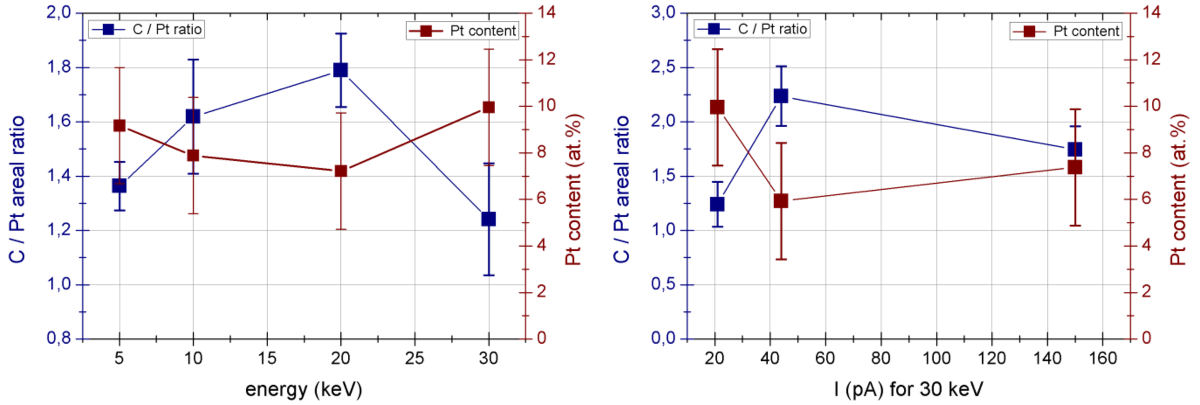

Figure 6-13: C / Pt ratio (green) and Pt content (red) of pillars deposited with varying PE energies and minimal currents (left) and varying currents at 30 keV (right).

The results of EDX analyses allow a first estimation of the density using average values for pristine carbon in a glassy state which is supposed to describe the carbon matrix appropriately[46,47] and Pt[48] (cf. Table 6-4) via

$$\rho_{hom}[g/cm^3] = c_C \cdot 1.4\,[g/cm^3] + c_{Pt} \cdot 21.45\,[g/cm^3] \tag{6.3}$$

In order to connect the results from chapter 6.2 with EDX measurements we need to take a glance at equation (5.16). Reordering Euler-Bernoulli's equation for a cylindrical beam one gets:

$$f_0 \frac{h^2}{w} \sim \sqrt{\frac{E}{\rho}} \tag{6.4}$$

The left side in equation (6.4) has been determined via previous electrodynamic measurements; ρ can be calculated from EDX analyses. As one can see, these experimental results are inversely proportional to each other. However, 5 keV and 30 keV resonators exhibit ***both a higher resonance frequencies and a higher average density*** (Figure 6-12 and Figure 6-13 respectively) since an enhanced Pt level is equivalent to a higher average density of the resonator. The solution to this apparent contradiction has to be found in Young's modulus. This means that an enhanced Pt level has to increase Young's modulus E even more than the density to lead to an enhanced resonance frequency, as $f_{res} \sim \sqrt{E/\rho}$. In order to prove this statement it is inevitable to determine Young's modulus separately. For that, pillars' deflections with respect to the applied voltage were measured (see next chapter) in order to consequently simulate Young's modulus via FES software Comsol®, and Matlab®.

6.4 Deflection Experiments

The electrodynamic resonance method allowed the identification of the intrinsic resonance frequency for quasi-1D nano-resonators applying an AC voltage to the counter electrode with the appropriate frequency (chapter 6.2). Using a DC voltage leads to constant deflection of the nano-pillar towards the counter electrode due to electrostatic forces. The deflection can be measured via SEM. However, frame times have to be kept as short as possible to avoid charging of the pillar which changes the appearing deflection. The detailed experimental setup for these electrostatic deflection experiments can be obtained from chapter 4.1.2.1. Subsequently, it is possible to determine Young's modulus via FES (cf. chapter 4.1.3). These results will be discussed in the following chapter 6.5.

Figure 6-14 shows the deflection with respect to the applied DC voltage and thus the force for varying PE energies (left) and different currents for a PE energy of 30 keV (right). As evident, 5 keV and 30 keV pillars show less deflection and thereby exhibit higher stiffness. This is in agreement with the result gathered from EDX measurements (chapter 6.3) which suggested a higher metal content for quasi-1D structures deposited with these two PE energies on the expense of less “soft” carbon. According to Euler-Bernoulli’s equation (6.1,) the resonance frequency is also increased with enhanced stiffness ($f_0 \sim E$). Hence, results from electrostatic experiments are in agreement with resonance frequencies (chapter 6.2.2) which were higher for 5 keV and 30 keV nano-resonators.

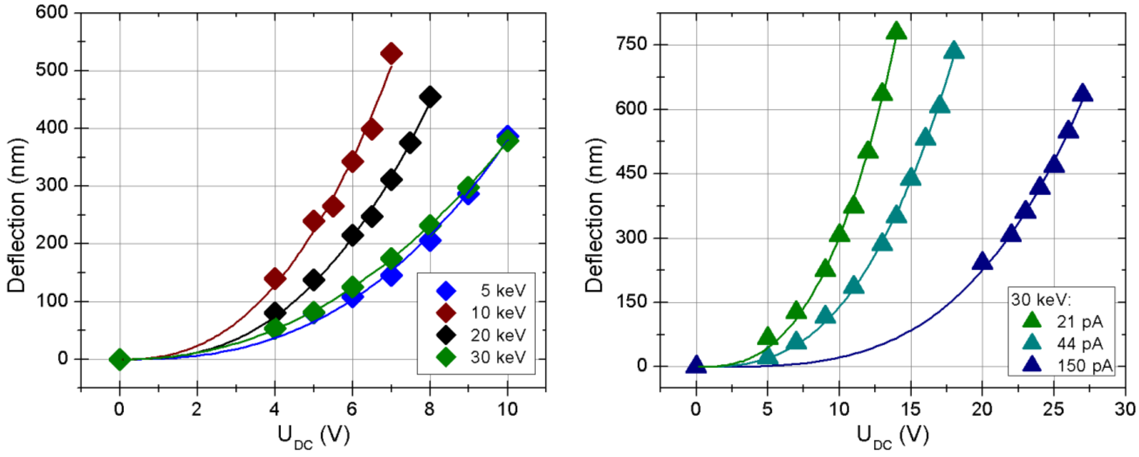

Figure 6-14: Net deflection of pillars with respect to the applied voltage for varying PE energies (left) and differing currents at 30 keV (right). The colors indicate different deposition parameters.

Previous experiments revealed influence of geometric deviations on pillar properties. Especially the impact of varying widths arising from unstable stigmator settings tends to be very strong due to the extreme aspect ratios of quasi-1D resonators with diameters of down to ~ 65 nm. According to equation (5.9) the maximum deflection d_{max} at uniform load for a cylindrical beam with diameter *w* and height *h* (equation (5.15)) follows:

$$d_{max} \sim \frac{q_0 h^4}{E w^4} \tag{6.5}$$

In order to dispel any doubts, the maximum deflection d_{max} from deflection experiments was multiplied by w^4/h^4. Thereby it is possible to correct geometrical influences which proved to be necessary for resonance frequencies (chapter 6.2.2). However, in the case of deflection experiments, geometrical influences do not affect the results from Figure 6-14 considerably, as can be seen in Figure 6-15.

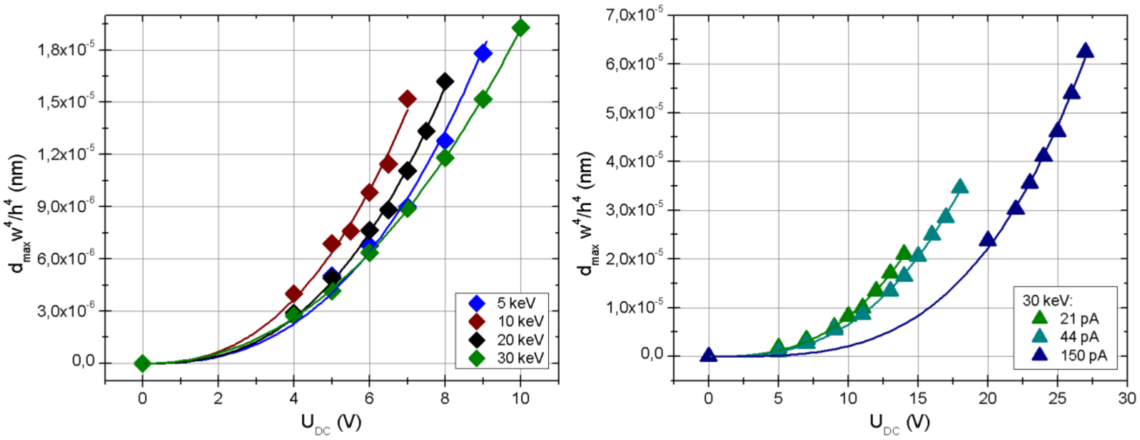

Figure 6-15: Voltage induced maximum deflection of the pillar multiplied by the ratio of radius and height to the fourth to adjust results for geometrical influences. As the plot is similar to Figure 6-14, the influence of geometry is negligible for qualitative analysis.

Summing up the results we gathered from deflection experiments it can be said that the conclusions drawn from previous analysis, i.e. resonance frequencies in chapter 6.2.2 and chemical analysis (chapter 6.3), has been confirmed. There it was revealed that 5 keV and 30 keV nano-pillars contain more Pt and exhibit higher resonance frequencies even if they are adjusted for geometries. Equal relations have been found for increasing currents. It is reasonable that resonators have an increased stiffness if they contain more metal leading to enhanced natural frequencies. Electrostatic experiments strongly support this argumentation as the revealed deflection diminishes for increasing currents as well as for structures deposited with 5 keV and 30 keV structures compared to intermediate PE energies. This behavior is also visible if deflections are purged from geometrical influences.

However, the approximation of a uniform load is not precise as the electrostatic force on the pillar depends on the distance between the counter electrode and the pillar itself. Bending of the pillar leads to a reduced distance and therefore a larger electrostatic force proportional to the pillar's deflection. Hence, a more thorough method must be used for analysis which takes dynamics into account. The solution for this issue has been found in FES. Implementing COMSOL® simulations in a Matlab® routine enables not only the ability to compare deflections reliably but makes it also possible to calculate Young's modulus, a characteristic number of the pillar's stiffness independent from geometry and an important quantity for elastic mechanics considerations, e.g. Euler-Bernoulli beam theory (chapter 5.1.1.).

Before we take this next step an undesired detail should be mentioned. Applying positive and negative voltages uncovers a slightly divergent behavior in the displayed deflection. In theory, the force on the grounded pillar depends only on the absolute value of the applied voltage or the difference in voltage between the counter electrode and the pillar respectively. However, the deflection of the pillar towards the counter electrode is considerably smaller at negative voltages (Figure 6-16). This phenomenon was observed in every deflection experiment. A likely explanation would be implanted electrons as consequence of the e-beam exposure during the deposition process. As such FEBID structure exhibit bad electrical conductivities, charging is likely to occur. An overall negative charge Q_e would increase the force and thus the deflection when a positive voltage is applied and vice versa. An additional aspect is the work-function difference between pillars and the Au electrode which could lead to a slight offset in the range of 1 eV for all pillars. However, further experiments have to be done in the future to verify these presumptions. In addition, as this behavior has been found in all measurements, it does not affect the observed trends but it only affects quantitative considerations. We just have to keep in mind that the real difference in potential between pillar and counter electrode tends to be higher than the applied voltage which increases deflection and thereby decreases calculated Young's modulus.

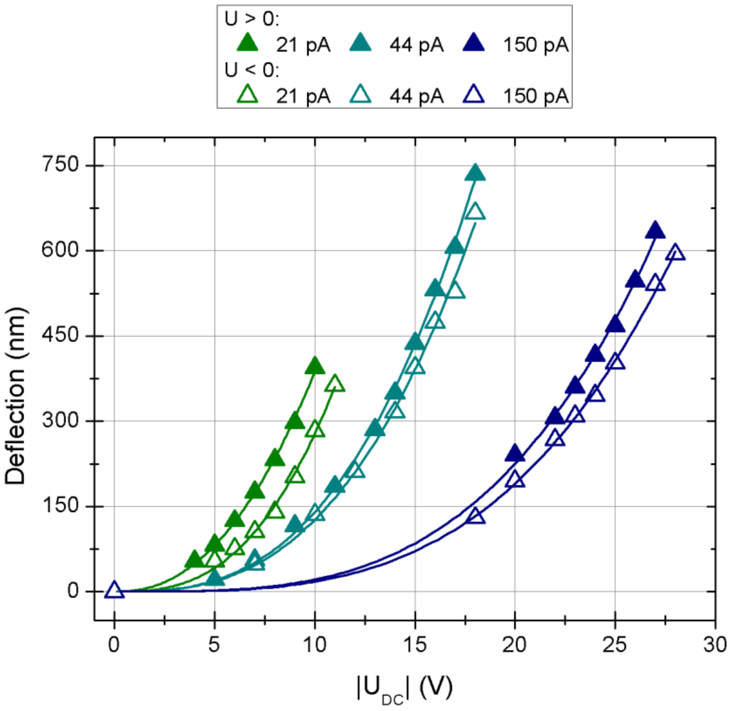

Figure 6-16: Comparison of deflection applying a positive voltage (squares) and negative voltages (stars) for uncured pillars (top) and cured pillars (bottom).

6.5 Finite Element Simulations

FES enables a calculation of the system’s electric field with high accuracy. As a result, it is possible to derive the electrostatic force acting on the resonator. Young’s modulus repels a displacement caused by an attractive force on the resonator and is connected to the applied force via equation (2.1). Hence, this quantity can be calculated with the information provided by deflection experiments (chapter 6.4).

In order to provide a model of the resonating setup including resonator, counter electrode, and surroundings and is as accurate as possible a variety of geometrical parameters has to be determined (Figure 4-6). Special emphasis has to be put on conscientious measurements of these geometries to gather trustworthy information about the Young modulus from simulations. Naturally, there is little influence on Young modulus’ calculation by parts of the counter electrode which are far away from the pillar itself. Hence, the “vertical” and “horizontal square sizes” were merged into one parameter with a mean value. Unfortunately, although revealing a strong influence on the simulation results, it was highly sophisticated to measure the parameter “hole depth”. As a result, this parameter mostly determines the uncertainty of the calculation.

Table 6-3: Geometries of resonance systems used for calculating Young’s modulus. Further information concerning the denomination of geometric parameters can be derived from chapter 4.1.3. Please note that the values defining the pillar width are given in nm.

Pillar **Geom. quantity / µm**	**1-5**	**2-5**	**3-5**	**4-5**	**1-10**	**3-10**	**1-20**	**3-20**	**1-30**	**3-30**
Pillar height	5.03	5.02	5.06	5.09	4.97	5.06	5.10	4.83	4.18	4.85
Pillar width · 10^3	74.6	75.0	79.9	78.2	74.8	66.8	75.4	67.4	66.1	72.8
Hole Depth	1.4	1.45	1.5	1.5	1.3	1.3	1.3	1.5	1.3	1.3
Elec Width	2.33	2.43	2.43	2.50	2.17	2.49	2.17	2.49	2.36	2.50
Elec Length	9.00	8.93	9.3	9.20	9.03	9.20	8.95	9.24	9.10	9.60
Elec Height	3.52	3.47	3.46	3.55	3.33	3.50	3.37	3.6	3.35	3.52
Square Size vert.	9.80	--	10.3	10.7	9.60	10.5	9.7	10.6	9.72	--
Square Size hor.	9.40	--	9.55	9.50	8.90	9.50	9.00	9.50	9.24	--
Square Gap left	1.02	0.90	1.30	0.89	1.10	1.14	0.93	1.00	1.07	--
Square Gap right	0.79	0.80	1.30	0.87	1.00	1.14	1.02	1.10	1.33	--
Square Gap up	3.10	3.05	2.50	3.05	3.40	2.55	3.33	2.50	3.14	--
Pillar – VDD	2.38	2.50	2.43	2.41	2.50	2.42	2.49	2.43	2.50	2.43
Pillar – GND	6.07	5.90	6.10	5.88	6.08	6.17	5.82	6.18	5.81	6.10
Hole – VDD	2.25	1.00	0.9	1.57	0.90	1.03	0.56	0.94	0.83	0.84
Hole – GND	2.65	4.02	3.89	3.54	3.16	3.87	4.12	3.94	3.67	4.04

The gathered results were also largely dependent on the shape of the front area of the metal electrode as it is closest to the resonator and the largest force on the pillar emanates from there. In general, the front part of the electrode was rounded and therefore not a perfect cuboid. Rather than that, the cross section looked similar to the half of an ellipse. What is more, the shape of this ellipse depends on the stigmator settings of the ion beam and therefore varies at non-successive milling processes. In order to provide simulation results as close to reality as possible the elliptic cross section was analyzed in more detail. The electrode's width was measured every 500 nm in vertical direction. This data was included in the simulated shape of the electrode. By varying input parameters within the maximal measurement error and analyzing consequences on the simulation an uncertainty was estimated with 2.5 GPa for gathered values.

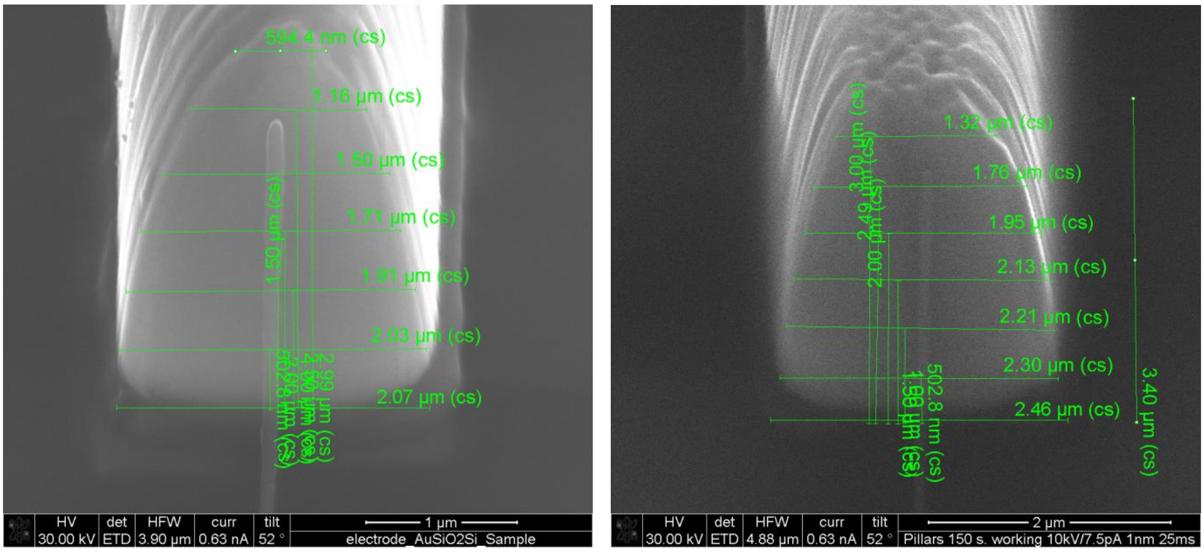

Figure 6-17: Images revealing the geometric measurements of electrode's front areas which differ in size and shape. The pillar can be seen in front of the electrode.

Figure 6-18 reveals that this thorough analysis of deflection experiments agrees well with resonance experiments (chapter 6.2.2) and EDX measurements (chapter 6.3). 5 keV and 30 keV nano-resonators are stiffer as they exhibit higher elastic moduli. As a consequence the resonance frequency is enhanced, too. Considering the internal composition, this is additionally in accordance to the results of the chemical analysis, as a higher content of "hard" Pt compared to "soft" carbon is suggested. Increasing moduli for higher currents also coincide with the results from previous chapters as they provided the outcome that the Pt content as well as the resonance frequency is raised by increasing currents (Figure 6-18, right). A quantitative analysis of Young's modulus will be given in chapter 6.8.

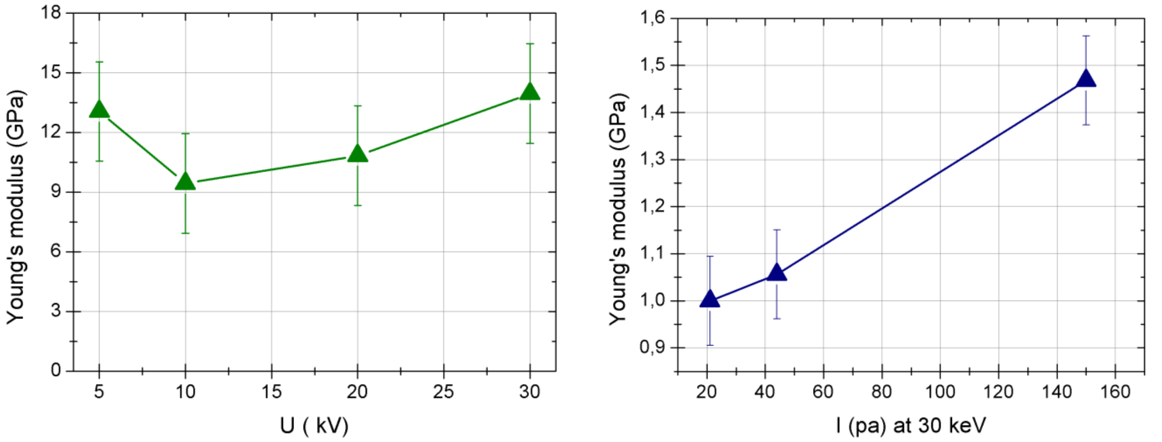

Figure 6-18: Young's modulus calculated from electrostatic deflection for varying PE energies (left) and different currents at 30 keV (right). Similar to results gathered from resonance experiments, 5 keV and 30 keV pillars exhibit an increased stiffness compared intermediate PE energies. Young's modulus also increases with increasing currents.

Now all physical quantities in Euler-Bernoulli's equation (5.9) have been determined via independent experiments and analysis. This has been performed for varying PE energies and varying currents. The conclusions drawn from that shall be summed up in the following chapter.

6.6 Influences of Deposition Parameters on Quasi-1D Nano-Resonators

At first, geometry investigations revealed that the deposition of quasi-1D nano-resonators is a highly sophisticated procedure. The minimal diameter of such structures (60 – 70 nm) pushes FEBID fabrication to its limits. As a result, deviations occur in diameters and height of up to ± 4 % which cannot be avoided. Fortunately, Stermitz et al.[22] proved that the resonance frequency of nano-resonators behaves as $f_{res} \sim w/h^2$, which is predicted by Euler-Bernoulli beam theory (chapter 5.1.1). Hence, it was possible to adjust the resonance frequency measured by AC field excitation for geometric influences. This procedure disclosed an increased resonance frequency at highest (30 keV) and lowest (5 keV) PE energies compared to intermediate ones (10 keV and 20 keV) as well as an increasing resonance frequency for higher currents at a specific PE energy (30 keV) (cf. chapter 6.2.2). As geometrical influences were compensated, this has to arise from internal, structural peculiarities. In accordance to these first outcomes, EDX measurements discussed in chapter 6.3 proved that 5 keV and 30 keV nano-pillars contain more Pt compared to "soft" carbon. An increase in the Pt content can also be found for increasing currents. In addition, FES (chapter 6.5) on the basis of experimental data gathered from electrostatic deflection experiments (chapter 6.4) demonstrated higher elastic moduli, i.e. an enhanced stiffness for pillars with higher Pt content. In order to completely understand these results, we have to connect the data of varying energies with the results of varying currents. As mentioned in chapter 6.1 (Table 6-1), using different PE energies implies the use of varying currents as the corresponding beam current cannot be arbitrary set. As discussed in detail in chapter 1.7, the dissociation process and thereby the chemistry of the deposit strongly depends on the working regime and therefore the ratio of available precursor molecules and potentially dissociating electrons. Hence, slightly different beam currents at different primary energies lead to two tendencies that overlap in the gathered results as visualized in Figure 6-19:

1) *Increasing PE energies decrease the dissociation cross section (green).*
2) *Increasing currents enhance the number of electrons (cyan).*

Both phenomena have been proven concordantly in literature.[1,14] Hence, it can be stated that these first experiments and their analyses provide the knowledge about influences of deposition parameter for FEBID fabrication of quasi-1D nano-resonators on the composition and as a consequence on elastic properties and the intrinsic resonance frequency. What is more, it was possible to find a consistent theory of causalities for these influences of deposition parameter on the chemical composition. Considering the observed macroscopic properties, namely the resonance frequency and geometric dimensions, all quantities are in accordance to Euler-Bernoulli's equation (5.9) in a qualitative manner. However, in order to gather a precise mathematical description of the relations, we need to check Euler-Bernoulli's equation exactly for correctness, which will be discussed in the following.

$$f_{res,cyl}\frac{h^2}{w} \sim \sqrt{\frac{\boldsymbol{E}}{\boldsymbol{\rho}}}$$

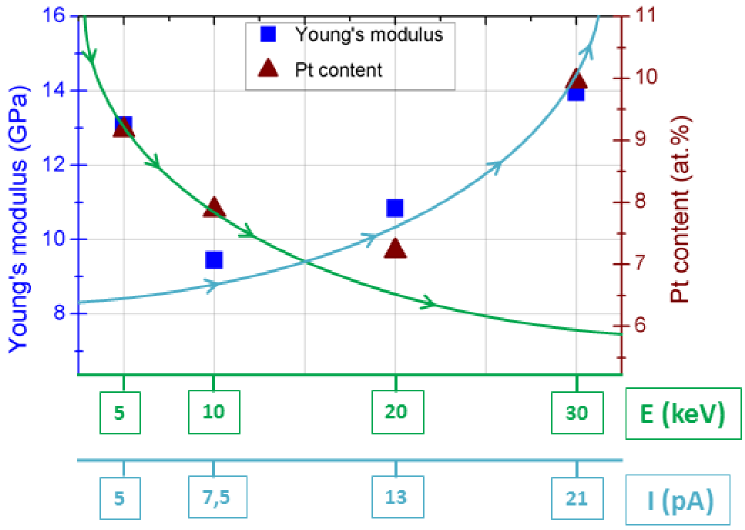

Figure 6-19: Effect of deposition parameters on Young's modulus (blue) and Pt content (red) of quasi-1D nano-resonators. Increasing PE energy (green) leads to a reduced dissociation cross section concerning precursor molecules which diminishes the amount of Pt in the deposit. In contrast, an increasing beam current (cyan) enhances the number of potentially dissociating electrons and increases the Pt content as well as Young's modulus.

6.7 Applicability of Euler-Bernoulli Beam Theory for Quasi-1D Nano-Resonators

Euler-Bernoulli's equation (5.16) plays a key role in analyses performed so far. However, exact proportionalities have only been used between the resonance frequency and geometries (cf. chapter 6.2.2) as the dependency $f_0 \sim w/h^2$ has already been demonstrated for FEBID nano-pillars.[22] In further discussion, it has been solely assumed that the resonance frequency increases with enhanced Young's modulus and decreases with higher average densities, i.e. $f_0 \sim E^x/\rho^y$ with $x, y > 0$. However, we determined all quantities in Euler-Bernoulli's formula from uncorrelated experiments: Densities $\boldsymbol{\rho}$ were calculated from EDX measurements (chapter 6.3) and Young's modulus $\boldsymbol{E}$ was derived from simulations based on bending experiments described in chapter 6.4 and 6.5. Geometrical dimensions (w and h, cf. chapter 6.1) and the resonance frequency (f_0 in chapter 6.2.2) were measured by the microscope. Thus, it is possible to check if this formula is applicable for FEBID fabricated quasi-1D resonators, as described in detail in chapter 5.4.1. It simply affords calculation of the proportional constant of Euler-Bernoulli's equation which is referred to as c_{np} (**nano-p**illar) via

$$c_{np} = f_{res,pillar} \frac{h^2}{w} \sqrt{\frac{\rho}{E}} \tag{6.6}$$

The results are given in Figure 6-20: The values for this factor c_{np} scatter around an average value and do ***not reflect the trends***, which could be observed in experiments, i.e. enhanced value for 5 keV and 30 keV. Hence, quasi-1D resonators follow the relations of Euler-Bernoulli and the equation can be adjusted according to equation (5.17).

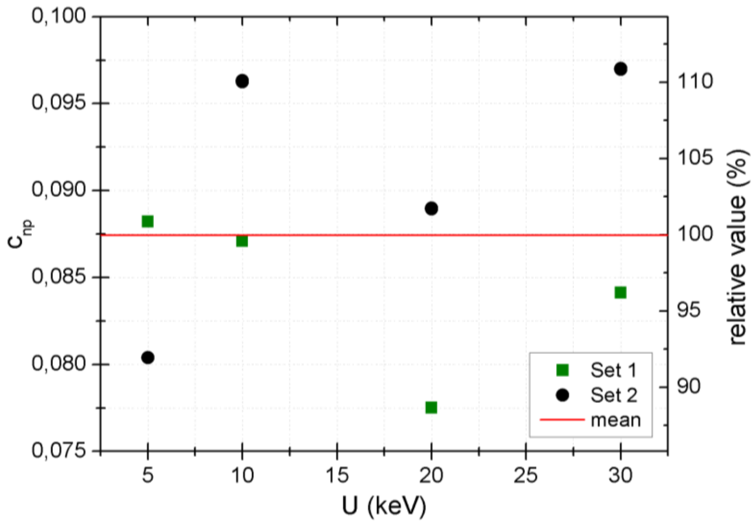

Figure 6-20: Backward calculated proportional constant in Euler-Bernoulli's equation via values for f_0, w, h, E, and ρ determined by independent experiments.

As a result, the deposited quasi-1D resonators can be described via

$$f_{res,pillar} = 0.087 \frac{w}{h^2} \sqrt{\frac{E}{\rho}} \tag{6.7}$$

Although the gathered value 0.087 ± 0.007 is constant, it differs from the theoretical value of 0.1978 (cf. equation (5.16)) significantly. However, we do not expect this factor derived from experiments to match the theoretical constant since we have to consider systematic deviations due to different reasons:

- *The **width** is not constant along the pillar. At the bottom and at the top of the pillar there is a non-linear increase in width up to 40 %.*
- *The **EDX measurements** were performed at regions in the upper third of the pillar to ensure similar precursor replenishment independent of the PE energy, but the chemical composition slightly changes along the pillar's main axis.*
- *The **average density** was only estimated from the chemical composition and the densities for pristine materials which is of relevance for the carbon part.*
- *The influence of **charging** is experimentally barely accessible and might have caused enhanced deflection and therefore reduced elastic modulus.*

A question mark has to be put especially after EDX measurements as Plank et al.[14] revealed a significant decrease in the Pt content with increasing heights. Thus, we can expect that the average density of the nano-pillar is slightly higher than the result of our EDX measurement performed in the upper third section of deposited quasi-1D structures. According to equation (6.6) a higher density would also lead to an increased proportional constant c_{np}. Hence, a higher density in lower parts of the pillar could explain the deviation from the theoretical formula. On the other hand, Utke et al. identified average densities for a copper precursor revealing also this metal-matrix structure in the range of pure graphite (cf. Table 2-1) and therefore much lower than values we gather from equation (6.3). However, the factor c_{np} was introduced just with the intention to take these systematic deviations into account. In addition, it has to be emphasized again that a qualitative point of view in order to identify trends in dependence of deposition parameter is much more important than absolute values.

Please note that we do not consider only one set of pillars in Figure 6-20 although we used to do that in the whole discussion. This is permissible since the situation for the calculation of c_{np} has changed. In previous discussion the experimentally derived quantities were compared with respect to deposition parameters. As Figure 6-11 revealed that these quantities are influenced by the date of fabrication, i.e. gas filling level etc. it was inevitable to use only one set for relative comparison. Now, we consider systematic deviations from the theoretical formula arising from reasons mentioned above. These deviations do not depend on the date of fabrication but are caused by differences of real FEBID structures from ideally shaped, homogenous materials. Hence, the used approach is justified.

As a first conclusion it can be stated that we obtained a detailed mathematical description for first mode mechanical oscillations of quasi-1D resonators AND the knowledge about influences arising from deposition parameters during fabrication. However, due to unavoidable deviations in FEBID deposition of these limit-pushing structures (e.g. stigmator settings), even this comprehensive insight does not allow the fabrication of nano-resonators matching exactly the desired frequency. Only a particular range can be estimated for the point of resonance. This problem can be met by the processes which are generated by irradiation electrons after the initial deposition process (post growth e-beam treatment). This will be discussed in the following chapter.

6.8 Post-growth E-Beam Treatment (Curing)

Previous works[33,34] revealed that deposits fabricated via FEBID react under e-beam exposure. Incompletely dissociated molecules are likely to finally dissociate under post-growth-treatment (PGT), also referred to as 'curing'. Stermitz et al.[22] investigated thoroughly the influence of PGT on 5 keV nano-resonators deposited with the same precursor gas for exposure to 30 keV PE electrons. His studies provided five main outcomes:

1) *E-beam PGT significantly increases the resonance frequency*
2) *Outer dimensions of pillars remain widely unaffected (± 4 %)*
3) *According to EDX measurements the chemical composition is rather constant*
4) *Pt grains in the metal-carbon matrix slightly grow from 1.7 to 2.2 nm*
5) *The carbon matrix gets graphitized for long e-beam PGTs*

The latter two affect the internal structure and therefore change mechanical properties. PGT induces further dissociation of not or incompletely dissociated precursor molecules in the carbon phase. This reaction results in dissociated Pt atoms which diffuse to large Pt nano-particles. Hence, it is possible that Pt grains grow without a change of the overall chemical composition and thus the average density. The graphitization is induced by the large amount of electrons impinging the carbon phase. Stermitz demonstrated that the resonance frequency could be doubled with PGT by a change of the internal metal-matrix structure at simultaneously constant chemical composition and similar outer dimensions. A bright field TEM images demonstrates the occurring processes. After fabrication the Pt grains (dark regions) are isolated from each other by a carbon matrix (bright). The whole structure is surrounded by a thin outer carbon layer (Figure 6-21a). PGT of the pillar for 3000 s led to a significant growth of Pt grains (b) and the formation of graphitic planes, which is visible in high resolution TEM images (c, black arrows). Both processes lead to an enhanced stiffness which increases the resonance frequency.

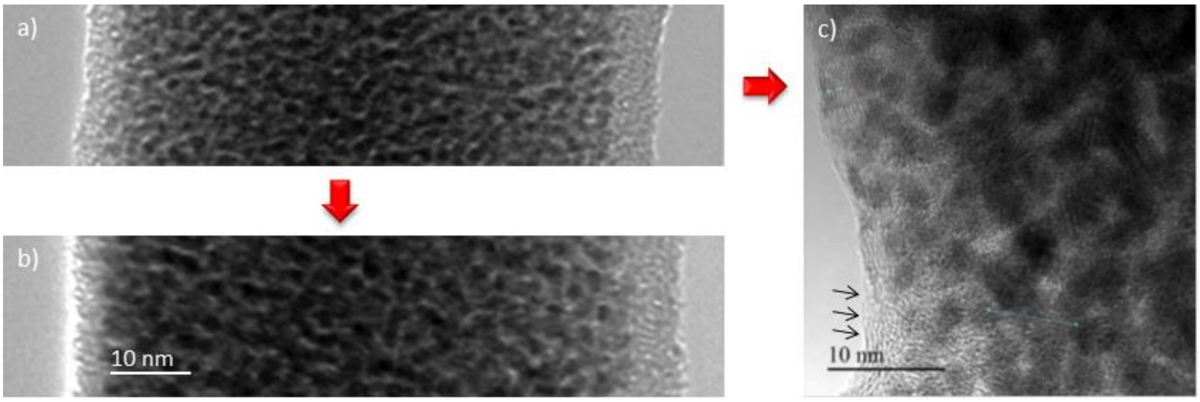

Figure 6-21: Bright field TEM image of an uncured pillar (a) and the same structure exposed to 30 keV electrons and a beam current of 21 pA for 3000 s. The Pt grain growth is clearly visible (b) as well as the forming graphitic planes (c). The latter one is marked by black arrows at some sites, where this effect is particularly visible [22, modified].

In this thesis, PGT was performed in top view as described in chapter 4.1.2.4. The structures were exposed to 30 keV electrons and a current of 44 pA for 3600 s. Generally, it is recommended to use higher currents as the yield of curing effects rises with the number of impinging electrons. However, 44 pA is the largest current which nano-pillars can be exposed to without the appearance of charge induced deformation of quasi-1D resonators. Deformation also occurs for lower PE energies. By that, the application of 30 keV electrons is required.

Figure 6-22 (left) reveals the resonance frequencies in dependency on total exposure times. The frequency increases significantly, if the pillar is exposed to the e-beam. The starting level differs due to varying resonance frequencies f_0. Resonance frequencies of 5 keV pillars (blue) and 30 keV (green) reveal a stronger increase although they already exhibit a higher starting frequency. On the right, corresponding frequencies with respect to the PE energies for different TET (0 s, 1800 s, and 3600 s) demonstrate that the trend illustrated in Figure 6-19 is maintained when curing is performed: An increased cross section for lower PE energies (5 keV) as well as an enhanced number of electrons for increasing currents (21 pA at 30 keV) lead to a higher Pt content resulting in an increased stiffness and an enhanced resonance frequency.

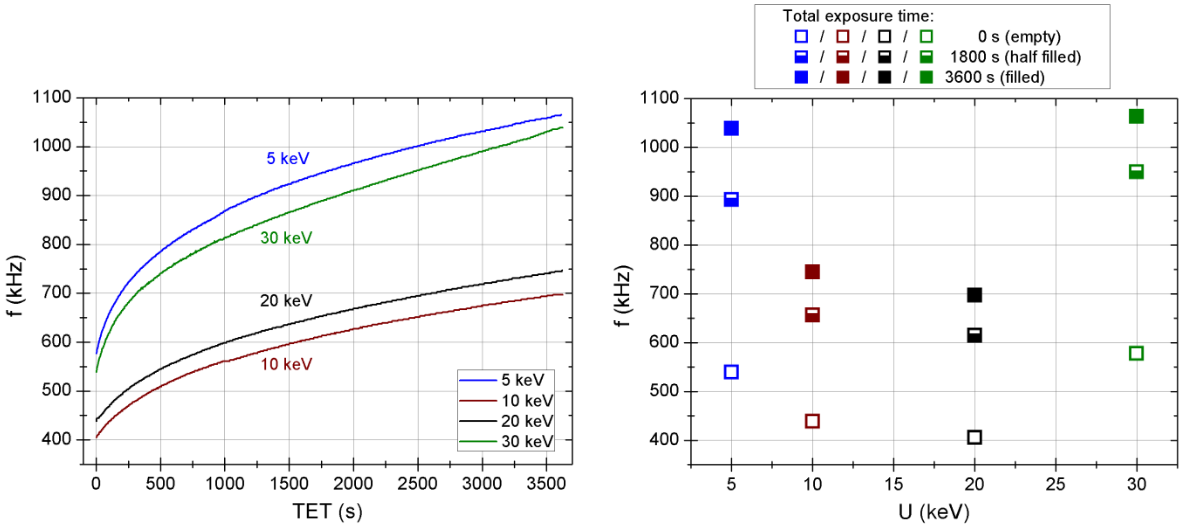

Figure 6-22: Development of the resonance frequency at PGT with 44 pA and 30 keV electrons for 3600 s (left). The frequencies rise significantly under e-beam exposure. The right plot reveals the frequencies with respect to the PE energy at the beginning, mid-time and at the end of PGT. Frequencies of 5 keV and 30 keV pillars are enhanced throughout the entire curing process.

However, in order to be able to compare these curing curves in a reliable manner, several mathematic operations have to be performed. At first, we only want to consider changes in pillar properties induced by PGT. As a result, the initial resonance frequency f_0 has to be drawn off. In order to regard also the dynamics of curing process plots are normalized to enable comparing of the curvatures of particular curing curves. In order to satisfy all requirements from above, some or even all of the following mathematic operations were performed on the data shown below:

- *Following plots reveal **changes** caused by PGT, i.e. Δf etc.*
- *In order to gather **normalized** curves, the last point was pinned at a value of one to reveal the relative development and to be able to compare respective curvatures.*

As mentioned above, the shift of the resonance frequency under e-beam radiation is induced by ***1)*** Pt grain ripening, and ***2)*** carbon graphitization. The frequency shift is larger for 5 keV and 30 keV nano-pillars (Figure 6-23, left). Plotting the curvature (right) discloses an important feature concerning the dynamics of curing processes: Although there is a faster increase for 5 keV and 30 keV at the beginning of curing, there is a stronger trend towards saturation for longer TET. The reason for such a behavior has to be found in post-deposition dissociation induced by PGT and a subsequent ripening of Pt grains. Remembering the description of dissociation for the used precursor in chapter 3.1.4, it was mentioned that a complete dissociation of a precursor molecule implies tens of electron interactions for full dissociation. As all quasi-1D structures were deposited with lowest currents and therefore ELR like conditions, resonators contain a large number of not dissociated and partly dissociated precursor molecules. On the other hand considering EDX results from chapter

6.3, a higher Pt content was found for highest and lowest PE energies (5 keV and 30 keV). This indicates advanced dissociation processes during deposition, i.e. a higher degree of dissociation which explains both stronger curing effects at the beginning and sooner saturation:

1) *Due to a higher degree of dissociation precursor molecules are better 'prepared', descriptively spoken, for further interaction with electrons by PGT (→ strong curing)*
2) *Dissociation is finished earlier and the curing process relaxes.*

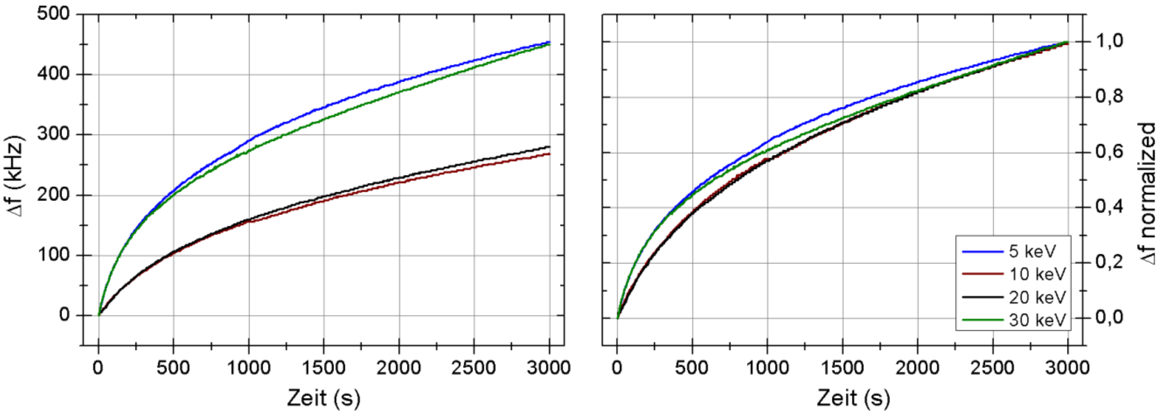

Figure 6-23: Changes of the resonance frequency with respect to the total exposure time (left). Shapes are original but the initial frequency after deposition was drawn off, for which reason all graphs start at 0 kHz. The right plot reveals the normalized data to visualize curing dynamics. The frequencies of 5keV and 30 keV rise faster but reveal a stronger trend towards saturation obvious by the higher curvature. The legend is valid for both plots.

So far it has been found that 5 keV and 30 keV pillars contain a higher degree of dissociation after deposition which agrees with an increased Pt content. However, further steps need to be taken to receive all facts involved in curing experiments.

It is known from geometrical characterization of nano-pillars (cf. chapter 6.1) that different deposition parameters involve varying geometric dimensions. Therefore, the dose (current × exposure time) is not equal for different pillars. Similar to previous chapters, curing results needs to be adjusted for geometric effects (cf. chapter 6.2.2). This procedure is additionally recommended by the fact that curing affects the internal metal-matrix structure much more than size and dimensions which widely remain the same during PGT (± 4 %). For that, parameters depending on the internal structure like Young's modulus E or the density ρ might provide a better insight in the changes coming along with PGT. The knowledge about geometrical dimensions enables to eliminate geometric influences and to calculate values proportional to the ratio E/ρ from equation (6.1). This procedure has already been described in detail in chapter 6.2.2. Thus, changes in the resonance frequency Δf become changes of internal parameters, viz. $\sim\Delta\,(E/\rho)$. The results of Stermitz et al. revealed that not only geometric dimensions remains widely unaffected from curing but also the chemical composition does not change.[22] As a result, the ***average density ρ is constant during the curing process*** and the results for $\Delta\,(\boldsymbol{E}/\boldsymbol{\rho})$ ***are equivalent to the change of Young's modulus***, i.e. $\Delta\,E/\rho$ or simply ΔE in arbitrary units.

Plotting ΔE (in AU) against the total exposure time provides a surprising fact as it reveals a rather ***linear dependency*** (Figure 6-24, left). Again 5 keV (blue) and 30 keV (green) rise faster in total values. Normalizing the evolution of ΔE (Figure 6-24, right) it is evident that the increase of Young's modulus for pillars deposited with those two energies slightly declines. On the contrary, the linear change of the Young's modulus is confirmed for 10 keV (red) and 20 keV (black). The slope of ΔE remains ***constant*** throughout the entire curing process which indicates an ongoing graphitization process assuming the dissociation process as finished, suggested by Porrati et al.[33] and Plank et al.[34].

It must be noted that the considerations above refer only to the applied curing process with 30 keV / 44 pA for about 3000 – 3600 s. It does not necessarily mean that the increase of ΔE remains constant for longer periods of e-beam radiation. In fact, it can be expected that the e-beam induced restructuring decelerates and the rise in Young's modulus slows down once the dissociation is entirely finished and most of the carbon is graphitized, respectively. However, the aim of these first experiments is to understand fundamental processes in quasi-1D resonators and to find suitable parameters to use for gas sensing applications. Thus, it is of great importance to know that the resonance frequency of resonators is tunable across almost the whole kHz range. This applies especially above 5 keV and 30 keV within a justifiably temporal expenditure.

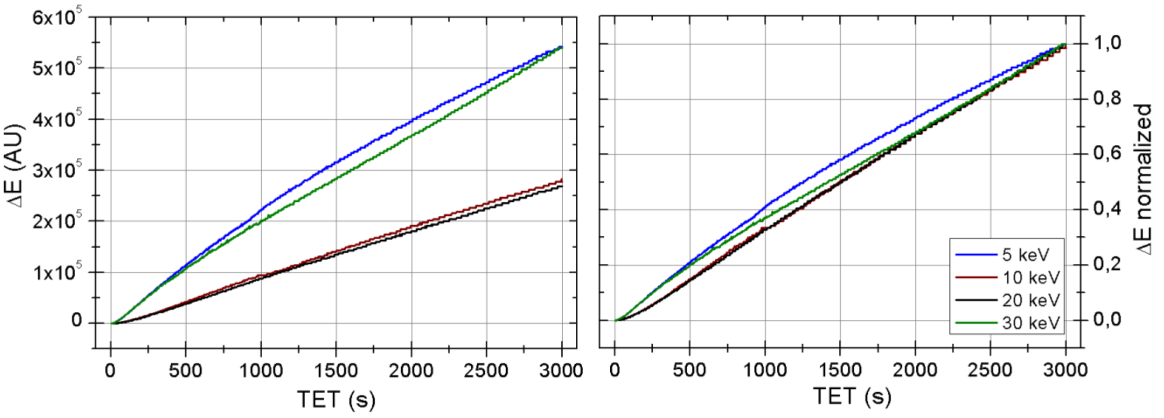

Figure 6-24: Time dependence of $\Delta E/\rho$ during curing process in absolute values (left) and normalized (right). The left graph reveals the evolution of $\Delta E/\rho$ or Young's modulus ΔE in AU calculated by the data plotted in Figure 6-23 via equation (6.1). Surprisingly, E develops almost linearly under e-beam radiation. In the right plot, one can see that the slope of E slightly decreases for 5 keV and 30 keV suggesting a slightly saturating curing process. In contrast, 10 keV and 20 keV exhibit a constant slope during PGT up to 3000 s.

As an initial summery about PGT it can be stated that 5 keV and 30 keV pillars exhibit a stronger increase of the resonance frequency in absolute values und electron radiation, but these pillars reveal a stronger curvature in normalized curing curves. This means that the curing process slows down more quickly. This behavior can be explained by the degree of dissociation which is higher for 5 keV and 30 keV resonators. As a result, the reactions generated by electron radiation proceed with higher velocity but are naturally finished faster. The shift of frequency adjusted for geometrical influences shows a rather linear dependence on the total exposure time. Together with the knowledge of previous works one can state that the overall mean density and geometric dimensions remain constant during PGT. The rising frequency is mainly caused by a rather ***linear*** increase of Young's modulus E within the used exposure times. Only 5 keV and 30 keV pillars show small deviations towards reduced slopes.

Another important feature for gas sensing application can be seen in Figure 6-25. A 10 keV and a 20 keV pillar were exposed to the e-beam two times, separated by 6 days and 72 days respectively. It turned out that the frequency shift arising from curing is almost completely ***irreversible***. The resonance frequency remained constant for 6 days and the resonance frequency of the 20 keV pillar suffers only the slight loss of 24 kHz after 72 (!) days. However, the sample was not stored in a high vacuum chamber during this period; thus, this minimal shift could arise from many different reasons as diffusion inside the structures by ambient molecules because this would increase the average density and therefore leads to a lowered resonance frequency (cf. equation (6.1)).

In addition, a break in the PGT leads to a stronger increase when it is continued again, whereas curing plots above (Figure 6-22 and Figure 6-23) may suggest that the frequency rise eventually saturates under permanent e-beam radiation. Concerning the widely ***constant*** resonance frequency after paused PGT, which indicates a widely stable internal structure, the strong increase at the beginning of a second e- beam exposure is even more remarkable. A kind of regeneration seems to take place inside the structure which is likely to be related to the aging effect described in literature[32,34].

Hence, the initial summary above about post-growth treatment can be expanded by another important feature: Once cured, the resonance frequency stays at a fairly equal level. Continued PGT revealed a strong ***increase after*** some days of ***regeneration*** without e-beam radiation. This is most probably caused by time related chemical changes of the Pt/C matrix (aging effect).

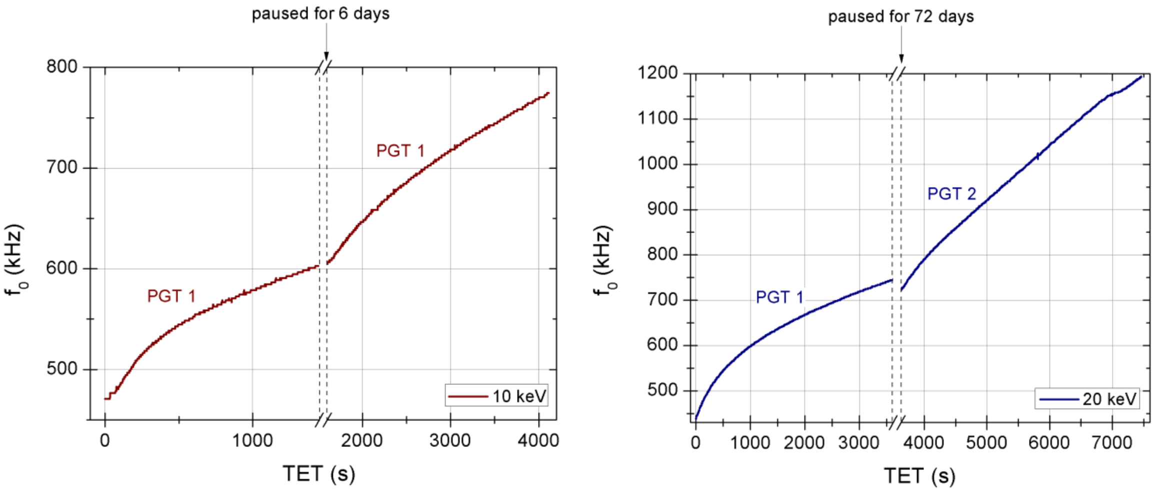

Figure 6-25: Development of resonance frequency during two periods of PGT. The curing for a 10 keV (left) and a 20 keV resonator (right) were temporally separated by 6 days and 72 days respectively. As one can see, the resonance frequency remained widely constant between the curing processes. When continuing an enhanced increase of the resonance frequency can be observed.

In order to prove the line of argument from the discussion above, namely that an increase of Young's modulus is responsible for the rising resonance frequency, deflection experiments were also performed after curing processes. Subsequently these results were used to calculate Young's modulus following the procedure from chapter 6.4 and 6.5. The results (Figure 6-26) strongly support the conclusions drawn from PGT. The stiffness of all structures is highly increased via e-beam treatment. 5 keV and 30 keV pillars reveal again a lower deflection with respect to the DC voltage than 10 keV and 20 keV.

Subsequent calculation of Young's moduli proves a considerable increase by curing processes (Figure 6-27, right). As mentioned above, this is caused by two effects: Growth of Pt grains from ~1.7 nm to ~2.2 nm and an at least partial transformation of the carbon phase in a graphite crystal structure. The first reduces the distance between neighboring Pt grains which is typically smaller than 0.5 nm for as-deposited structures. As a consequence the damping carbon phase between Pt grains is thinned which impedes bending of the structure

Quantitative analysis of Young's modulus discloses another fact which is not straight-forward. The values gathered for as-deposited nano-pillars at varying PE energies (Figure 6-27) are in the range of 9 GPa – 15 GPa. Taking into account the bulk elastic modulus for pristine Pt (168 GPa, cf. Table 6-4) or Pt nano-crystals (140 GPa) it is evident that the elastic properties of these nano-resonators are mainly determined by the carbon phase. TEM investigations of PtC nano-pillars suggest a very high sp2/sp3 carbon ratio above 80%[49] which is furthermore an argument for a small fraction of hydrogenated carbon[46]. In addition, a decreasing density and elastic modulus for an enhanced ratio of sp2-hybridised carbon has been demonstrated[50,51].

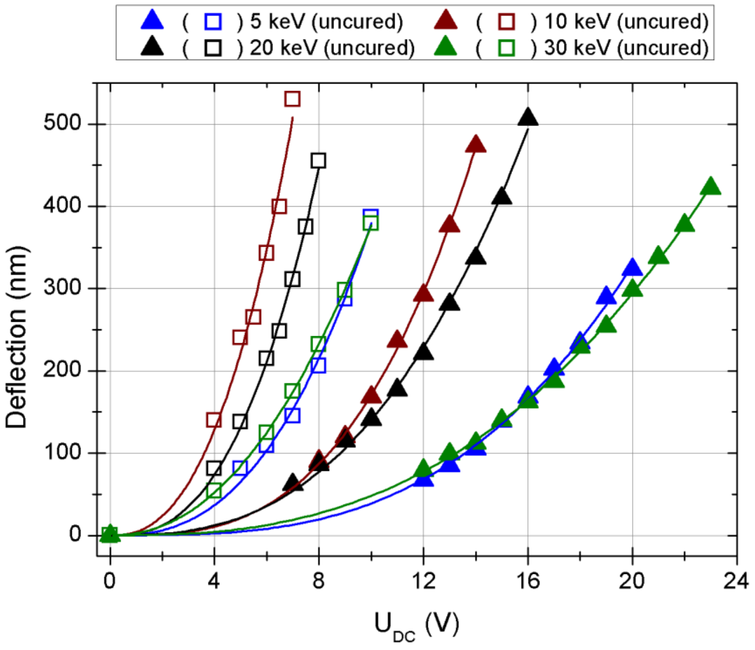

Figure 6-26: Net deflection of pillars with respect to the applied voltage. Comparing cured (solid triangles) and uncured (open squares) quasi-1D resonators reveals a significantly lowered deflection after PGT.

However, Table 6-4 reveals elastic moduli for nano-resonators that are similar to molecular solids with Van-der-Wall forces between single molecules, e.g. C_{60} (16 GPa). This is far below the elastic modulus in sp2-hybridized crystal graphite, even below Young's modulus between Van-der-Waal bonded basal planes in graphite (36 GPa) or that of glassy carbon (29-32 GPa)[46]. Similar moduli has only been found for disordered carbon nano-tubes (down to 10 GPa)[52] and polyhedral graphite particles, i.e. fine-grained graphite (12.8 GPa)[53]. Both of them exhibit a high concentration of defects. As the atomic bond length is highly correlated to the elastic properties of a material, the findings for as-deposited pillars suggest a loose network of mainly sp2-hybridized molecules inside the carbon matrix, containing additionally unchanged precursor molecules of fragments bonded via weak Van-der-Waal forces. These parts can be chemically activated easily which may explain the strong deformation occurring at exposure to low-keV electrons with a high interaction cross section. The considerations are also in accordance to transport simulations revealing good agreement with experimental results if the carbon matrix is treated as a material with polymer properties and dissolved voids[45]. This is also consistent with the fact, that long lasting static deflection leads to bending deformation, which indicates visco-elastic influences. However, the spatial distribution of Pt grains provides sufficient mechanical stability whereby this bending can be reversed by mechanical resonance oscillations which are completely elastic.

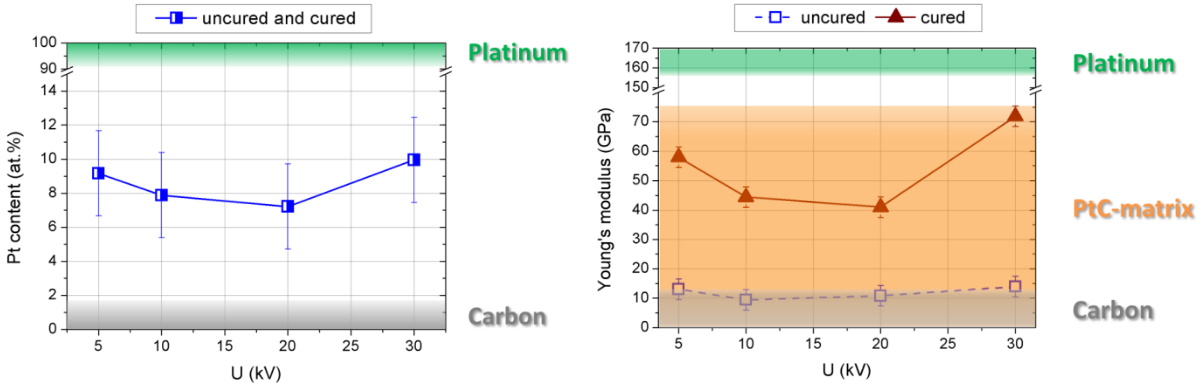

Figure 6-27: Estimated average density (left) and Young's modulus (right) of FEBID nano-pillars calculated from deflection experiments compared to the values of the components in pristine materials of platinum and carbon respectively. As one can see, the elastic properties are mainly determined by the carbon matrix (orange) although the material consists of Pt (green) and carbon (gray).

Table 6-4: Material properties for pristine components compared to quasi-1D nano-resonators consisting of a metal-matrix structure.

material		***R (Å)***	***ρ (g/cm^3)***	***E-modulus Uncured (GPa)***	***E-modulus Cured (GPa)***
Pt[1]	bulk		21.45	168	
	nano-crystals		21.4±0.4	139.7±2.7	
carbon[2]	C_{60} (fcc)		1.72	16	
	graphite (hex, sp2)	1.42	2.27	1020[3]; 36.3[4]	
	diamond (cubic, sp3)	1.54	3.52	1054	
	glassy C (~sp2)	1.42	1.3-1.55	29-32	
	aC (99% sp2)	1.43	1.9-2.0	140	
5 keV / 5 pA			3.78	13	50.65
10 keV / 7.5 pA			3.53	9	44.42
20 keV / 13 pA			3.40	10	41.06
30 keV / 21 pA			3.94	14	71.06

TEM images identified the formation of graphite planes after PGT (Figure 6-21). Similar behavior has been found for highly disordered catalytic nano-tubes supplied with thermal energy via 2500°C annealing whereby graphitic planes were much better aligned and Young's modulus was increased by one order of magnitude.[52] However, these planes do obviously not exhibit large extended networks as it is the case for pristine graphite but are arranged loosely (cf. Figure 6-21, c). This still strongly indicates a glassy carbon state which is characterized by convoluted sheets of graphite with small correlation lengths (intra-plane:

---

[1] 48

[2] 46,47

[3] a-axis

[4] c-axis

15 Å, inter-plane 5 – 15 Å)[46]. In contrast, amorphous carbon (***aC***) can also be almost exclusively sp2 bonded but exhibits a higher rate of cross-linking and disorder within one layer and a comparably high elastic modulus (140 GPa)[46]. Hence, elastic properties for glassy carbon are only determined by occasional inter-plane cross links and therefore slightly below the inter-plane modulus for graphite (36 GPa)[46]. As a result, when comparing with pristine bulk properties one has to consider the inter-plane elastic modulus for bulk graphite (36 GPa) or glassy carbon (29-32 GPa) instead of the intra-plane modulus (1020 GPa). In contrast to as-deposited nano-pillars, calculated Young's moduli for cured structures (40 – 70 GPa) are even higher than for inter-plane tension in bulk graphite. As a result, a second mechanism has to increase Young's modulus which has been found in Pt grain ripening. TEM images in Figure 6-21 (b) demonstrate significantly increased sizes of Pt grains. However, it is not likely that neighboring Pt grains are touching and thus determine elastic properties since studies of nano-crystalline Pt films revealed a decrease of Young's modulus of solely 12 % (140 GPa) compared to bulk Pt[48]. Hence, the elastic properties are still dominated by carbon (graphite) but are further enhanced by influences arising from the Pt nano-particles. Considering our resonance concept, it is obvious that this carbon dominated elasticity of the quasi-1D nano-resonators is inevitable since it provides sufficient amplitudes of oscillation. On the other hand, if the Pt grains would not provide a sufficient electrical conductivity, it would be impossible to excite the resonator via electric fields. As a result it can be stated that the unique composition of this FEBID structures which provide both electrical conductivity and elasticity are the key for quasi-1D resonators.

In order to sum up the experimental results from PGT, we can state that curing considerably increases Young's modulus (Figure 6-27). As-deposited pillars exhibit an elastic modulus which is in the range of weakly bond carbon molecular solids and thus determined exclusively by the carbon phase. After curing Young's modulus is even higher than for pristine graphite considering deformation along the c-axis in the hexagonal lattice. Hence, this increase cannot be explained solely by graphitization into a glassy carbon state but one have to take into account the Pt grain ripening. In terms of resonance frequency, the increase of Young's modulus leads also to a raised point of resonance (Figure 6-22). As a consequence the frequency of application can be tuned over the whole kHz range and deviations of deposited pillars from theoretical prediction (equation (6.7)) can be compensated.

6.9 Including the Nano–Granular Metal-Matrix Structure in Euler-Bernoulli

The previous chapter 6.8 demonstrated that, despite the presence of Pt, the elastic properties of nano-pillars are mainly determined by the carbon matrix. As-deposited pillars consist of rarely linked precursor fragments and mainly sp^2 hybridized carbon. This is in agreement with the observed Young's modulus in the range of 8 – 12 GPa as found for highly defected carbon grain structures[53] or disordered carbon nano-cylinders[52]. The energy provided by impinging electrons leads to the formation of graphitic sheets which increases Young's modulus (Figure 6-24) up to values for glassy carbon (29 - 32 GPa) or inter-plane tension in graphite (36 GPa). However, Young's modulus gathered from experiments and simulations ($\boldsymbol{E_{sim}}$) gets additionally raised by Ostwald ripening of Pt grains as a consequence of atomic Pt dissociated from precursor fragments by post-deposition dissociation processes induced by curing. In order to account for this additional increase and thus for the nano-granular occurrence of Pt a factor $\boldsymbol{c_{ng}}$ has been introduced (section 5.4.2) comparing actual moduli of two-phase PtC-resonators with that of pristine carbon in glassy state ($\boldsymbol{E_{gC}}$)

$$c_{ng} = \frac{E_{sim}}{E_{gC}} \tag{6.8}$$

with a medium value of Young's modulus for glassy carbon (**gC**) basing on literature (29-32 GPa)[46]

$$E_{gC}[GPa] = 30\ [GPa] \tag{6.9}$$

Hence, $\boldsymbol{c_{ng}}$ values greater than unity represent elastic moduli which exceed that for glassy carbon and thus cannot be explained solely by the carbon matrix. Figure 6-28 reveals the evolution of the nano-granular factor with respect to the TET during PGT. As-deposited pillars (TET = 0) exhibit low elastic modulus due to highly defected sp^2 carbon configuration with dissolved or partly attached precursor molecules. In addition, the carbon phase separates Pt grains and acts as a damping material. Curing increases Young's modulus and thus $\boldsymbol{c_{ng}}$ by the formation of locally well-aligned graphitic sheets until a glassy state is established. Simultaneously the migration of atomic Pt released from unattached fragments leads to ripening of Pt nano-particles which reduces the distance between these metal grains. By that, Young's modulus can even exceed values for pristine glassy carbon ($\boldsymbol{c_{ng}}$ > 1) due to the influence of Pt nano-particles. At this point it is important to discuss the sequence of occurring effects. Especially 30 keV pillars reveal elastic moduli far beyond glasslike carbon. From previous studies[33,34] and in particular from electric measurements it is evident that the finalization of precursor dissociation is the predominant effect in early stages of e-beam PGT. Once, the electrons are not consumed by that process the carbon matrix modification overtakes entirely leading to the effects described above. Nevertheless, it is assumed that both processes co-exist at any time but their relative contribution changes.

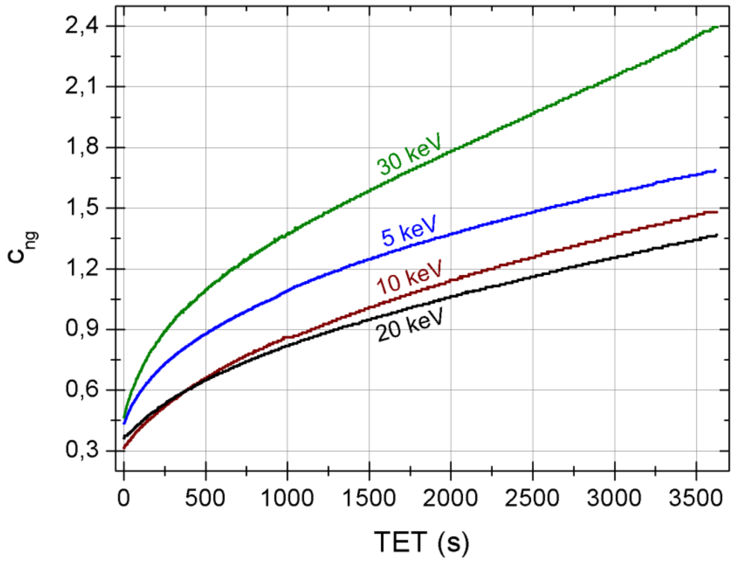

Figure 6-28: Nano-granular constant c_{ng} *during curing process. Whereas* $\boldsymbol{c_{ng}}$ *factor is small for as-deposited pillars (elastic modulus smaller than glassy carbon) it increases during PGT and finally extends the value which can be expected from Young's moduli of pristine carbon in glassy state (*$\boldsymbol{c_{ng}}$*>1).*

6.10 Summary

The resonance frequency of pillars deposited at different PE energies and current as well as at one specific PE energy and varying current was determined by applying an AC field (chapter 6.2). Experimental results reveal a single well-defined peak for 30 keV pillar (cf. Figure 6-29) and superposed resonance oscillations for other PE energies, i.e. 5, 10, and 20 keV. In addition, the geometric dimensions were measured (chapter 6.1) and bending experiments were performed (chapter 6.4). On the basis of the shown deflection with respect to the applied DC voltage Young's modulus ***E*** was calculated via finite element simulations (chapter 6.5). EDX measurements provide information about the chemical composition of the structures (chapter 6.3).

Two distinct tendencies could be derived from the data gathered from the variation of deposition parameters. On the one hand, there is a ***higher dissociation cross section*** at 5 keV / 5 pA due to the lower energy of the PE electrons, confirmed by higher VGRs (cf. chapter 6.1). Hence, the structure contains more Pt and exhibit enhanced stiffness and a comparatively higher resonance frequency. On the other hand, deposition parameters of 30 keV / 21 pA provide a smaller dissociation cross section but a ***larger number of electrons*** due to a higher current which leads to an enhanced Pt content compared to intermediate deposition parameters (10 keV / 7.5 pA and 20 keV / 13 pA).

E-beam post-growth treatment (curing) increases Young's modulus and thus the resonance frequency at simultaneous constant average density via ripening of Pt nano-particles and formation of graphite sheets. This is a key feature to tune the resonance frequency into the desired range. Young's modulus is raised up to 70 GPa and the resonance frequency can be increased by more than 450 kHz after 3600 s of irradiation by the electron beam at 30 keV and 44 pA. Even longer PGT's are expected to shift the modulus to even higher but saturating values which was beyond the scope of the present thesis.

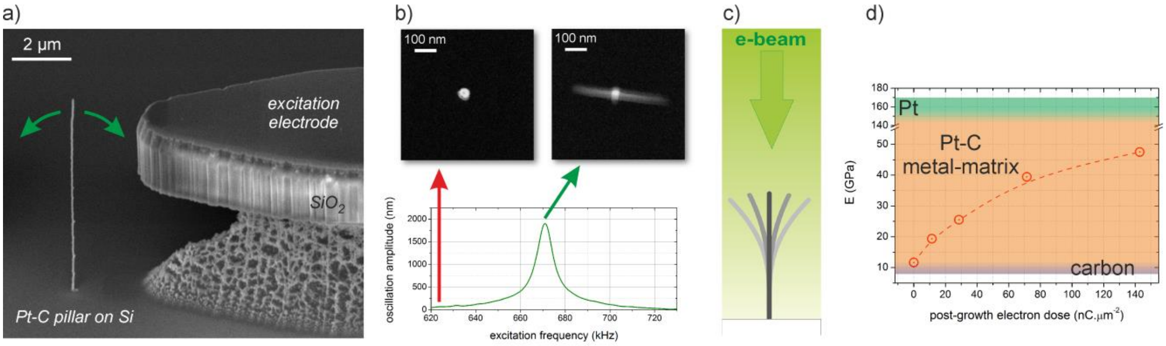

Figure 6-29: AC excitation of quasi-1D nano-resonators (a) and SEM images of pillars on/off resonance with corresponding resonance curve (b). Top view curing (c) considerably increases Young's modulus (d) and enables tuning of the resonance frequency across a wide range.

7 Gas sensing Experiments

Taking advantage of the results from previous experiments we want to introduce the main topic of this thesis: Quasi-1D nano-structures as ultra-sensitive gas sensors. Thorough investigations concerning the influences of deposition parameters on resonance behavior strongly suggest the use of highest primary electron energies and lowest beam current and by that using 30 keV and 21 pA, respectively. Nano-resonators deposited with this set of parameters exhibit one well-defined resonance peaks with most tunable frequencies via e-beam PGT.

7.1 Concept

As described in detail in section 6.2, a quasi-1D pillar (***resonator***) oscillates when an appropriate AC field is applied. The resonance frequency can be tuned to be in the desired range via electron beam curing (cf. chapter 6.8). If gaseous molecules adsorb on the pillar, the resonance frequency is changed (cf. Figure7-1) which is basically described in chapter 2.3. The rate of adsorption on microporous carbon nano-materials can be described by the Dubinin-Rdushkevich equation assuming a Gaussian distribution of the adsorption potential, i.e., the rate of adsorption reveals a maximum and decreases symmetrically around this maximum value:

$$\frac{W}{W_0} = \exp\left[-\left(\frac{RT\ \ln(P_0/P)}{\beta E_0}\right)^2\right] \tag{7-1}$$

$\boldsymbol{W/W_0}$ is the rate of adsorption with the maximum value $\boldsymbol{W_0}$ and the actual adsorption $\boldsymbol{W}$ at a specific pressure $\boldsymbol{P/P_0}$ (P_0 indicates the vapor pressure of the saturated adsorbate). $\boldsymbol{E_0}$ represents the characteristic energy of adsorption and $\boldsymbol{\beta}$ is a material parameter[54]. As the energy of adsorption is determined by the interaction between substrate and the adsorbing molecule, the adsorption rate is different for every molecule. Hence, the amount and sort of adsorbing molecules can theoretically be determined via quantitative analysis of the resonance frequency shift. Additionally, the extreme aspect ratio of the resonator enables to observe a frequency shift even at the adsorption of very few molecules. As the differentiation between gaseous adsorbates can be highly complicated in practice, it might be useful to ensure the specific detection of one type of molecule via chemical modification of the surface. Thus, the presence of one particular type of molecules can be determined with an extreme sensitivity. Making the surface chemically sensitive allows the detection of slightest traces of a particular type of molecules in the ambient air. This is the main advantage of this concept.

In addition, this method allows distinguishing between different forms of adhesive interaction. As physisorption is established via weak van der Waals forces this process is generally reversible. Hence, complete desorption can occur as consequence of a diminishing partial vapor pressure, i.e. a lowered concentration of the gas in the ambient atmosphere. In turn, this results in a shift of the resonance frequency to the initial value. In contrast, if the adsorbate is chemically bonded to the adsorbent, the resonance frequency remains at the changed value even if the gaseous phase of the adsorbate is pumped out e.g. of the vacuum chamber.

In this thesis we basically focus on the proof of concept instead of quantitative analysis of gaseous molecules in the surrounding air.

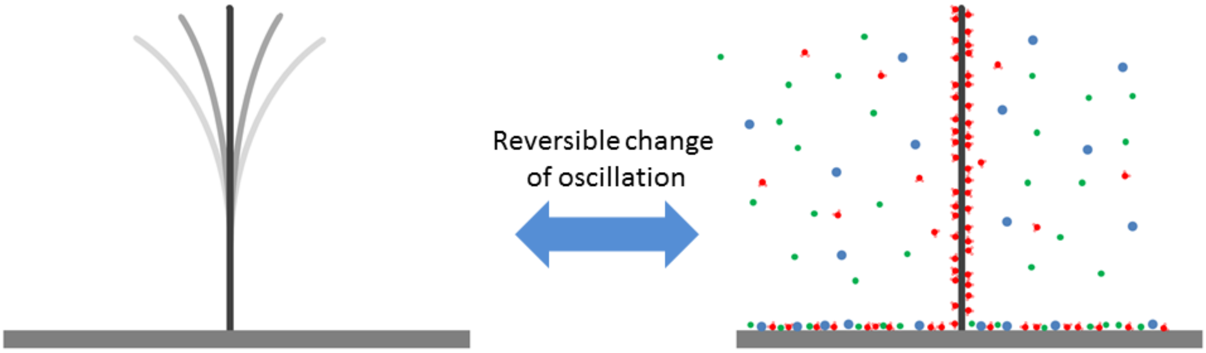

Figure7-1: The adsorption of molecules changes the oscillation behavior, i.e. the resonance frequency. Due to varying adsorption rates the specific and highly sensitive detection of gaseous molecules is possible

7.2 Gas sensing Experiments Using SEM Detection

7.2.1 Experimental Outcome

As described in detail in chapter 4.2, the resonance frequency of a resonator was determined using optical methods (SEM). The resonance peaks were captured and subsequently analyzed via software Tracker®. This procedure was performed at different gas pressures and for varying gases. Previous experiments with gaseous atmospheres and PtC deposits together with chemical considerations suggest the use of the following gases:

1) *Air (water vapor) (multi-component gas)*
2) *Oxygen O_2 (single air component)*
3) *Nitrogen N_2 (single air component)*
4) *Sulfur-hexafluoride SF_6 (assumed as chemisorbed material due to e-beam related dissociation)*

Considering the morphological discussion in chapter 6.8 the resonator consists of a thin carbon surface layer surrounding two phase structure of Pt nano-particles embedded in soft carbon matrix with a high concentration of defects and voids. As a result, these large amounts of defects and voids suggest high rates of adsorption[55]. Purification experiments[56] and according simulations[45] revealed a high gas permittivity in similar nano-structures for water molecules at large pressures. This is supported by a high mobility of water molecules in carbon polymers and a weak interaction in terms of adsorption for Pt (E_a = -0,3 eV/atom)[45]. Thus, water molecules are assumed to diffuse into the resonator. In contrast, oxygen, which is likely to adsorb at Pt (activation energy E_a=-3 eV/atom)[45], remains in regions closer to the surface. However, both gases and also N_2[57] are likely to adsorb on carbon nano-structures at considerable rates. According to atomistic considerations, the highest rates of adsorption on carbonic adsorbents can be expected for H_2O. This was actually revealed for sp^2-hybridized carbon nano-tubes[58]. The fourth gas (SF_6) was chosen with the intention to investigate the influences of molecules containing highly reactive fluoride.

Hence, isolated measurements were performed for the four different gases. The gas of interest was released into the vacuum chamber until the pressure rose above $60 \cdot 10^{-6}$ mbar and two measurements for one type of gas were performed. The use of a Kleindiek® micromanipulator / GIS combination guarantees a local pressure in the area of interest which is much higher than the average pressure in the vacuum chamber (cf. chapter 4.2.3). Afterwards the inlet valve was closed and the specimen chamber was evacuated to at least $4 \cdot 10^{-6}$ mbar (referred to as measurement 'vacuum'). Thus, the difference in the average pressure was more than one order of magnitude; the local pressure difference in the ambient atmosphere around the resonators tends to be much higher. Figure 7-2 illustrates the global pressure in the vacuum chamber at the corresponding measurement. Measurements at equal atmospheres, e.g. vacuum 1 & 2 or air 1 & 2, were separated by approximately one minute. The time between measurements performed at different atmospheres, i.e. air 2 and vacuum 3, is about 10 minutes due to careful adjustment of the gas inlet and pumping out of the gaseous adsorbates respectively.

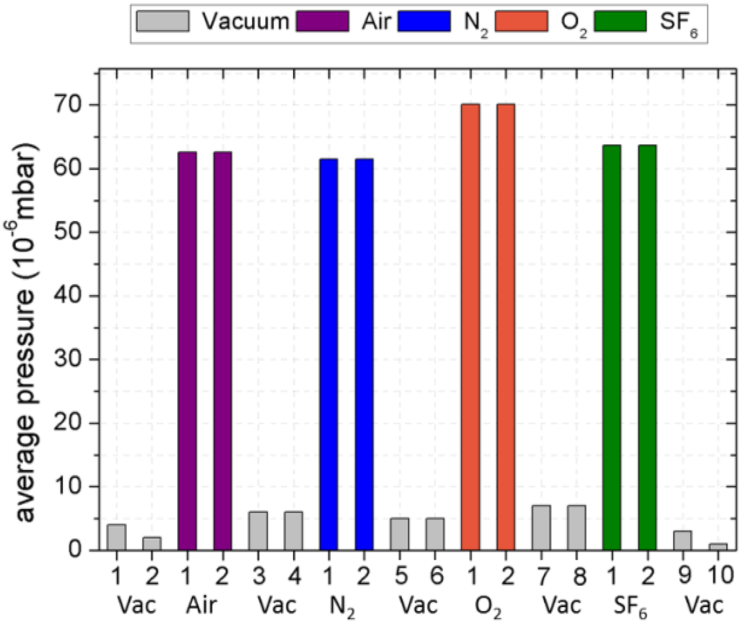

Figure 7-2: Average pressure inside the vacuum chamber at the corresponding measurements. Please note that the local pressure around the resonator was much higher due to the use of a annular nozzle on Kleindiek® GIS.

As mentioned above, two measurements were performed per ambient atmosphere. Each of them provides two resonance curves as two successive frequency sweeps around the resonance frequency were tracked: one up sweep and one down sweep. The resonator's oscillation was captured via SEM and analyzed by 'Tracker® 4.84' as described in chapter 4.2.3.

Afterwards, an internal Origin® 8.5 routine ('PSD Voigt 1') performed a fit according to:

$$y = y_0 + A \cdot \left[\frac{2\mu}{\pi} \frac{w_L}{4(x-x_c)^2 + {w_L}^2} + (1-\mu) \sqrt{\frac{4 \cdot \ln(2)}{w_G \sqrt{\pi}}} \cdot e^{-\frac{4 \cdot \ln(2)}{{w_G}^2}(x-x_C)^2} \right] \quad (7\text{-}2)$$

This formula might appear quite complicated but it is essential that the peaks (i.e. the resonance frequency) of both the real and the fitted curve are in strict compliance.

Figure 7-3 illustrates representative resonance peaks for up AND down sweeps in black and red, respectively. It is clearly evident that successive resonance curves are shifted by a small amount. This arises from curing effects (cf. chapter 6.8). The resonance frequency of one measurement, i.e. for one upsweep and one sweep down, was calculated as maximum of the arithmetic mean of these two curves. However, due to the arising frequency shift caused by PGT a background shift had to be extracted and subsequently drawn off. As a result, the derived changes of the resonance frequency are solely caused by the adsorption of particular gaseous molecules and not by curing effects. Although the PGT induced frequency increase saturates for long exposure times, as shown in Figure 6-23, it is permissive to assume a linear frequency shift caused by PGT for sweeps around the resonance frequency since the exposure times per measurement are shorter than approximately 30 s compared to about 3600 s for complete curing (cf. Figure 6-23).

Hence, the use of frequencies determined by 'vacuum' experiments and therefore without significant adsorption of one type of gaseous molecules allows the determination of a linear increase which is exclusively caused by curing. As the PGT induced shift of the resonance frequency takes place for both, measurements with and without adsorption of one type of gaseous molecules, subtracting this shift discloses the effects of adsorption on the resonance frequency of quasi-1D nano-resonators.

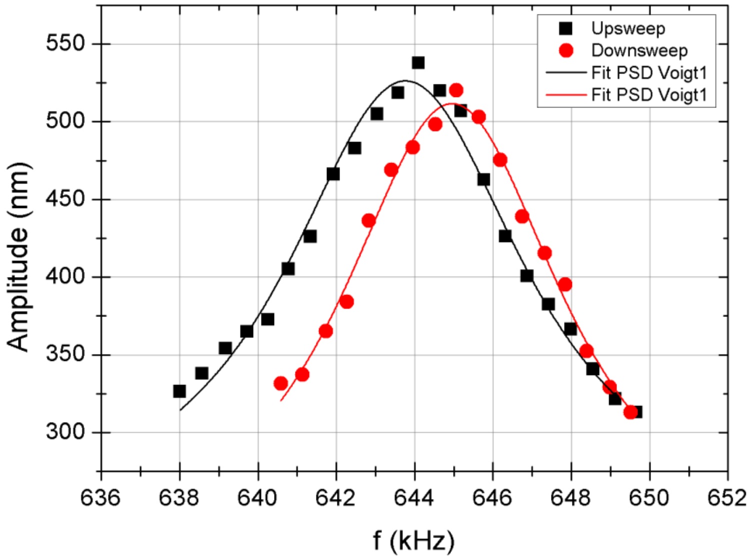

Figure 7-3: Up- and down-sweep around the resonance peak. The scatter graphs reveal the pillar's amplitude gathered from captured movies via video analyzing software Tracker®, the line plots show the corresponding fits performed with Origin®.

Figure 7-4 representatively reveals the arithmetic mean of up-and down-sweep at two different atmospheres: The black line indicates the resonance peak for closed valves and thus at the minimal pressure accessible by this vacuum system; the red resonance peak was measured with opened valve leading to the gas inlet of ambient air. The linear background shift has been drawn off. Hence, the visible shift of the resonance frequency is solely induced by adsorption of molecules from the gaseous phase and follow-up processes such as diffusion.

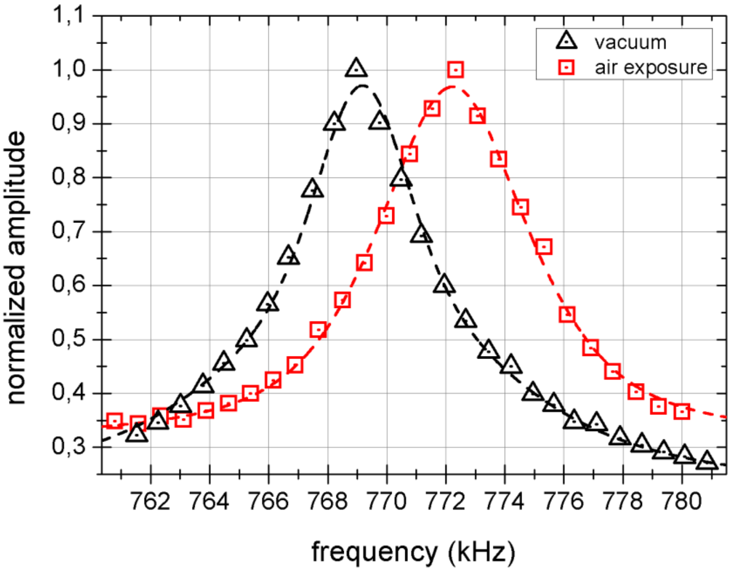

Figure 7-4: Resonance frequency of successive measurements. Black scatters indicate a 'vacuum' experiment, where the resonance frequency was determined for closed inlet valves. Measuring the resonance peak at the presence of ambient air (red) reveals a significant increase of the resonance frequency. Please note that the frequency increase caused by curing has already been drawn off.

Figure 7-5 illustrates the relative frequency shift caused by adsorption of the respective type of gas. Two interesting features can be derived:

1) ***The amount of frequency shift depends on the gas type, i.e. the adsorption rate***
2) ***The adsorption can be reversible (physisorption) and irreversible (chemisorption)***

These two statements are undoubtedly some of the key findings of this thesis. If air (purple) is let into the chamber, a comparatively large shift of the resonance frequency of about + 3 kHz occurs. This large shift is equivalent to a high rate of adsorption, probably caused by gaseous H_2O which is likely to adsorb on carbon[58]. After closing the velvet and pumping down the specimen chamber the resonance frequency falls again to its initial value. This is the ***proof of reversibility*** of the adsorption process and thus of a physisorbing character of the adsorption process. One drawback of the usage of air is its composition: Air consists of many different types of molecules. In order to prove the argument that the frequency shift was mainly determined by water vapor the main components, nitrogen (78.1 %) and oxygen (20.95 %), were used for following experiments. In addition, it is possible to receive better insight in the adsorption rates of the specific gases occurring in air. Figure 7-5 confirms that the increase in frequency for N_2 (blue) and O_2 (orange) is significantly lower than the one for water containing air. Hence, the remarkable rise of the resonance frequency at the adsorption of air is likely to originate from water. In addition, the adsorption of N and O was also reversible because the resonance frequency fell off again when the gas velvet was closed and the chamber pumped down again.

Sulfur hexafluoride (olive) was used for the last gas experiment, a gaseous dielectric. The shift of the resonance frequency is about + 3 kHz and therefore similar to the value found for air. This indicates a high rate of adsorption. However, this adsorption process was not reversible since the resonance frequency did not return to its initial value at the next 'vacuum' measurement without inlet of SF_6 gas (light green and grey striped). The gas molecules, which caused the increase of the resonance frequency did obviously not desorb after the valve was closed, but they were still strongly bound to the resonator. This is a sign of a chemical bond induced by SF_6 dissociation generated by the extreme power of the impinging electrons.

This assumption has been verified via EDX analyses. Comparing EDX scans of the resonator exposed to SF_6 as well as the e-beam and one of an area which was not affected by impinging 30 keV electrons reveals significant differences in the appearance of Fluor (Figure 7-6). While no evidence of the presence of Fluor is found on the substrate, it can be definitely detected on the resonator. Hence, SF_6 desorbs if it is not exposed to high energy PE electrons but undergoes a chemical reaction with the PtC resonator if SF_6 is dissociated by impinging electrons.

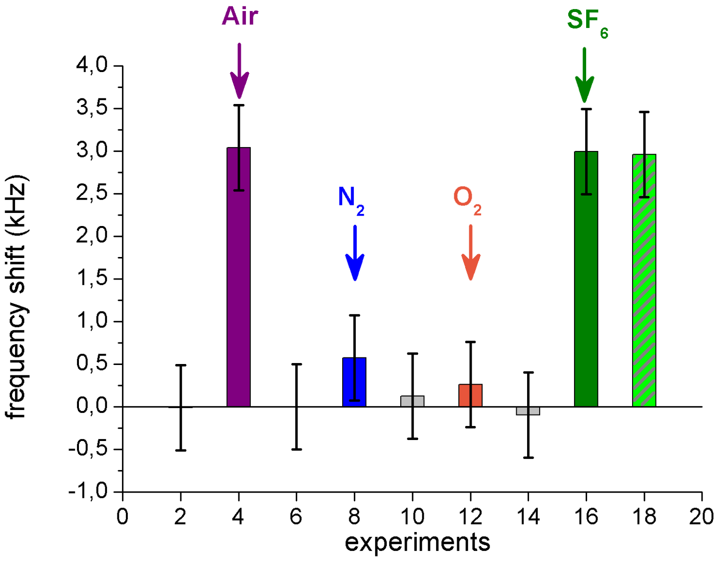

Figure 7-5: Additional frequency shift, which is not caused by e-beam curing. As one can see, the shift depends on the gas type. Grey bars indicate 'vacuum' experiments.

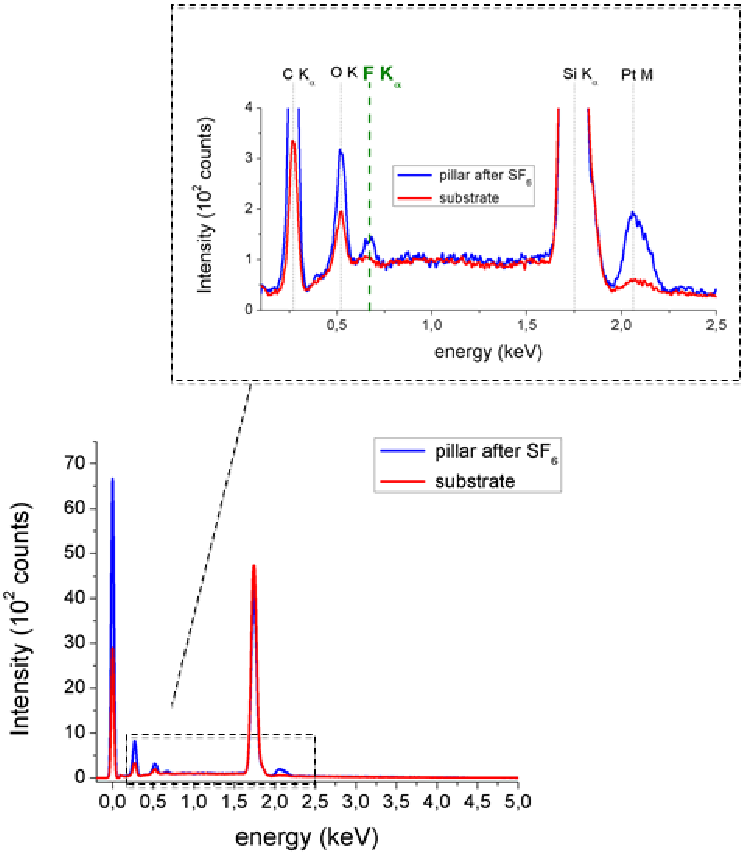

Figure 7-6: EDX scans of the pillar (blue), which was irradiated by the e-beam at the presence of SF6 and the substrate, which was not bombarded by electrons. The zoomed area reveals undoubtedly the presence of fluoride (emphasized by a green line) on the pillar.

In order to conclude these semi-quantitative analyses we can state that the presence of gas molecules changes the resonance frequency by a few kHz and can be detected highly sensitively. What is more, the adsorption is reversible for many types of molecules but can also be irreversible. In case of reversibility the resonance frequency of the pillar drops back to the initial value, if the gas is removed from the ambient atmosphere. In contrast, if the molecules are stuck by a chemical bond the resonance frequency remains at the enhanced value, even if the gaseous molecules are pumped out of the chamber. Hence, this setup enables additionally the ability to distinguish between physisoption and chemisorption. However, a more thorough discussion concerning the causes of this frequency is required and shall be provided in the following chapter.

7.2.2 Possible Causes of Frequency Increases of Nano-Resonators at Gaseous Adsorption

It is useful to start with the chemisorbed SF_6 as the chemical reaction leads to strongly bound fluoride on the resonator. According to high resolution TEM images, the resonator consists of Pt nano-particles spatially distributed in a carbon matrix. This carbon matrix exhibits a high grade of disorder and is transformed into a glassy carbon state by PGT. The gas permeability for glass-like carbon is $10^{-11} - 10^{-12}$ cm/s.[59] Simulations of deposited nano-structures consisting of such PtC system suggest a permeability coefficient which is in perfect agreement with this value[45]. Hence, the carbon matrix can be treated as glass-like carbon, also in terms of molecular migration. Considering Euler-Bernoulli's equation adjusted to quasi-1D resonators (6.7) the rise in frequency can stem from several parameters. Since a decrease in height can be neglected as well as a reduced density caused by gas adsorption, two possible cases can lead to an increased resonance frequency:

1) ***An increase in Young's modulus***
2) ***An enhanced width of the resonator***

The used resonator was deposited with 30 keV and 21 pA and a TET of 500 s. This suggests a height of about (5.0 ± 0.2) µm. The resonance frequency was about 810 kHz at SF_6 adsorption experiments. This frequency was already enhanced due to trials prior to actual gas adsorption measurements. The initial as-deposited frequency of the resonators was 609 kHz. Comparing this with the curing curve of a 30 keV pillar, the frequency shift corresponds to a TET of about 760 s (< 13 min) and an elastic modulus of about 37 GPa. Assuming a density estimated by linear regression of EDX results concerning the Pt content (equation (6.3)) a frequency shift induced by SF_6 adsorption corresponds either to an increase of Young's modulus of 0,2 – 0,4 GPa or an increase in diameter of about 0.2 - 0.3 nm. Typical bond lengths between 100 – 200 pm are in approximate compliance with that estimated increase in diameter. The reaction of dissociated fluoride with the outer carbon layer on the pillar's surface is likely to take place and then leads to the formation of tetra-fluormethane. Thus, the chemisorption of a single monolayer of SF_6 leading to tetra-fluormethane can partly induce this considerably shift in the resonator's frequency. However, this is not a completely satisfying explanation. Occasional formation of SF_6 dimers on secondary sites may additionally increase the resonators diameter. The distance between the SF_5 anions in a SF_6 dimer has been estimated with 620 pm[60]. Thus, this may induce the additional increase of the resonance frequency. However, as the presence of sulfur was not confirmed by EDX analysis, the formation of dimers could not have taken place in a considerable extent. ***Hence, as an essential outcome of this study it can be derived, that a second mechanism is involved, which raises the resonance frequencies***. Considering a change in the carbon configuration via chemical reaction to fluorhexamethane, the former sp^2 hybridized carbon molecules on the surface layer are likely to become sp^3 hybridized due to the extremely large electro negativity of fluoride. According to literature, Young's modulus increases with the fraction of sp^3 hybridized atoms[50]. As the increase of Young's modulus, which is necessary for a 3 kHz shift of the considered resonator's frequency, is that low (1 %), this possibility should be taken into account as well.

Figure 7-7 reveals the influences of a slight increase of Young's modulus from 37 GPa to 37.3 GPa as well as an increase of the diameter from 73 nm to 73.3 nm. The calculated resonance frequency of the considered resonator, based on the assumptions of a constant average density and height respectively, is considerably changed. Hence, slight increases of both quantities lead to a significantly enhanced resonance frequency.

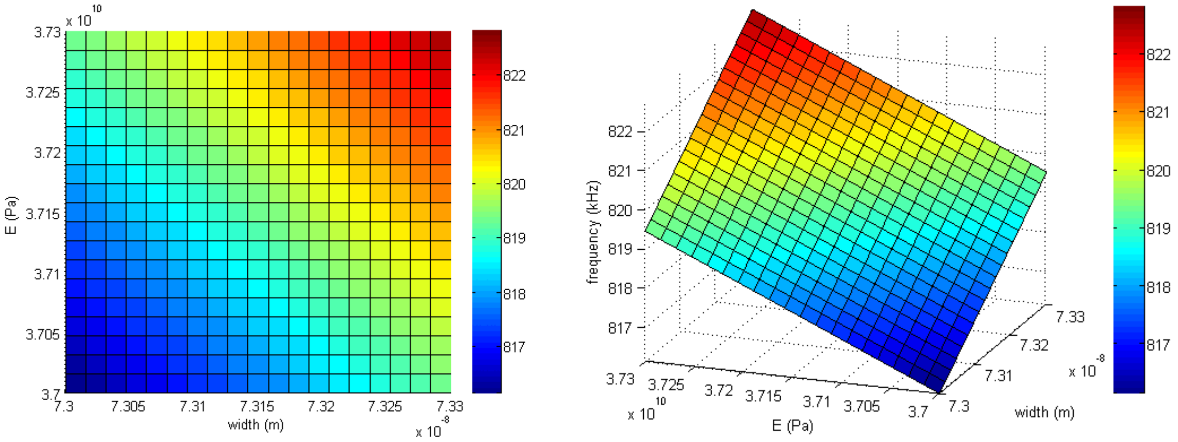

Figure 7-7: Influences of an increase of Young's modulus and the resonator's diameter up to 0,3 GPa and 0,3 nm respectively. Simulations demonstrate that these small variations shift the resonance frequency about 3 kHz each.

Before taking diffusion into account it shall be noted, that the changing ambient pressure as consequence of the gas injection has been considered. However, its negligence appears to be appropriate because of three reasons. At first, gas detection experiments are still performed at rather low pressure, even if the pressure is significantly increased compared to 'vacuum' experiments. Therefore, the electromagnetic force is likely to act comparatively much stronger than friction resistance impedes an oscillation at such low pressures. Secondly, a rising ambient pressure is supposed to cause damping of the oscillation which usually decreases the frequency. In fact, the resonance frequency was increased by gas injection. The third and probably most convincing reason opposing the theory that the influence of the ambient pressure on the oscillation dominates over adsorption effects is the variety of the experimentally observed frequency increases, which depends on the absorbate. While the pressure was increased by a similar amount for air, O_2, N_2 and SF_6, the according increase of the resonance frequency was remarkably different. Therefore, the influence of the ambient pressure appears to be negligible when using similar pressures but different gases. At least, it is small compared to the effects of adsorption.

In the discussion above, diffusion inside the structure was neglected in a first approximation for chemisorbed SF_6. This is not permissible for H_2O, as it is well known from experiments[56] and simulations[45] that gaseous water diffuses deeply inside the structure. In addition, the permeability constant is typically larger by two orders of magnitude compared to pure O_2 in many polymers[45].

Assuming constant outer dimensions of the resonator the diffusion of H_2O inside the carbon matrix leads to an increase in the resonator's density. This, in turn, decreases the resonance frequency (equation (5.13)). If the entire matrix is filled with gaseous water at a density of 0,035 g/cm^3, the resonance frequency becomes decreased by about 2.5 kHz (green in Figure 7-8, top). However, experiments revealed a total increase of resonance frequency in the presence of ambient air and therefore gaseous H_2O of about 3 kHz (Figure 7-5). Apart from this decreasing trend there has to be a compensating component increasing the resonance frequency (red triangles in Figure 7-5). As mentioned before, this can be caused by an increase of the resonator's diameter (bottom left) up to 0.65 nm (~1 %) or an increase of Young's modulus of about 0.45 GPa (~1 %) (bottom right). Considering the magnitudes of the increases in both cases, it is evident that a definite explanation cannot be found. An average increase in diameter of 0.65 nm over time may occur solely by physisorption. However, considering average bond lengths a value of 650 pm seems to appear quite high. In contrast, an increase of Young's modulus by a high amount of diffused H_2O is rather imaginable. On the contrary, the observed frequency shift (+3 kHz) was reversible which definitely indicates that neither adsorbed nor diffused H_2O molecules were chemically bound. As a consequence it has to be doubted that H_2O can increase the elastic properties of carbon significantly without a strong chemical interaction. Overall, it is most probable that the observed total increase is caused by both mechanisms: ***1)*** an increase in the resonator's diameter due to physisorption, and ***2)*** a rise in Young's modulus induced by water diffusion into the deposit.

However, it is still to mention that these estimations base on the assumption that water diffusion inside the resonator increases only the density while outer geometries remain unaffected. Enhanced diameters were assumed to be caused solely by adsorption. If the diffusion of H_2O molecules swells the resonator, the system can only be simulated iteratively which is far beyond the scope of this thesis. In fact, the actual mechanisms are not identified, but a present topic of discussion. At this point it should be mentioned that these findings, although not definite, are absolutely essential for further steps as they reveal possible effects which could not be extracted in the past.

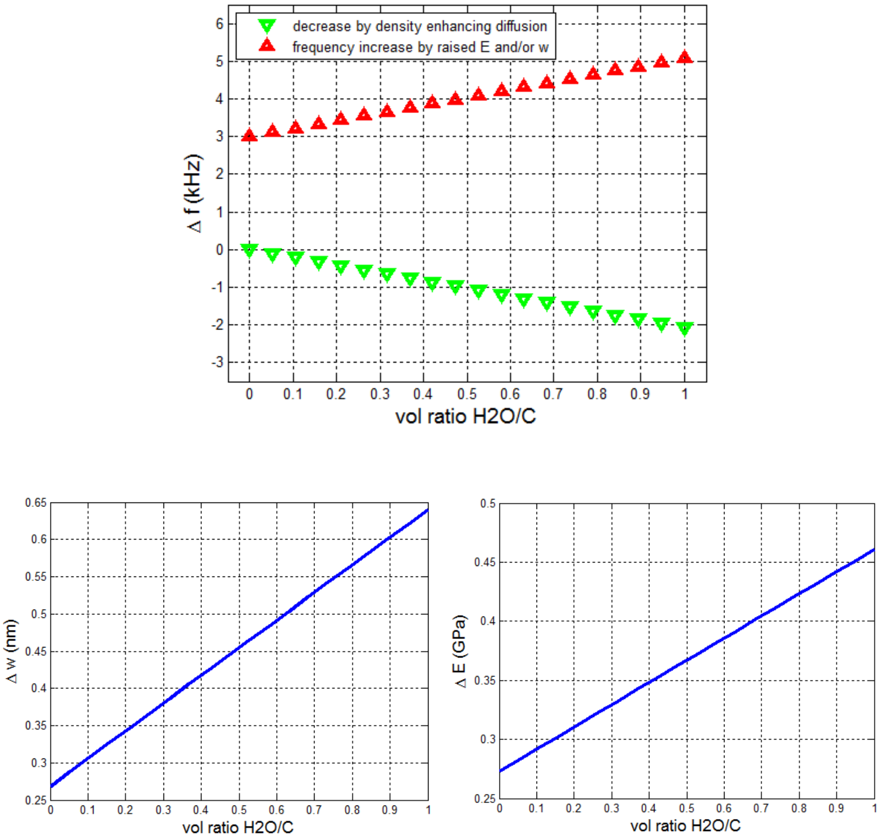

Figure 7-8: Decrease of the resonance frequency (green) by additional occupation of the carbon volume by water vapor at a gas pressure of 0,035 g/cm^3 (a). This decrease has to be compensated (red) to gain a total increase of 3 kHz which can be established by an increased in width up to 0,65 nm (bottom left) or an increase in Young's modulus up to 0,45 GPa (bottom right).

Finally it can be said that the proof of the gas sensing concept has been provided, although slightly different as initially thought (cf. chapter 2.3). The presence of various kinds of molecules leads to a characteristic increase of the resonance frequency, which is reversible for physisorbed gases. In case of SF_6 the frequency shift was irreversible which indicates chemisorption. This was confirmed via EDX analyses. Hence, it is possible to distinguish between these types of adsorption.

Quantitative considerations were restricted due to missing and barely accessible information about very local pressures in the vacuum chamber. However, it can be stated that the observed rise of the resonance frequency is probably caused by both an increase of the resonator's diameter due to adsorption as well as an enhanced elastic moduli due to diffusion inside the structure. This is in accordance to the high permeability constant of H_2O as the resonance frequency shift was much higher for water (3 kHz) than for N_2 and O_2(<1 kHz). Chemisorption of SF_6 caused also a high increase of approximately 3 kHz. This irreversible shift can be induced by a changed carbon configuration towards sp^3-hybridized carbon atoms due to chemical bonding with dissociated Fluoride.

Considering future strategies, it is evident that more experiments have to be performed at highly defined partial pressures to gather a deeper insight in the dynamics coming along with gas adsorption and/or diffusion. In addition, different adsorbates should be avoided due to the highly sophisticated mechanisms related to gaseous adsorption. In this case, functionalization of surfaces is a promising strategy for further experiments in order to strongly promote the adsorption of one specific kind of molecule.

In addition, the detection method using SEM keeps this method far from any industrial application. Thus, a different approach has to be considered, which is described in the following chapter.

7.3 External Read-Out of the Resonance Behavior

The e-beam causes undesired chemical and structural changes to the resonator and thereby make gas detection more complicated. Therefore it is essential to find another measurement method which does not or at most slightly affect the pillar itself. It is of high importance that the measuring process MUST NOT cause a shift of the resonance frequency.

As it was essential to know the material constraints for these kinds of resonators, oscillation tests were performed with resonators deposited on different materials: Au (metal), Si (semiconductor), SiO_2 (insulator), as well as with pillars mounted on other deposits. Several test electrodes were fabricated by ion milling. An oscillation could be generated on all kinds of materials (test structures emphasized with green lines in Figure 7-9). Resonators were deposited on SiO_2, on a milled square to reach the Si substrate (a) as well as on a square which was omitted from milling process in order to maintain the Au cover (c).

7.3.1 LCR Circuits

A first try was performed via the LCR meter Aligent E4980A. The pillar represents a capacity due to the nano-granular structure. The space between the counter electrode and the pillar is a dynamic inductivity, which is changed at the point of resonance due to the changed distance between them as a consequence of mechanical oscillation. In addition, there is the capacitance of the electrode itself, which is connected in parallel.

In theory, the phase φ between voltage and current exhibits two zero crossings in the first harmonic for an equivalent circuit: at the resonance frequency f_r and the anti-resonance frequency f_a. Between these frequencies the system becomes inductive. Outside this frequency range, a capacitive behavior is revealed with a negative phase. In practice, this theoretical behavior with respect to the frequency is superimposed by a parasitic capacitance, which rises linearly with the frequency.

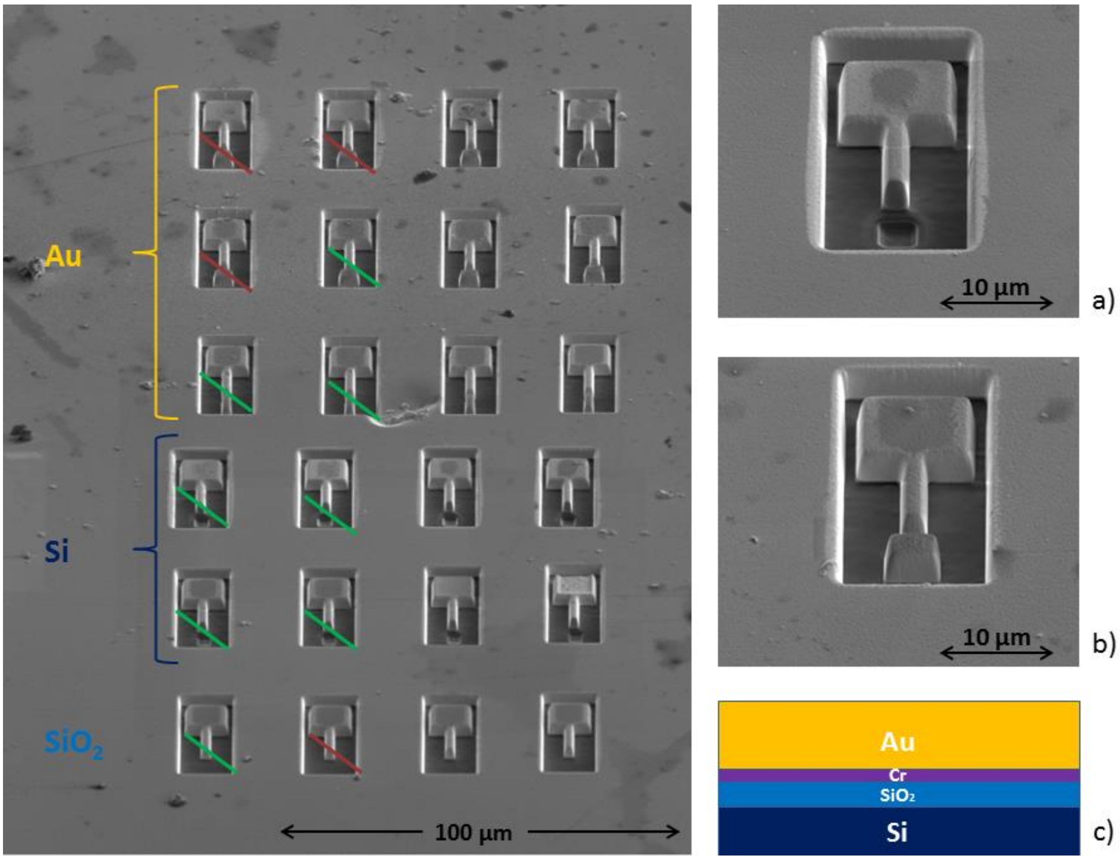

Figure 7-9: Oscillation tests of pillars on different materials (main picture). Green lines indicate successfully initialized oscillations. The pictures on the right hand side reveal electrodes for tests on Si (a), on Au (b) and, again, the composition of the sample (c).

Unfortunately, neither a zero crossings of the phase, nor the reactance at the resonance frequency was observed for free-standing pillars. The situation was different when the pillar touched on the counter electrode, which resulted in a physical connection between counter electrode, pillar and substrate. The phase became zero at one point, but the pillar did not reveal any visible mechanical oscillation, as it was touching the counter electrode. Hence, this kind of electrical readout is inapplicable for a gas sensing system since only a mechanical oscillation of the pillar may be changed by adsorbed molecules. Better results for this method can be derived from literature[22].

7.3.2 Electrical Read-Out via Current Measurements

A more promising approach was to mount an oscillating structure on a current-carrying connection. The oscillation should influence the current, which can easily be detected using a sensitive ampere meter. The idea behind this concept builds upon the unique nano-granular structure. A displacement of the deposit leads to a changed distance between the conductive Pt grains. This is known to take place in a strongly non-linear fashion[5]. It is assumed to affect the current through the structure when the resonator oscillates and Pt grains get compressed during oscillation. The exact architectures (tripod and lambda structures) and its results are discussed in the following chapters.

7.3.2.1 Tripod Structures

A tripod structure was chosen for the connecting wires, since three branches fix the base of the structure. As a result, the top of the oscillating pillar shows maximum deflection. Using a pillar on a single branch between the electrodes would lead to a compensating motion of the single wire. Tripods are always deposited between two conducting and one insulated electrodes with a pillar, i.e. resonator in the center. The branches are of an equal length of 2 – 2.5 µm depending on the longest distance between the electrodes. Further information can be derived from chapter 4.3.2.1.

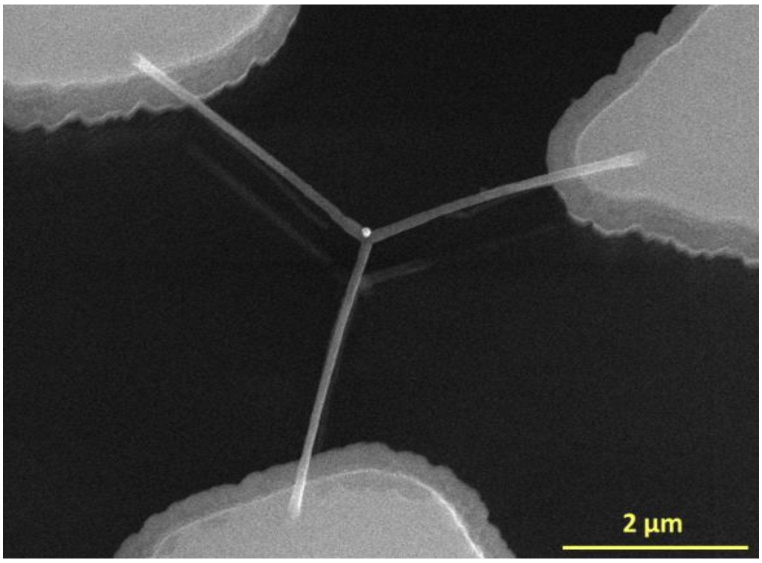

Figure 7-10: Test structures with one insulated electrodes and two connected to the conducting paths. The Tripod connects two conducting electrodes (up and down) and one insulated electrode (upper right corner). The pillar is situated in the center.

As a first step, the electrical conductivity has to be investigated. The insulated electrode was connected via a 3-axes Omniprobe® micromanipulator which consists of a tungsten tip, movable in all directions. The high level DC voltage was applied to the insulated electrode and one conducting electrode. The residual electrode was put on ground potential. The current measurements were performed with a Keithley® Picoammeter 6485. A Keithley® voltage source 230 was used for the voltage supply. All untreated tripods samples were insulating. Even a voltage of 20 V did not lead to any current. However, curing with 30 keV enables a current in the nA-range. Due to the PGT induced processes described in chapter 6.8 we gain two major benefits from this curing: A sufficient ***current*** flow through the deposit and an increased ***mechanical stability***. The latter is important to obtain reasonable oscillations of the resonator on top. A light “shadow” of the tripod structure between the electrodes is visible on the SiO_2 ground beneath (cf. Figure 7-10). This originates from transmitted electrons leading to deposits at the bottom area of the substrate and therefore does not belong to the real tripod-bridge. This side-effect is inevitable as the tripod is deposited as a bridge between the electrodes, ergo 4 – 5 µm above the substrate. However, the insulating character of re-deposits was proofed so that it appears not to be a problem for our measurements.

The current extend through the tripod induced by PGT is determined by the e-beam current and the exposure time. What is more, the current rises exponentially with respect to the applied voltage which agrees with current related experiments. As the conductivity is mainly determined by Pt grains isolated from each other by highly disordered and thus non-conducting carbon, the charge transport is caused by tunneling in the correlated variable range hopping regime[32]. As hopping transport is typically described by an exponential law, the results given in Figure 7-11 are consistent. It shows the average values of current measurements (500 data points) at a certain voltage for different tripod structures. As one can see the current could be significantly increased by curing. Figure 7-12 reveals representative measurements on a tripod structure (left). At least 500 data points were used for one measurement. As one can see, the current becomes unstable, if it gets too high. This is also visible at the standard deviation (right). In order to guarantee the highest possible stability and simultaneously a sufficient strength, currents between 2 - 10 nA ought to be used.

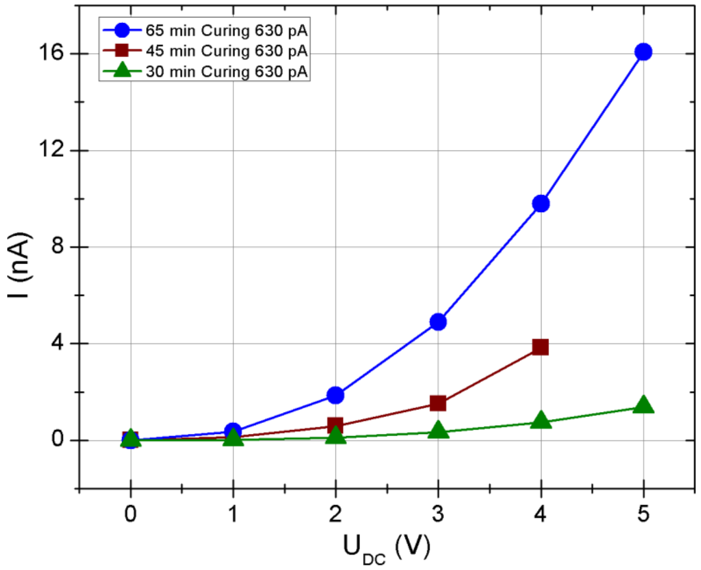

Figure 7-11: Mean current of 500 data points for tripod structures treated by the e-beam at 30 keV and different currents and/or for varying durations.

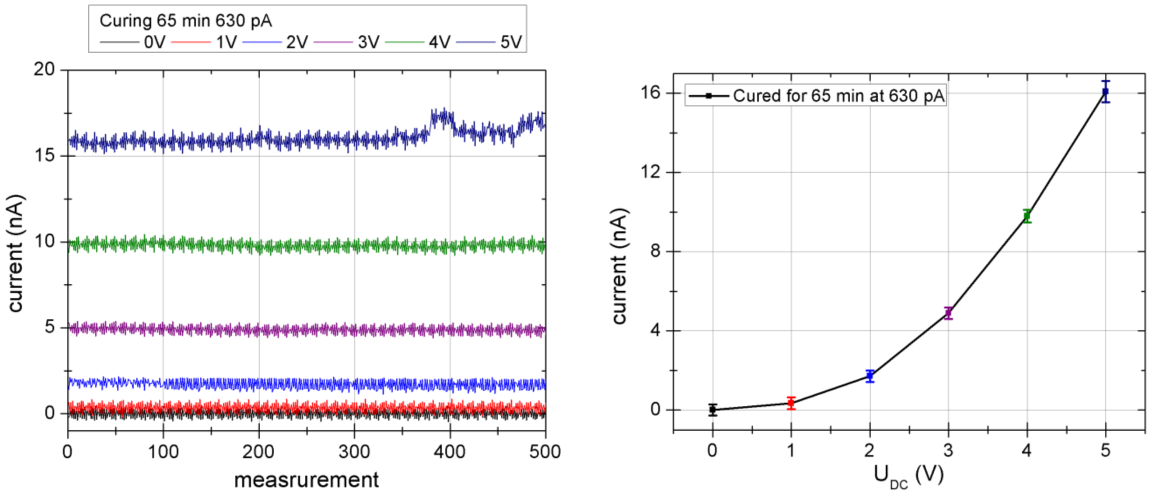

Figure 7-12: Raw data of current measurements (left) and mean values including standard deviations at varying DC voltages for a tripod with branches of 2,5 µm in length. Currents above 10 nA reduces the stability and lead to higher standard deviations. The structure was cured 65 min at 30 keV and 630 pA.

Although it is possible to force an electric current through the structures, the deposits are not really good conductors. As a result, charging occurs, e.g. if the structure is exposed to the e-beam. This has already been observed at deflection experiments (cf. Figure 6-16). This becomes obvious when considering Figure 7-13. The left plot reveals successive current measurements at 0, 1, 2 and 3 V (upsweep) and a downsweep from 2 to 0 V. As one can see, the average current with respect to a specific voltage is higher at the downsweep. This might have two possible reasons: *(1) curing of the structures via current* or *(2) charging of the deposits*. The first one has to increase the current continuously. Charging is equivalent to local fields arising from trapped charge carriers in the low-electron deposit. Hence, it is likely to relax after some time. This was checked by a second measurement, using a kind of “reset-measurement” at an applied voltage of 0 V between two successive current measurements. As a benefit of this sequence, the Picoammeter 6485® enables the function ‘zero check’ between measurements. This function reconfigures the amplifier to shunt the input signal to low. As a result, no current can flow in the circuit. A “measurement” at 0 V disables zero check and leads to a balanced charge in the deposit. As a result, up- and down-sweeps are in perfect agreement (Figure 7-13, right). Thus, charging of PtC nano-structures can be induced by both impinging electrons from the e-beam and charge carriers injected from contact lines.

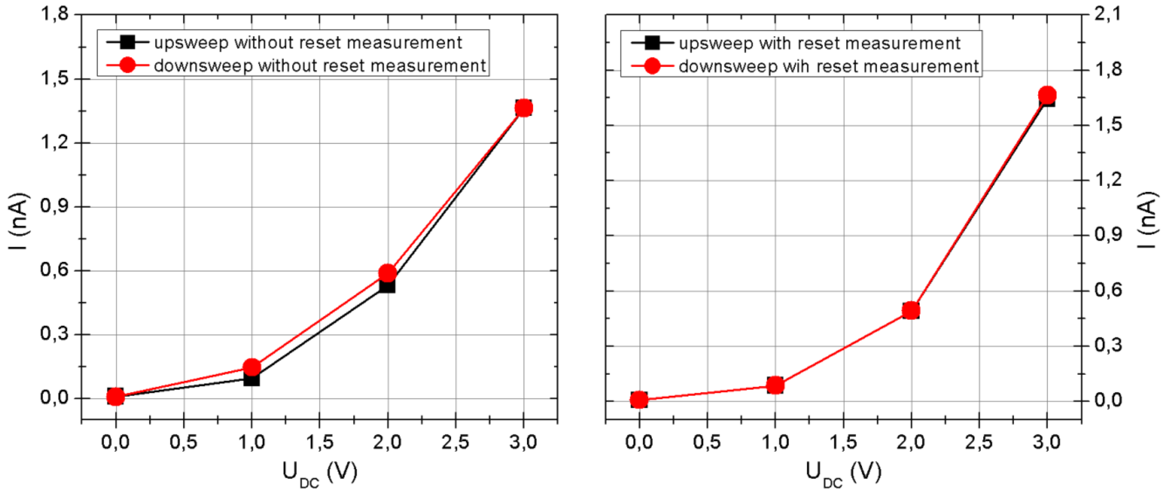

Figure 7-13: Up- and down-sweep with (right) and without (left) a reset measurement (= 0 V measurement to allow relaxation of local fields induced by charging) between successive U-I-measurements. Without reset measurement the down-sweep current is increased due to charging from the injection of charge carriers from the electrodes into the low-conductive deposit.

In the next step the pillar was tried to be put into resoncance as described in chapter 4.3.2.1. In order to achieve that, an Omniprobe® micromanipulator and a Kleindiek® gas injection system equipped with a Omniprobe® tungsten tip instead of a nozzle was used for connection of the insulated electrodes (Figure 7-14). In this setup, the left tip connected to the tripod was set to a high voltage level and the right tip served as exciting electrode. As a result, a DC current was established through the tripod structure. The pillar on top of the tripod ought to change this current, if it is put in resonance by the AC voltage applied by the second tip. ***Unfortunately, the resonator showed no mechanical response to the applied AC field***. In addition, the approach of the tips to the electrode was highly sophisticated (Figure 7-14, left), as both needles need to be aligned highly accurately. Detailed experiments with gradually decreasing base widths of the tripods revealed a damping behavior for the used dimensions, which entirely suppressed the resonator oscillation. In order to overcome this limitation, the tripod architecture was transferred to different samples with four parallel conductive lines (cf. chapter 4.3.2.2).

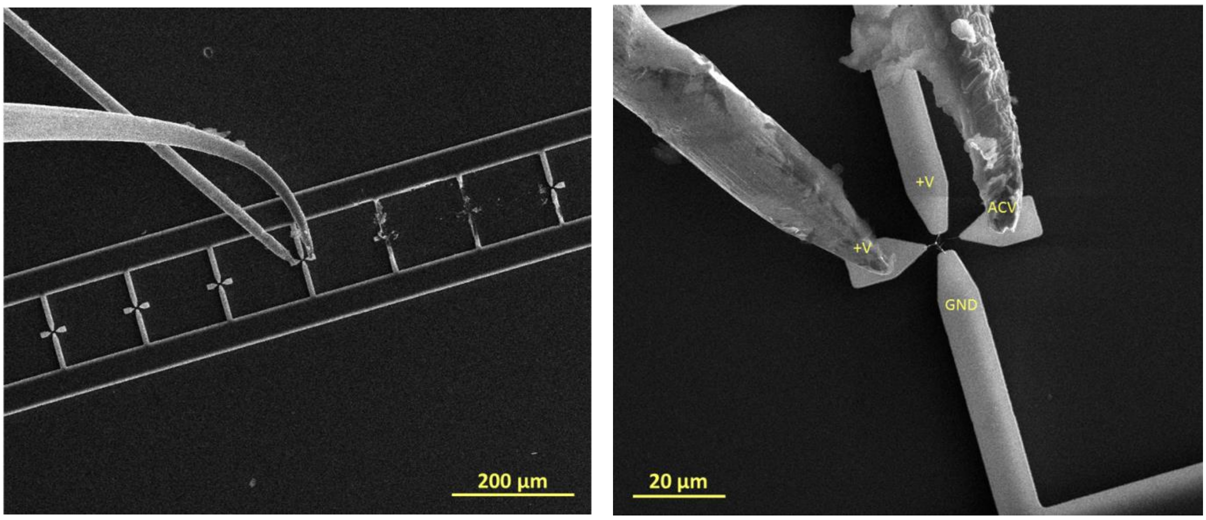

Figure 7-14: Connection of the insulated elecrodes via Omniprobe micromanipulator and Kleindiek® GIS. The left image reveals the difficult approach, in the right image one can see the connected tips and the tripod with the resonator (white point in the center) in between.

Therefore, tripods were deposited with two branches on one line, the high level, and one branch was connected to GND (Figure 7-14, left), again in order to establish a DC current over the tripod. As the distance between these lines is shorter than those between the electrodes in the previously used substrates, the deposited tripod structures are smaller. Beside the elimination of the damping character, this approach has the advantage of lower electric resistances. The approached micromanipulator was used for the excitation about 3 µm apart from the resonator along various directions. The Kleindiek® micromanipulator was not needed in this experimental setup, which is a considerable benefit compared to etching samples, as mentioned above. Indeed, an oscillation could be induced for several pillars deposited with 30 keV / 21 pA and 5 keV / 5 pA. Although the resonators revealed massive amplitudes at oscillation, as shown in Figure 7-14 (right), no clear response of the electric current through the tripod base branches could be found. This allows the conclusion that the variation of the grain-to-grain distance as essential element for changing the electric conductivity does not occur to the necessary extend in the interconnection region at the tripod center. Therefore, an alternative architecture was defined and tested as described in detail in the following.

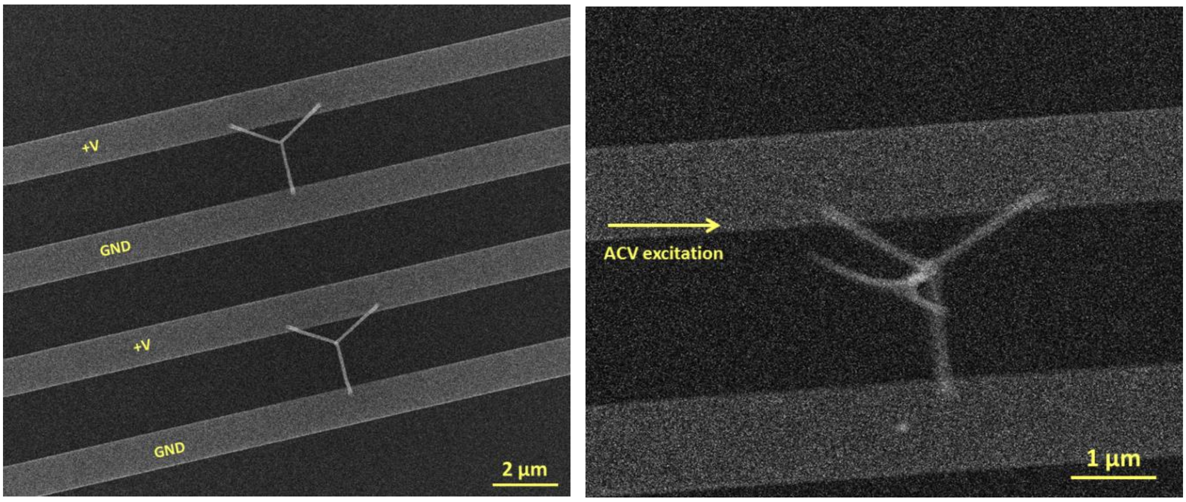

Figure 7-15: Tripods in top view deposited on two conductive lines each (left). The conducing strips can be connected outside the vacuum chamber. On the right hand side the image reveals an oscillating resonator (top view) on a tripod structure at a mechanical response onto an AC field of 493 kHz. The noisy signal of the image originates from the AC field.

7.3.2.2 Lambda Structures

Previous experiments prompt the conclusion that the oscillation of a pillar deposited ON a live structure does not sufficiently affect the current. As a result, the aim was to create a design, which enables oscillation of the current carrying structure itself and this was found for a shape further referred to as "lambda". It consists of a pillar connected to a side branch, typically deposited with a point pitch of 1 nm and a dwell time of 25 ms or 35 ms depending on the intended slope. A scheme is given in Figure 7-16: The lambda structure is made of a quasi-1D resonator which is connected to an electric circuit by a side branch. This geometry exhibits three important features:

1) *Oscillation (Resonance concept)*
2) *Gas adsorption leading to a changed resonance frequency (gas sensing concept)*
3) *Low-conductive region sensitive to oscillations (electrical read-out concept)*

The first one is mainly provided by the quasi-1D resonator which can be brought into resonance by an appropriate AC field (cf. chapter 6). Although the side-branch lowers the resonance frequency significantly, it can still be found in the kHz range. Gas adsorption of several molecules shifts the resonance frequency, which allows the detection of the present gaseous molecules with high sensitivity (chapter 7.2).

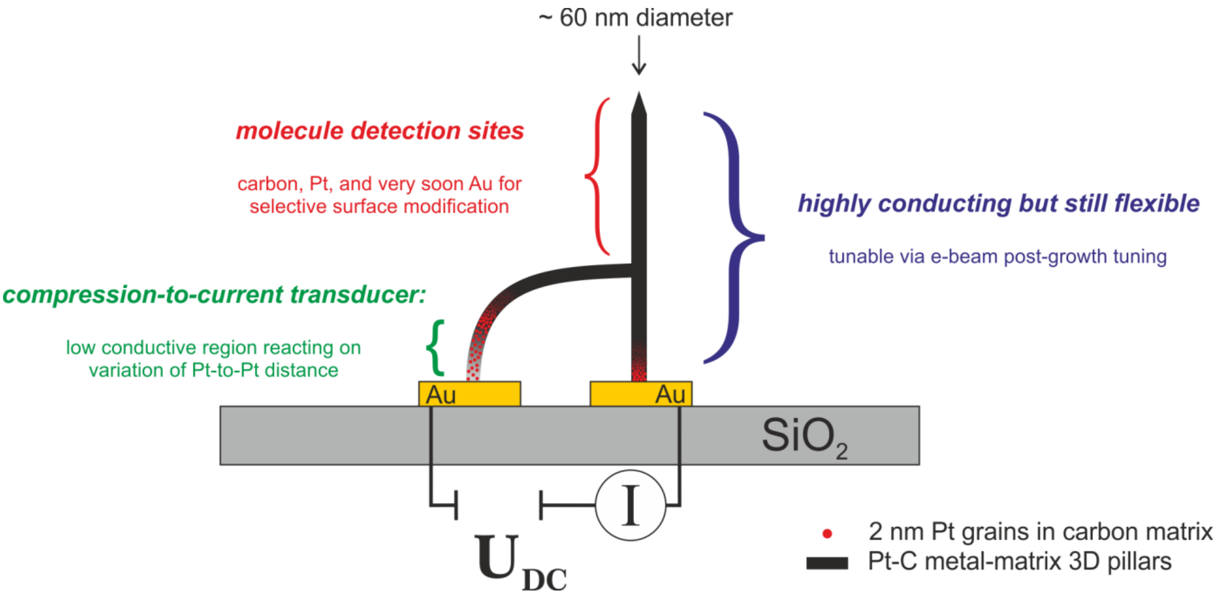

Figure 7-16: Schematic working principle of a lambda structure consisting of a quasi-1D resonator and an additional side branch. The pillar can be brought into resonance and thus provides the mechanical oscillation (blue). The electrical conductivity is increased via PGT skipping one part at the very beginning of the branch (green). Thereby, this low conductive region is highly sensitive to changed Pt-Pt grain distance and determines the current thorugh the entire circuit. Molecular adsorption (red) shifts the resonance frequency and allows the gas sensing detection via electrical read-out.

A drawback of the gas sensing strategy used in chapter 7.2 was the SEM based method of detection. Lambda structures represent a promising approach to cope with this task with a thoughtful strategy. The entire structure gets cured except for a small section at the base of the branch, which exhibits the highest curvature (marked in green in Figure 7-16). Consequently, this low conductive region determines the electrical conductivity of the entire circuit. In turn, the current reacts highly sensitively to changes of the conductivity within this active region. As Pt grains of as-deposited structures are separated by non-conductive carbon, the charge transport is associated with hopping transport (cf. chapter 7.3.2.1). As a result, the conductivity within this region is affected by a changed distance between Pt grains, which can be induced by mechanical oscillation. Hence, this geometry connects the main finding of this work: Gas adsorption changes the frequency of the resonant response to AC fields, which can be identified via an altered current due to changed Pt-Pt distances.

Initially, the lambda structure was supposed to oscillate in the direction of the side branch to change the curvature in the functional region (Figure 7-17 left). In practice, it was not possible to induce an oscillation in the intended direction although the position of the excitation electrode was varied. The fixing of the pillar induced by the side-branch turned out to be too strong to enable a deflection of the pillar along the side-branch. Therefore, the excitation direction was changed by 90° which led to enormous amplitudes including oscillation of the side branch as shown in Figure 7-17 (right).

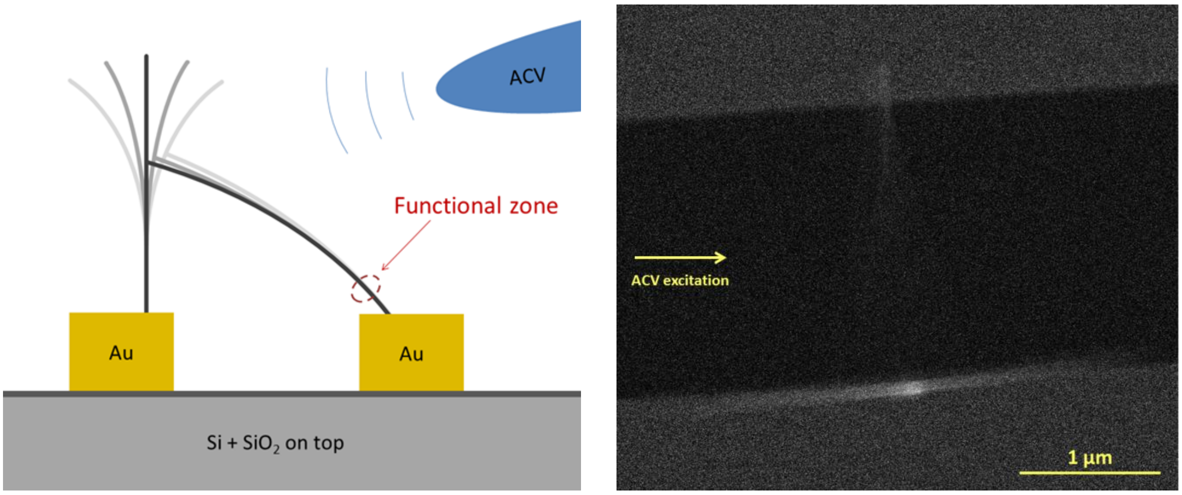

Figure 7-17: Intended concept for the high compression of the nano-granular structure (left). Rotated oscillation direction by 90° which led to lateral oscillation of both, free-standing resonator and side-branch as shown in Figure 7-16.

Current measurements revealed a behavior similar to tripod structures. The current rises exponentially with respect to the applied DC voltage (Figure 7-18, left) and a reset measurement leads to a slightly reduced current (right, see bottom note).

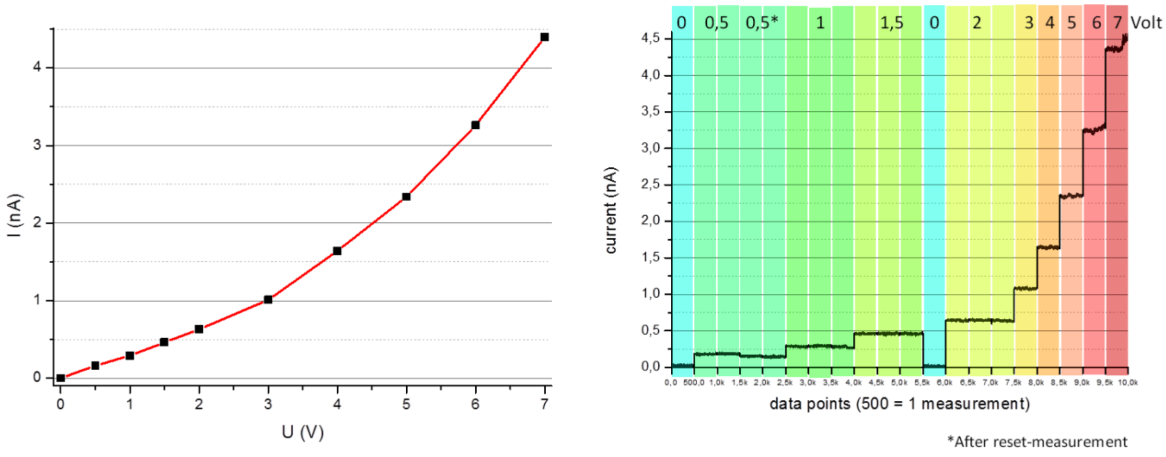

Figure 7-18: Current measurements of a lambda structure (branch length: 2.2 µm, dwell time: 30 ms, POP: 1 nm). Again a reset measurement slightly reduces the current as can be seen in the third and fourth measurement at 0.5 V (left). The right plot reveals mean values with respect to the applied voltage.

The final obstacle to overcome turned out to be the most sophisticated one: Measuring the DC current during an AC frequency sweep stimulates the resonant response of the lambda structure. As the measuring equipment was not state-of-the-art, current measurements demanded exceptionally careful handling. However, among a high number of partially cured lambda structures, very few, ideally partial-cured resonators revealed a current response as shown in Figure 7-19. As can be seen, a lowered current at the presence of mechanical oscillation can be seen to be in very good positional and shape agreement with the frequency peak. Please note that, although in good accordance, the current revealed a different response than expected: oscillation of the structure reduces the current. As is often the case in such development stages, nanotechnology works slightly differently than expected. This reflects a more complex situation as simple models suggest. Therefore, further investigations are planned which include strongly improved electric measurement equipment as well as dynamic low temperature transport measurements to access new phenomena of oscillating metal-matrix systems.

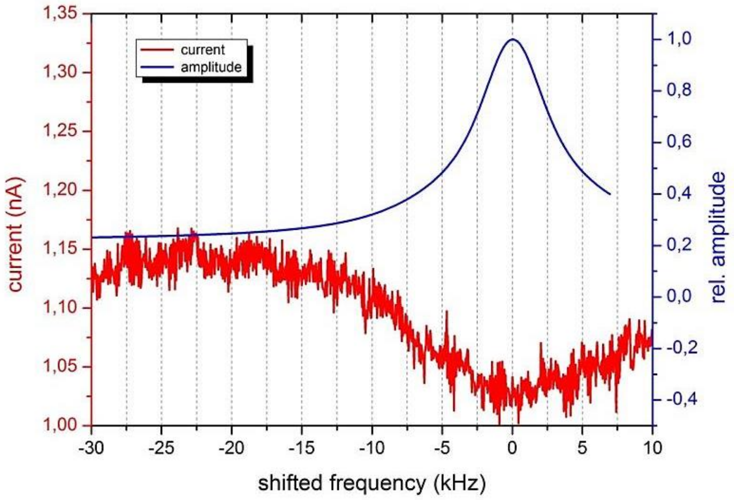

Figure 7-19: Oscillation of a resonating structure (blue) and current through the nano-granular deposit (red) following the concept in Figure 7-16. The current response (red) corresponds well to the mechanical oscillation (blue).

8 Summary and Outlook

Key result of this thesis is the proof of a unique gas sensing concept using electrically stimulated quasi-1D nano-resonators. These free-standing 3D nano-structures are fabricated by focused electron beam induced deposition (FEBID) using a $MeCpPt^{IV}Me_3$ precursor resulting in nano-granular two-phase composites consisting of a carbon matrix and Pt nano-particles. The uniqueness of this internal structure is the basis of our concept providing both sufficient conductivity and elasticity for electrically induced resonance oscillations. Adsorption experiments using SEM revealed a frequency shift related to the rate of adsorption and reacts extremely sensitively to interaction with adsorbates.

The study started with a comprehensive investigation concerning properties of such quasi-1D resonators with respect to deposition parameters. First of all, growth rates were observed and connected to corresponding fundamental regime mechanisms. Resonance oscillations were discussed in detail from both a qualitative and quantitative point of view. Chemical analysis provided a compositional insight into the nano-granular structure which was found to be in good compliance with investigated elastic properties. In more detail, deflection experiments were used to calculate Young’s modulus via finite element simulations. Consequently, as-deposited quasi-1D nano-resonators were found to behave similar to highly disordered polymer like carbon in terms of material properties although containing considerable amounts of Pt. The outcomes of these chemical and mechanical characterizations could be connected to deposition parameters providing a consistent theory for influences of PE energies and beam currents on mechanical properties and thus the resonance behavior of quasi-1D nano-resonators. Afterwards, close examination concerning impacts of post deposition e-beam radiation revealed the formation of graphite planes and a glassy carbon state. However, the elastic properties gathered for cured nano-resonators exceed those values which can be achieved for similar carbon structures in pristine bulks. The missing link was found in the Pt nano-particles. Ostwald ripening induced by the migration of atomic Pt released from carbon in precursor fragments by post growth treatments. As a consequence of these detailed investigations Euler-Bernoulli’s beam theory could be adapted in order to account for the unique two phase structure of FEBID fabricated nano-resonators.

This knowledge enabled the fabrication of nano-resonators which are suitable for high-sensitivity gas-sensing applications. Different gases were experimentally investigated and correlated with theory. This led to the classification of two effects contributing to the varying resonance frequencies: ***1)*** diameter increase due to adsorption layers, and ***2)*** diffusion into the material. In addition, the reversibility of these processes allowed drawing conclusions for the classification in physisorption and chemisorption.

Finally, the detection method as well as the geometry of the resonating structure was further developed. Lambda structure enabled the identification of the state of resonance via electrical current measurements in the nA range.

All in all, it is evident that this concept enables the detection of gaseous molecules with an incredible sensitivity. However, this extreme sensitivity also includes the drawback that such nano-resonators react to a multiplicity of interactions and processes. As a result, it is inevitable to functionalize the surface in order to promote the interaction with specific molecules in the ambient atmosphere. An ongoing approach developed at FELMI is the alteration of the metal using Au instead of Pt. It is well known that Au reveals a strong affinity to toxic volatile organic carbons. Further functionalizing Au with thiols enables a further advanced specific detection of gases in the surrounding air. Hence, future application can be seen in the qualitative detection of smallest traces of toxic components.

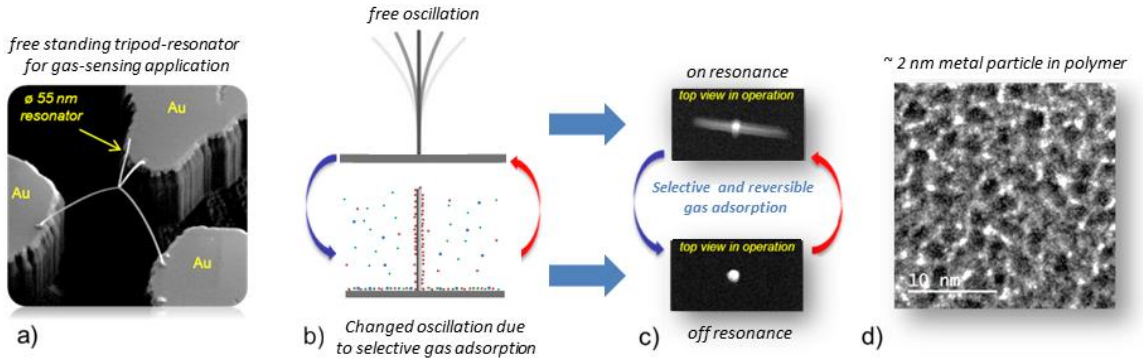

Figure 8-1: Possible free-standing architecture for gas sensing applications (a), its working principle (b) and correspondingly visualized via SEM images (c). The unique nano-structure (d) enables elastic oscillation and simultaneous electrical conductivity.

9 Bibliography

1. Utke I. *Nanofabrication Using Focused Ion and Electron Beams: Principles and Applications*. 1st ed. Oxford: Oxford Univ. Press; 2012.

2. Van Dorp WF, Hagen CW. A critical literature review of focused electron beam induced deposition. *J. Appl. Phys.* 2008;104(8):081301. doi:10.1063/1.2977587.

3. Utke I, Hoffmann P, Melngailis J. Gas-assisted focused electron beam and ion beam processing and fabrication. *J. Vac. Sci. Technol. B Microelectron. Nanom. Struct.* 2008;26(2008):1197. doi:10.1116/1.2955728.

4. Botman a, Mulders JJL, Hagen CW. Creating pure nanostructures from electron-beam-induced deposition using purification techniques: a technology perspective. *Nanotechnology* 2009;20:372001. doi:10.1088/0957-4484/20/37/372001.

5. Huth M, Porrati F, Schwalb C, et al. Focused electron beam induced deposition: A perspective. *Beilstein J. Nanotechnol.* 2012;3:597-619. doi:10.3762/bjnano.3.70.

6. Wnuk JD, Gorham JM, Rosenberg SG, et al. Electron induced surface reactions of the organometallic precursor trimethyl(methylcyclopentadienyl)platinum(IV). *J. Phys. Chem. C* 2009;113(Iv):2487-2496. doi:10.1021/jp807824c.

7. Winkler R, Fowlkes J, Szkudlarek A, Utke I, Rack PD, Plank H. The Nanoscale Implications of a Molecular Gas Beam during Electron Beam Induced Deposition. *ACS Appl. Mater. Interfaces* 2014;6:2987-95. doi:10.1021/am405591d.

8. Plank H. *Courtesy*.; 2015.

9. Goldstein JI. *Scanning Electron Microscopy and X-Ray Microanalysis*. 3rd ed. New York, NY: Kluwer Academic, Plenum Publ; 2003.

10. Reimer L. *Scanning Electron Microscopy: Physics of Image Formation and Microanalysis*. 2nd ed. Springer Berlin Heidelberg; 1998. doi:10.1007/978-3-540-38967-5.

11. Engmann S, Stano M, Papp P, Brunger MJ, Matejčík Š, Ingólfsson O. Absolute cross sections for dissociative electron attachment and dissociative ionization of cobalt tricarbonyl nitrosyl in the energy range from 0 eV to 140 eV. *J. Chem. Phys.* 2013;138:0-7. doi:10.1063/1.4776756.

12. Utke I, Friedli V, Purrucker M, Michler J. Resolution in Focused Electron- and Ion-Beam Induced Chemical Vapor Deposition. 2007;2219(2007):4. doi:10.1116/1.2789441.

13. Szkudlarek A, Gabureac M, Utke I. Determination of the surface diffusion coefficient and the residence time of adsorbates via local focused electron beam induced chemical vapour deposition. *J. Nanosci. Nanotechnol.* 2011;11:8074-8078. doi:10.1166/jnn.2011.5066.

14. Plank H, Haber T, Gspan C, Kothleitner G, Hofer F. Chemical tuning of PtC nanostructures fabricated via focused electron beam induced deposition. *Nanotechnology* 2013;24(17):175305. doi:10.1088/0957-4484/24/17/175305.

15. Allen TE. Monte Carlo calculation of low-energy electron emission from surfaces. *J. Vac. Sci. Technol. B Microelectron. Nanom. Struct.* 1988;6(1988):2057. doi:10.1116/1.584111.

16. Drouin D, Couture a. R, Joly D, Tastet X, Aimez V, Gauvin R. CASINO V2.42 - A fast and easy-to-use modeling tool for scanning electron microscopy and microanalysis users. *Scanning* 2007;29:92-101. doi:10.1002/sca.20000.

17. Jonge N De, Drouin D. Three-Dimensional Electron Microscopy Simulation with the CASINO Monte Carlo Software. 2012;33(3):135-146. doi:10.1002/sca.20262.Three-Dimensional.

18. Coutan AR, Drouan D, Gauvin R. monte CArlo SImulation of electroN trajectory in sOlids (CASINO). 2011. Available at: http://www.gel.usherbrooke.ca/casino/download2.html.

19. Schmied R, Fowlkes JD, Winkler R, Rack PD, Plank H. Fundamental edge broadening effects during focused electron beam induced nanosynthesis. *Beilstein J. Nanotechnol.* 2015;6:462-471. doi:10.3762/bjnano.6.47.

20. Fowlkes JD, Rack PD. Fundamental Electron-Precursor-Solid Deposition Simulations and Experiments. *ACS Nano* 2010;4(3):1619-1629. Available at: http://www.ncbi.nlm.nih.gov/pubmed/20201541.

21. Smith D a., Fowlkes JD, Rack PD. Understanding the kinetics and nanoscale morphology of electron-beam- induced deposition via a three-dimensional monte carlo simulation: the effects of the precursor molecule and the deposited material. *Small* 2008;4(9):1382-1389. doi:10.1002/smll.200701133.

22. Stermitz M. Free Standing Quasi-1D Resonators for Sensing Applications. 2014;(March).

23. Utke I. *Private Communication*.; 2013.

24. Winkler R. *Courtesy*.

25. Satoh H, Kawata S, Nakane H, Adachi H. Studies on the ZrO/W(100) surface by means of low-energy electron diffraction and X-ray photoelectron spectroscopy. *Surf. Sci.* 1998;400:375-382. doi:10.1016/S0039-6028(97)00896-0.

26. EdC. Fig 3-3 Everhart-Thornley_detector. 2007. Available at: http://fr.wikipedia.org/wiki/Détecteur_Everhart-Thornley. Accessed March 6, 2015.

27. Akhmadaliev C, Bischoff L, Mair GLR, Aidinis CJ, Ganetsos T. Investigation of emission instabilities of liquid metal ion sources. *Microelectron. Eng.* 2004;73-74:120-125. doi:10.1016/j.mee.2004.02.027.

28. Giannuzzi LA, Stevie FA. *Introduction to Focused Ion Beams: Instrumentation, Theory, Techniques and Practice*. New York, NY; 2005. doi:10.1007/b101190.

29. Trimethyl-methylcyclopentadienyl-platinum chemical composition. Available at: http://www.sigmaaldrich.com/catalog/product/aldrich/645605?lang=de&region=AT. Accessed March 6, 2015.

30. Michelitsch SG. Electrical in-situ measurements for e-beam induced Pt deposition. 2010.

31. Van Dorp WF, Wnuk JD, Gorham JM, Fairbrother DH, Madey TE, Hagen CW. Electron induced dissociation of trimethyl (methylcyclopentadienyl) platinum (IV): Total cross section as a function of incident electron energy. *J. Appl. Phys.* 2009;106(Iv). doi:10.1063/1.3225091.

32. Kolb F, Schmoltner K, Huth M, et al. Variable tunneling barriers in FEBID based PtC metal-matrix nanocomposites as a transducing element for humidity sensing. *Nanotechnology* 2013;24:305501. doi:10.1088/0957-4484/24/30/305501.

33. Porrati F, Sachser R, Schwalb CH, Frangakis a. S, Huth M. Tuning the electrical conductivity of Pt-containing granular metals by postgrowth electron irradiation. *J. Appl. Phys.* 2011;109(6):063715. doi:10.1063/1.3559773.

34. Plank H, Kothleitner G, Hofer F, et al. Optimization of postgrowth electron-beam curing for focused electron-beam-induced Pt deposits. *J. Vac. Sci. Technol. B Microelectron. Nanom. Struct.* 2011;29(5):051801. doi:10.1116/1.3622314.

35. Winkler R. Implications of Precursor Dynamics on Nanostructures during Focused Electron Beam Induced Deposition. 2013;(December).

36. Oxford Instruments Nanomanipulator OmniProbe 200. Available at: http://www.oxford-instruments.com/products/nanomanipulation-nanofabrication/nanomanipulator/omniprobe-200. Accessed April 4, 2015.

37. Pico Technology. 2015. Available at: https://www.picotech.com/oscilloscope/3000/usb3-oscilloscope-logic-analyzer. Accessed April 4, 2015.

38. BRUKER. ESPRIT. Available at: https://www.bruker.com/de/products/x-ray-diffraction-and-elemental-analysis/eds-wds-ebsd-sem-micro-xrf-and-sem-micro-ct/esprit-2.html.

39. Kleindiek Nanotechnik Micromanipulator. Available at: http://www.nanotechnik.com/mm3a-em.html. Accessed April 4, 2015.

40. Brown D. Tracker 4.84. 2014. Available at: https://www.cabrillo.edu/~dbrown/tracker/.

41. Gross D, Hauger W, Schnell W, Wriggers P. Schwingungen kontinuierlicher Systeme. In: *Technische Mechanik 4*. Springer Berlin Heidelberg; 2007:232-254. doi:10.1007/978-3-540-70738-7.

42. Davis J, Taylor JD. ANALYSIS OF THE NONLINEAR VIBRATIONS OF ELECTROSTATICALLY ACTUATED MICRO-CANTILEVERS IN HARMONIC DETECTION OF RESONANCE (HDR). 2008;(August).

43. Li XF. A unified approach for analyzing static and dynamic behaviors of functionally graded Timoshenko and Euler-Bernoulli beams. *J. Sound Vib.* 2008;318:1210-1229. doi:10.1016/j.jsv.2008.04.056.

44. Gross D, Ehlers W, Wriggers P. *Formeln Und Aufgaben Zur Technischen Mechanik 2 - Elastostatik, Hydrostatik*. 4th ed. Heidelberg: Springer Berlin Heidelberg; 2007. doi:978-3-540-70768-4.

45. Fowlkes JD, Geier B, Rack PD, M. S, Winkler R, Plank H. Electron nanoprobe induced oxidation: a simulation of direct-write purification. 2012. doi:10.1039/xoxxooooox.

46. Robertson J. Properties of diamond-like carbon. *Surf. Coatings Technol.* 1992;50:185-203. doi:10.1016/0257-8972(92)90001-Q.

47. McEnaney B. Structure and bonding in carbon materials. In: Burchell TD, ed. *Carbon Materials for Advanced Technologies*.Vol 3. 1st ed. Amsterdam: Pergamon [Press], Elsevier, Elsevier Science, Pergamon; 1999:11. Available at: http://onlinelibrary.wiley.com/doi/10.1002/chin.199951294/full.

48. Salvadori M, Brown I, Vaz a., Melo L, Cattani M. Measurement of the elastic modulus of nanostructured gold and platinum thin films. *Phys. Rev. B* 2003;67:2-5. doi:10.1103/PhysRevB.67.153404.

49. Frabboni S, Gazzadi GC, Spessot a. TEM study of annealed Pt nanostructures grown by electron beam-induced deposition. *Phys. E Low-Dimensional Syst. Nanostructures* 2007;37:265-269. doi:10.1016/j.physe.2006.06.018.

50. Dwivedi N, Kumar S, Malik HK, Govind, Rauthan CMS, Panwar OS. Correlation of sp3 and sp2 fraction of carbon with electrical, optical and nano-mechanical properties of argon-diluted diamond-like carbon films. *Appl. Surf. Sci.* 2011;257(15):6804-6810. doi:10.1016/j.apsusc.2011.02.134.

51. Kelires PC. Elastic properties of amorphous carbon networks. *Phys. Rev. Lett.* 1994;73(18):2460-2463. doi:10.1103/PhysRevLett.73.2460.

52. Salvetat BJ, Kulik AJ, Bonard J, et al. Elastic Modulus of Ordered and Disordered Multiwalled Carbon Nanotubes **. 1999;(2):161-165.

53. Li B, Zhang P, Fu QQ, Li XF, Zhao X, Song XL. Nonlinear elastic behavior and failure mechanism of polyhedral graphite particles undergoing uniaxial compression. *J. Appl. Phys.* 2014;116:053504. doi:10.1063/1.4891729.

54. Kiselev VM, Belousova IM, Belousov VP, Sosnov EN. Gas Adsorption by Fullerenes and Polyhedral Multi-Walled Carbon Nanostructures. In: Rossi M, ed. *Carbon Nanomaterials for Gas Adsorption*. Pan Stanford Publishing 2012; 2012.

55. Nechaev YS. Physical and Chemical Interactions of Hydrogen with Carbonaceous Nanostructures (An Analytical Study — Indirect Experiment). In: Rossi M, ed. *Carbon Nanomaterials for Gas Adsorption*. Pan Stanford Publishing 2012; 2012.

56. Geier B, Gspan C, Winkler R, et al. Rapid and Highly Compact Puri fi cation for Focused Electron Beam Induced Deposits: A Low Temperature Approach Using Electron Stimulated H 2 O Reactions. 2014.

57. Barnard AS. Modeling Gas Adsorption on Carbon Nanotubes. In: Rossi M, ed. *Carbon Nanomaterials for Gas Adsorption*. Pan Stanford Publishing 2012; 2012.

58. Zollo G, Gala F. Atomistic Simulation of Gas Adsorption in Carbon Nanostructures. In: Rossi M, ed. *Carbon Nanomaterials for Gas Adsorption*. Pan Stanford Publishing 2012; 2012.

59. Inagaki M, Kang F. Engineering and Applications of Carbon Materials. In: *Materials Science and Engineering of Carbon: Fundamentals*. 2nd ed. Amsterdam: Butterworth-Heinemann; 2014:298.

60. Braun M, Fabrikant II, Ruf M-W, Hotop H. High-resolution studies of (SF 6) q − (q = 1–3) cluster anion formation in low-energy electron collisions with (SF . *J. Phys. B At. Mol. Opt. Phys.* 2013;46:195202. doi:10.1088/0953-4075/46/19/195202.